A non–resonant inelastic x–ray scattering study on silicon oxides and clathrates

Dissertation

zur Erlangung des Doktorgrades der Naturwissenschaften
der Fakultät Physik der Technischen Universität Dortmund

vorgelegt von
Henning Sternemann

Februar 2008

Abstract

Thesis advisor
Metin Tolan

Author
Henning Sternemann

A non–resonant inelastic x–ray scattering study on silicon oxides and clathrates

Silicon is still a dominating element in terms of industrial applications and also fundamental research. Silicon oxides play a key role for insulator layers in integrated circuits and coatings for opto–electric devices. A microscopic understanding of the silicon–oxide structure is therefore highly demanded. New nanostructured silicon compounds showing particular physical behavior have been discovered during the last decade. So, endohedrally doped silicon clathrates are promising materials for thermo–electric applications and tailored band–gaps. The study of the interaction between the guest atoms and the host silicon network is crucial to understand changes in physical properties. Also in the view of fundamental research silicon clathrates show exciting structural and electronic phase–transitions under high pressure.

Access to the structural and electronic information in bulk amorphous silicon monoxide and complex silicon compounds can be achieved by the study of absorption edges. Non–resonant inelastic x–ray scattering is a powerful tool to measure shallow absorption edges using hard x–rays. This allows the study of low energy transitions under conditions which do not permit electrons and soft x–rays. In the present work, an algorithm is presented for the proper experimental extraction of momentum–transfer dependent scattering spectra. A comparison with ab–initio calculations can contribute significantly to the understanding of the experimental spectra. Therefore, the applicability and the limits of theoretical approaches are elaborated in a study of the pure elements silicon, magnesium and sodium. Based on these methodical advances, the disproportionation of bulk amorphous silicon monoxide is analyzed and compared to the interface clusters mixture model for the SiO structure. Complex nano–structured barium doped silicon networks are examined by the survey of the barium giant dipole resonance. The first observation of different modulations of the resonance depending on the structure will be presented and future applications on high–pressure research will be highlighted.

Contents

List of Figures

List of Tables

List of Acronyms

ANR	Ankudinov, Nesvizhskii and Rehr exchange kernel
APS	Advanced Photon Source
BSE	Bethe–Salpeter equation
CA	Core Compton profile asymmetry
DAC	Diamond–anvil cell
DDSCS	Double differential scattering cross section
DELTA	Dortmunder Elektronenspeicherring–Anlage
DFT	Density–functional theory
DOS	Density of states
l–DOS	Projected DOS respecting the angular momentum of the final state
ESRF	European Synchrotron Radiation Facility
EXAFS	Extended x–ray absorption fine structure
FMS	Full multiple scattering
HF	Hartree–Fock
IA	Impulse approximation
ICM	Interface clusters mixture (model)
IXS	Inelastic x–ray scattering
LCAO	Linear combination of atomic orbitals
LDA	Local–density approximation
LFC	Local–field correction
LERIX	Lower energy resolution inelastic x–ray scattering spectrometer
MOSFET	Metal oxide semiconductor field effect transistor
NMR	Nuclear magnetic resonance
NRIXS	Non–resonant inelastic x–ray scattering
RB	Random–bonding (model)
RIXS	Resonant inelastic x–ray scattering
RM	Random–mixture (model)
RPA	Random–phase approximation
RSMS	Real space multiple scattering
SK	Slater–Koster
SPring–8	8 GeV Super Photon Ring
StoBe–deMon	Stockholm–Berlin version of the deMon DFT code
TDLDA	Time dependent local density approximation
VA	Valence Compton profile asymmetry
VP	Valence Compton profile
XAFS	X–ray absorption fine structure

XANES	X–ray absorption near–edge structure
XAS	X–ray absorption spectroscopy
XRD	X–ray diffraction
XRS	X–ray Raman scattering (see NRIXS)

Chapter 1

Introduction

From the first integrated circuit and the rise of microelectronics to the growth of nanostructured materials, silicon has always played a key role in material and semiconductor science. Silicon nanocrystals embedded in an oxide matrix are a class of material moving into the focus of applied research. Such systems have revealed to be promising candidates for high efficient photoluminescent structures and non–volatile flash memory applications.[1] Bulk amorphous silicon monoxide or SiO_x/SiO_2 multilayer systems are favorable starting materials for their production.[2] Especially the cluster growth and the structure of suboxide interfaces between clusters and oxide are of importance. With the ongoing miniaturization of electronic devices, buried amorphous silicon and silicon/germanium suboxide interfaces between conducting and insulating layers are also becoming crucial for the functionality and the performance of microelectronics.[3] The development of a nanostructure model for amorphous silicon monoxides and the process of its disproportionation with the growth of nanocrystals is therefore topic of current research.

In recent years, also novel compounds based on complex silicon networks, especially silicon clathrates, exhibited attractive physical and electronic features from superconductivity to magnetic order.[4] Moreover, their electronic structure can be altered by intercalation of different guest atoms leading to, e.g., orbital hybridization and charge transfer.[5] Therefore, the knowledge of the coupling between a guest atom and its host lattice allows a tailoring of the electronic and physical properties in a wide range, e.g., concerning band–electronic or thermo–electric structure.[6]

---

[1] T.Z. Lu *et al.* (2006), *J. Appl. Phys.* **100**, 014310; A. Zimina *et al.* (2006), *Appl. Phys. Lett.* **88**, 163103.

[2] V. Kapaklis *et al.* (2005), *Appl. Phys. Lett.* **87**, 123114; M. Mamiya *et al.* (2001), *J. Cryst. Growth* **229**, 457; M. Zacharias *et al.* (2002), *Appl. Phys. Lett.* **80**, 661.

[3] S. Balakumar *et al.* (2007), *Appl. Phys. Lett.* **90**, 032111; D.R. Hamann (2000), *Phys. Rev. B* **61**, 9899.

[4] C.L. Condron *et al.* (2005), *Inorg. Chem.* **44**, 9185; H. Kawaji *et al.* (1995), *Phys. Rev. Lett.* **74**, 1427; Y. Mudryk *et al.* (2002), *J. Phys.: Condens. Matter* **14**, 7991.

[5] J.P. Connerade and M.W.D. Mansfield (1982), *Phys. Rev. Lett.* **48**, 131; D. Connétable (2007), *Phys. Rev. B* **75**, 125202.

[6] G.B. Adams *et al.* (1994), *Phys. Rev. B* **49**, 8048; D. Kahn and J.P. Lu (1997), *Phys. Rev. B* **56**, 13898; G.S. Nolas *et al.* (2001), *Semicond. Semimet.* **69**, 255.

The growing variety of novel compounds for electronic applications exhibits the need for studies of internal interfaces and bulk properties. A favorable method sensitive to local and electronic structure in bulk samples is non–resonant inelastic x–ray scattering (NRIXS).

Study of core electrons by NRIXS — often also referred to as x–ray Raman scattering (XRS) — is a unique tool to access shallow absorption edges with high–energy x–rays.[7] Hence, it is an important technique with a growing rate of applications to study bulk properties,[8] liquids[9] or systems in extreme environments[10] where soft x–rays or electrons are disadvantageous as probe. Since NRIXS is a scattering process, a finite momentum transfer q according to the scattering angle ϕ is employed.[11] Thus, the selection rules for excitation channels can be freely chosen and final states of different orbital momenta can be studied.[12] Soininen *et al.*[13] showed that the projected unoccupied density of states is accessible with q–dependent NRIXS. The decomposition of the spectra would allow a direct comparison between theory and experiment for the angular momentum dependent transition channels. Recently, the background proportional enhancement of the extended fine structure in NRIXS was demonstrated for magnesium, aluminum,[14] and ice[15] by variation of the momentum transfer. Moreover, both the orientation of the momentum–transfer vector considering the symmetry axes of a crystalline sample and the dependence on its absolute value were essential to study directionally dependent excitations, e.g. for the hexagonal MgB_2 and Be.[16] Therefore, employing the q–dependence of NRIXS is of significant importance in such studies. The applications of NRIXS spectroscopy strongly increased with the advent of synchrotron radiation and during the recent years, various experimental setups have become accessible at third generation synchrotron sources. Inter alia, these are spec-

---

[7] A comprehensive overview on the history of NRIXS and its recent developments is given by W. Schülke (2007), *Electron dynamics by inelastic x–ray scattering*, Oxford University Press.

[8] M. Balasubramanian *et al.* (2007), *Appl. Phys. Lett.* **91**, 031904; U. Bergmann *et al.* (2002), *Microchem. J.* **71**, 221; A. Mattila *et al.* (2005), *Phys. Rev. Lett.* **94**, 247003; C. Sternemann *et al.* (2005*a*), *Phys. Rev. B* **72**, 035104; C. Sternemann *et al.* (2005*b*), *Phys. Rev. Lett.* **95**, 157401; H. Sternemann *et al.* (2007*a*), *Phys. Rev. B* **75**, 075118; H. Sternemann *et al.* (2007*b*), *Phys. Rev. B* **75**, 245102.

[9] U. Bergmann *et al.* (2007*a*), *Phys. Rev. B* **76**, 024202; Y.Q. Cai *et al.* (2005), *Phys. Rev. Lett.* **94**, 025502; Ph. Wernet *et al.* (2004), *Science* **304**, 995.

[10] D.A. Arms *et al.* (2005), *Phys. Rev. B* **71**, 233107; R.S. Kumar *et al.* (2007), *Diamond Rel. Mat.* **16**, 1136; S.K. Lee *et al.* (2005), *Nature Materials* **4**, 851; S.K. Lee *et al.* (2007), *Phys. Rev. Lett.* **98**, 105502; W.L. Mao *et al.* (2003), *Science* **302**, 425; W.L. Mao *et al.* (2006), *Science* **314**, 636; Y. Meng *et al.* (2004), *Nat. Mater.* **3**, 111; Ph. Wernet *et al.* (2005), *J. Chem. Phys.* **123**, 154503.

[11] M.H. Krisch *et al.* (1997), *Phys. Rev. Lett.* **78**, 2843; H. Nagasawa *et al.* (1997), *J. Phys. Soc. Jpn.* **66**, 3139; J.A. Soininen *et al.* (2001), *J. Phys.: Condens. Matter* **13**, 8039; C. Sternemann *et al.* (2003), *Phys. Rev. B* **68**, 035111.

[12] Y. Feng *et al.* (2004), *Phys. Rev. B* **69**, 125402; K. Hämäläinen *et al.* (2002), *Phys. Rev. B* **65**, 155111; C. Sternemann *et al.* (2003), *Phys. Rev. B* **68**, 035111.

[13] J.A. Soininen *et al.* (2006), *J. Phys.: Cond. Mat.* **18**, 7327.

[14] T.T. Fister *et al.* (2006*a*), *Phys. Rev. B* **74**, 214117.

[15] U. Bergmann *et al.* (2007*b*), *J. Chem. Phys.* **127**, 174504.

[16] A. Mattila *et al.* (2005), *Phys. Rev. Lett.* **94**, 247003; C. Sternemann *et al.* (2003), *Phys. Rev. B* **68**, 035111.

trometers at beamline ID16 of the European Synchrotron Radiation Facility (ESRF),[17] the Taiwan beamline BL12XU of the 8 GeV Super Photon Ring (SPring–8),[18] and the beamlines 13–IDD,[19] 16–IDD,[20] 18–IDD[21] and 20–ID[22] of the Advanced Photon Source (APS).

Despite the advance of experimental setups and the possibility of highly sophisticated experiments, the analysis of the momentum–transfer dependent NRIXS spectra is still a challenge. This is due to the lack of universal algorithms for the separation of the element–selective signal of a certain absorption edge from the undesirable Compton scattering of other electrons in the system. An experimentally self–consistent approach for such a universal algorithm has been developed and is presented in this work.

The interpretation of NRIXS spectra by computational methods has made great progress in recent years. For simple bulk crystalline elements, an approach based on the Bethe–Salpeter equation (BSE) leads to a remarkable agreement between experiment and theory.[23] However, the computational cost of this approach quickly becomes unfeasible for amorphous systems[24] or systems with large unit cells, e.g. clathrates or fullerenes. An adaptation of the real space multiple scattering (RSMS) approach FEFF8.2[25] for NRIXS spectra[26] can overcome this computational bottleneck. It has been shown that this approach yields very good results for the K–edge of bulk crystalline beryllium when compared to experiments. For the study of medium– and high–Z materials, it is important to extend calculations also to L–, M–, and higher edges. The experimental accessibility of such shallow absorption edges by NRIXS has already been shown.[27] For a thorough application of the RSMS method on complex samples, especially for the calculation of non–K edges, a critical study on the capabilities and limitations of this approach is eligible. In this work, a comparison of RSMS L–edge calculations with experiment and theory will be discussed with focus on the near–edge regime.

The bulk sensitivity of NRIXS is advantageous for the examination of internal interfacial domains. The advances in the experimental analysis of NRIXS spectra allow a momentum–transfer dependent study on the disproportionation of bulk amorphous silicon monoxide

---

[17] M.H. Krisch *et al.* (1997), *Phys. Rev. Lett.* **78**, 2843.

[18] Y.Q. Cai *et al.* (2004), *AIP Conf. Proc.* **705**, 340.

[19] W.L. Mao *et al.* (2003), *Science* **302**, 425; Y. Meng *et al.* (2004), *Nat. Mater.* **3**, 111.

[20] R.S. Kumar *et al.* (2007), *Diamond Rel. Mat.* **16**, 1136.

[21] U. Bergmann and S.P. Cramer (1998), *SPIE Proc.* **3448**, 198.

[22] T.T. Fister *et al.* (2006*b*), *Rev. Sci. Instr.* **77**, 063901.

[23] J.A. Soininen and E.L. Shirley (2001), *Phys. Rev. B* **64**, 165112; J.A. Soininen *et al.* (2001), *J. Phys.: Condens. Matter* **13**, 8039.

[24] C. Sternemann *et al.* (2005*c*), *J. Phys. Chem. Solids* **66**, 2277.

[25] A.L. Ankudinov *et al.* (1998*a*), *Phys. Rev. B* **58**, 7565.

[26] J.A. Soininen *et al.* (2005), *Phys. Rev. B* **72**, 045136.

[27] W.A. Caliebe (1997), "Inelastic X–Ray Scattering with High Energy Resolution", PhD thesis, Christian–Albrechts Universität zu Kiel; C. Sternemann *et al.* (2005*a*), *Phys. Rev. B* **72**, 035104.

and on the spectral contribution of the suboxide interface. The degree of disproportionation and its temperature dependence will be analyzed in this work and brought into comparison with results of amorphous germanium monoxide. The extracted dynamic structure factor of the suboxides will be presented and viewed together with first ab–initio calculations.

The intercalation of guest atoms into nanostructured silicon based compounds to intentionally change physical properties of the material requires an insight into the structural and electronic environment of the guests. The giant resonance is an access to the local surrounding of certain guest atoms. A study of the barium giant dipole resonance in complex silicon surroundings, such as clathrate structures, will be presented in this work. Modulations of the giant resonance will be extracted and compared to RSMS calculations. This work is organized as follows:

Chapter 2: The theoretical framework for non–resonant inelastic x–ray scattering is outlined with special focus on a numerical real space multiple scattering approach.

Chapter 3: Experimental requirements and details of the beamlines, at which the experiments have been accomplished, are discussed.

Chapter 4: A consistent background–removal algorithm is presented for momentum–transfer dependent inelastic x–ray studies. It is exemplified on the study of the silicon $L_{II,III}$–edges in Si and SiO_2.

Chapter 5: A real space multiple scattering approach is applied to the study of elemental solids' L–edges and its prospects as well as its limitations are discussed in detail.

Chapter 6: A study of the disproportionation process of bulk amorphous silicon monoxide depending on the annealing temperature will be presented. The results of the temperature behavior are compared with a recent study of bulk amorphous germanium monoxide. Furthermore, the spectral contribution of silicon suboxides is extracted from the total spectrum and compared with calculations from an ab–initio DFT approach.

Chapter 7: Bulk nanostructured barium doped silicon compounds are analyzed utilizing the barium giant dipole resonance. Theoretically predicted changes in the fine structure of the resonance for different compounds have been experimentally found and are compared to ab–initio calculations. A first high–pressure experiment for barium doped silicon clathrates is presented and the prospects of future high–pressure studies are emphasized. An experimentally observed complex momentum–transfer dependence is presented for an iodine–doped silicon clathrate.

Chapter 8: The results of this work are summarized and an outlook on possible consecutive studies based on this work will be given.

Chapter 2

Theory of non–resonant inelastic x–ray scattering

In this chapter the theoretical principles for non–resonant inelastic x–ray scattering shall briefly be outlined. Numerical approaches for the calculation of NRIXS spectra will be emphasized besides the discussion of the physical process in the light of Fermi's golden rule.[1]

Inelastic x–ray scattering (IXS) is a powerful and versatile tool for studying the electronic structure of matter.[2] Most generally, an inelastic x–ray scattering process can be displayed as shown in Fig. 2.1. A photon of energy[3] ω_1 and wave vector $\mathbf{k}_1$ is scattered by the sample into a photon of energy ω_2 and wave vector $\mathbf{k}_2$. As in elastic scattering experiments, the probed length scale is determined by the momentum transfer $\mathbf{q} = \mathbf{k}_1 - \mathbf{k}_2$, which is dependent on the scattering angle ϕ. Excitations are probed via an energy transfer $\omega = \omega_1 - \omega_2$.

The inelastic scattering process is represented by the Hamilton operator H_{int} describing the interaction between the electromagnetic field and the electrons in the scattering system. Within Born–Oppenheimer approximation and for the non–relativistic case it can be written as a sum over the electrons involved:[4]

$$H_{\text{int}} = \sum_n \frac{e^2}{2m}\mathbf{A}_n^2 + \sum_n \frac{e}{m}\mathbf{p}_n \cdot \mathbf{A}_n, \tag{2.1}$$

where $\mathbf{p}_n$ is the momentum of the nth electron, $\mathbf{A}_n$ is the vector potential of the electro-

---

[1] Special theoretical details important for the extraction of experimental spectra are discussed separately in chapter 4.

[2] For a comprehensive overview see: W. Schülke (1991), "Inelastic scattering by electronic excitations", *Handbook on synchrotron radiation, Vol. 3*, ed. by G.S. Brown and D.E. Moncton, North–Holland, Amsterdam; W. Schülke (2007), *Electron dynamics by inelastic x–ray scattering*, Oxford University Press.

[3] Natural units with $\hbar = c = 1$ are used for the derivation of the dynamical structure factor (c is the speed of light). However, for convenience, energies will be given in eV ($1\,\text{eV} \approx 1.602 \times 10^{-19}\,\text{J}$) and momenta in atomic units ($1\,\text{a.u.} \approx 1.89\ \text{Å}^{-1}$).

[4] K. Hämäläinen and S. Manninen (2001), *J. Phys.: Condens. Matter* **13**, 7539.

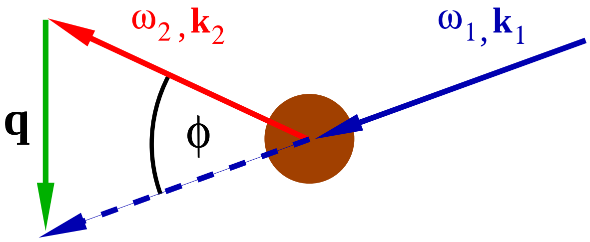

Figure 2.1: Inelastic x–ray scattering process. X–rays of energy ω_1 and wave vector $\mathbf{k}_1$ are scattered to an energy ω_2 and wave vector $\mathbf{k}_2$ so that an energy ω and a momentum $\mathbf{q}$ is transferred to the scattering system.

magnetic field, e is the electron charge, and m its mass. In first order perturbation theory, the left term gives rise to elastic and non–resonant inelastic scattering whereas the second describes absorption and emission. Inelastic x–ray scattering is a two–photon process. Therefore resonant inelastic x–ray scattering[5] originating from the $\mathbf{p} \cdot \mathbf{A}$ term contributes only in second order perturbation theory.

The double differential cross section $\frac{d^2\sigma}{d\Omega d\omega_2}$ is the quantity measured in an IXS experiment and can be expressed by means of the Kramers–Heisenberg formula[6] employing the interaction Hamiltonian (2.1). The non–resonant part is given in the Born approximation by

$$\left.\frac{d^2\sigma}{d\Omega d\omega_2}\right|_{\mathrm{NR}} = r_0^2 \frac{\omega_2}{\omega_1} (\boldsymbol{\epsilon}_1 \cdot \boldsymbol{\epsilon}_2)^2 \sum_{\mathrm{f}} \left| \langle \mathrm{f} | \sum_n e^{i\mathbf{q}\cdot\mathbf{r}_n} | \mathrm{i} \rangle \right|^2 \delta\left(E_{\mathrm{f}} - E_{\mathrm{i}} - \omega\right), \tag{2.2}$$

where $|\mathrm{i}\rangle$ is the initial state and $|\mathrm{f}\rangle$ are the final states, respectively, $\boldsymbol{\epsilon}_1, \boldsymbol{\epsilon}_2$ are the photon polarizations of the incoming and scattered x–rays, and $r_0 = e^4/m^2$ is the classical electron radius. It can be written as

$$\left.\frac{d^2\sigma}{d\Omega d\omega}\right|_{\mathrm{NR}} = \left(\frac{d\sigma}{d\Omega}\right)_{\mathrm{Th}} \frac{\omega_2}{\omega_1} S(\mathbf{q}, \omega). \tag{2.3}$$

In a single particle theory the dynamic structure factor $S(\mathbf{q}, \omega)$ is given by

$$S(\mathbf{q}, \omega) = \sum_f \left| \langle \mathrm{f} | e^{i\mathbf{q}\cdot\mathbf{r}} | \mathrm{i} \rangle \right|^2 \delta(\omega + E_{\mathrm{i}} - E_{\mathrm{f}}) \tag{2.4}$$

according to Fermi's golden rule. $\left(\frac{d\sigma}{d\Omega}\right)_{\mathrm{Th}}$ is Thomson's scattering cross section, i.e. the coupling between photon and electron. A full knowledge of the dynamic structure factor for arbitrary momentum transfer and energy loss would come along with a full understanding of all excitations on all length scales within the sample. However, experimentally, $S(\mathbf{q}, \omega)$

---

[5] I.e. ω_1 is close to an absorption edge.

[6] H.A. Kramers and W. Heisenberg (1925), *Z. Phys.* **31**, 681.

can only be measured for a finite number of $\mathbf{q}$ and range of ω. Following Schülke[7] NRIXS can be partitioned into three limiting cases depending on the momentum transfer and energy loss:[8]

1. For $\mathbf{q} \cdot \mathbf{r}_c \approx 1$ and $\omega/\omega_p \approx 1$, *valence excitations* such as plasmons or particle–hole pair excitations are probed. $\mathbf{r}_c$ is the typical inter–particle distance in the sample and ω_p is the plasmon frequency.

2. For $\omega \approx E_{\mathrm{B}}$, electrons from inner shells are excited. E_{B} is the binding energy of a core electron. These kind of experiments are often called *non–resonant x–ray Raman scattering* (NR–XRS) experiments.

3. $\mathbf{q} \cdot \mathbf{r}_c \gg 1$ and $\omega \gg E_{\mathrm{B}}$ is the limit of *Compton scattering* probing the ground state of the electron–momentum distribution.

This work focusses on the second case, i.e. on core–shell excitations studied by NRIXS.[9] Thus, the theoretical description and approaches to calculations will be discussed in the following.

In a core level non–resonant inelastic x–ray scattering process, the energy transfer ω is in the range of the binding energy of a tightly bound discrete core state, e.g. of K–, L–, and higher shells. Thus, an electron from this level can be excited into an unoccupied state above the Fermi energy E_{F} of the system. For an atom, the probability of the excitation depends on the density of (unoccupied) states (DOS) and on the matrix element for the excitation channel. According to Eqn. 2.4, the excitation operator is a complex exponential, which can be expanded in the Taylor series[10]

$$\langle \mathrm{f}|e^{i\mathbf{q}\cdot\mathbf{r}}|\mathrm{i}\rangle = i\langle \mathrm{f}|\mathbf{q}\cdot\mathbf{r}|\mathrm{i}\rangle - \frac{1}{2}\langle \mathrm{f}|\left(\mathbf{q}\cdot\mathbf{r}\right)^2|\mathrm{i}\rangle + \mathcal{O}((\mathbf{q}\cdot\mathbf{r})^3). \tag{2.5}$$

For small $\mathbf{q} \cdot \mathbf{r}$, the first term dominates giving rise to dipole transitions. It corresponds to the dipole term $\boldsymbol{\epsilon} \cdot \mathbf{r}$ in x–ray absorption spectroscopy (XAS) with the photon polarization vector $\boldsymbol{\epsilon}$.[11] Thus, in the dipole limit, NRIXS formally yields the same information for $\omega \approx E_{\mathrm{B}}$ as XAS for $\omega_1 \approx E_{\mathrm{B}}$. However, NRIXS allows a free choice of the incident energy whereas in XAS it is determined by the absorption edge. An increase of the momentum transfer leads to an amplification of the higher–order terms and thus of the multipole–transition contribution to the excitation spectrum.

---

[7] W. Schülke (1991), "Inelastic scattering by electronic excitations", *Handbook on synchrotron radiation, Vol. 3*, ed. by G.S. Brown and D.E. Moncton, North–Holland, Amsterdam.

[8] On an meV–scale also phonons can be probed by NRIXS. However, this is not discussed here.

[9] For simplicity, the study of core–shell excitations by NRIXS will be just addressed as *NRIXS* in the following.

[10] $|\mathrm{i}\rangle$ and $|\mathrm{f}\rangle$ are assumed to be orthogonal.

[11] Y. Mizuno and Y. Ohmura (1967), *J. Phys. Soc. Jpn.* **22**, 445; T. Suzuki (1967), *J. Phys. Soc. Jpn.* **22**, 1139.

2.1 Introduction to the theory of non–resonant inelastic x–ray scattering from core levels

Because the excitation of an electron induces a hole in the according core level, the dynamic structure factor is moreover influenced by the interaction of the excited electron with the core hole. In a single–particle theory, the final state $|\mathrm{f}\rangle$ can be interpreted as an electron above the Fermi level in the presence of a core hole, i.e. in a modified potential (final–state rule).[12] It will be discussed later[13] that, especially for ω close to E_B, the core hole–electron interaction is of importance and eventually should be treatened in a two–particle theory like the BSE formalism.[14]

In a solid, the local potential and therewith the DOS is influenced by the atoms in the environment of the excited atom. Thus, the potential is different from an isolated atom and a single atomic orbital is a poor approximation for a final state. Instead, the use of realistic scattering states for excitations is necessary. This can be fulfilled, e.g., by employing the density–functional theory (DFT).[15] Moreover, the wave function of the excited electron propagates from the excited atom into the solid and is scattered by the local potential of the neighboring atoms. This results in an auto–interference of the wave function and thus leads to a modulation of the excitation probability, i.e. of the NRIXS spectrum. This phenomenon is similar to the x–ray absorption fine structure (XAFS), though in NRIXS also non–dipole excitation channels have to be considered.

In the following, two different approaches to the numerical calculation of $S(\mathbf{q},\omega)$ for NRIXS will be outlined.

2.2 Real space multiple scattering approach

The program FEFF[16] provides an implementation for the calculation of the absorption function $\mu(\omega) \propto \omega S(\omega)$ for XAFS.[17] An adaptation to calculate $S(\mathbf{q},\omega)$ for non–resonant inelastic x–ray scattering has been presented by Soininen *et al.*[18] Both schemes are based on a multiple scattering Green's function formulation in real space.

---

[12] U. von Barth and G. Grossmann (1982), *Phys. Rev. B* **25**, 5150.

[13] See chapter 5.3.

[14] For a detailed discussion of the formalism, see: J.A. Soininen (2001), "Final–state interactions in inelastic x–ray scattering", PhD thesis, University of Helsinki; J.A. Soininen and E.L. Shirley (2001), *Phys. Rev. B* **64**, 165112; J.A. Soininen *et al.* (2001), *J. Phys.: Condens. Matter* **13**, 8039; J.A. Soininen *et al.* (2005), *Phys. Rev. B* **72**, 045136).

[15] W. Kohn and L.J. Sham (1965), *Phys. Rev.* **140**, A1133.

[16] FEFF–project home page: `leonardo.phys.washington.edu/feff`, see also A.L. Ankudinov *et al.* (2003), *Phys. Rev. B* **67**, 115120.

[17] See W. Schülke (2007), *Electron dynamics by inelastic x–ray scattering*, Oxford University Press, Eqn. (3.40).

[18] J.A. Soininen *et al.* (2005), *Phys. Rev. B* **72**, 045136.

2.2.1 Green's–function formulation

The Green's–function approach[19] is advantageous for the multiple–scattering problem since the explicit calculation of the final electron wave function $|\mathrm{f}\rangle$ is transformed into a more efficient calculation of the Green's function $G(E)$.[20] The dynamic structure factor for a core state $|\mathrm{i}\rangle$ can be expressed as a sum over the angular momenta $L=(l,m)$ and $L'=(l',m')$ of the initial and final states:[21]

$$S(\mathbf{q},\omega)=\sum_{L,L'} M_L(-\mathbf{q},E)\rho_{L,L'}(E)M_{L'}(\mathbf{q},E), \tag{2.6}$$

where $M_L(\mathbf{q},E)=\langle \mathrm{R_L(E)}|e^{i\mathbf{q}\cdot\mathbf{r}}|\mathrm{i}\rangle$ are the transition matrices with scattering states $R_L(E)$ of the embedded atom. $\rho_{L,L'}(E)=-\frac{1}{\pi}\Im\left(G_{L,L'}(E)\right)$ is the multiple–scattering matrix in terms of the final–state electron Green's function $G(E)=(E-H+i\Gamma)^{-1}$.[22] $H=H_0+\sum\limits_n v_n$ is the one–electron Hamiltonian with the free electron Hamiltonian H_0 and the scattering potentials v_n at atomic site n. Γ is the inverse lifetime of the core state. $G(E)$ can be calculated from the Green's function of a free electron $G^0(E)$ by an implicit functional Dyson equation:

$$\begin{aligned} G &= G^0+\sum_n G^0 v_n G \\ &= G^0+\sum_n G^0 t_n G^0+\sum_{n\neq m} G^0 t_n G^0 t_m G^0+\ldots, \end{aligned} \tag{2.7}$$

where all multiple scattering at a given site n is summed up in the scattering matrix $t_n=v_n+v_nG^0t_n$.

2.2.2 Full multiple scattering and the path expansion

For excitation energies well above the absorption threshold,[23] which in XAFS is the region of the extended x–ray absorption fine structure (EXAFS), the energy of the excited electron is high and therefore the scattering interaction between the photons and the electrons in the system is weak, i.e., the eigenvalues of G^0T are small.[24] The expansion of the Dyson equation (2.7) then quickly converges and can be stopped after a finite number of iterations:

$$G=\left[\sum_{n=0}^{N}\left(G^0T\right)^n\right]G^0+\mathcal{O}\left(\left(G^0T\right)^{N+1}\right). \tag{2.8}$$

---

[19] See, e.g., S. Doniach and E.H. Sondheimer (1998), *Green's functions for solid state physicists*, Imperial College Press, London.

[20] It is $\Im(G(E))=\sum\limits_{\mathrm{f}}|\mathrm{f}\rangle\langle\mathrm{f}|\delta(E-E_{\mathrm{f}})$. E_{f} is the energy of final state $|\mathrm{f}\rangle$.

[21] J.A. Soininen *et al.* (2005), *Phys. Rev. B* **72**, 045136.

[22] For simplicity, the angular momenta are omitted here and in the following.

[23] E_{B} will be called *absorption edge* or *absorption threshold* even though a scattering and not an absorption process is considered.

[24] It is $T=\sum\limits_n t_n$ the total scattering matrix, where the diagonal elements of G^0 are assumed to be zero.

This is called the *path expansion.* Close to the absorption edge, the scattering of the electron wave function is strong and multiple scattering of high orders become important. The *full multiple scattering* (FMS) Green's function can then be calculated using the relation

$$G = \left(1 - G^0 T\right)^{-1} G^0, \tag{2.9}$$

which comes along with a numerically extensive matrix inversion. However, due to the small kinetic energy of the excited electrons, the mean free path of their wave function into the solid is small and only a rather small number of surrounding atoms has to be taken into account.[25] Both methods have to be applied for large energy range calculations. For energy points within about the first 40 eV above the absorption edge, the full matrix has to be inverted. For energy losses of 100–1000 eV, path expansion is the method of choice. In between, both approximations should show an overlap.

2.2.3 Key approximations

With the ab–initio code FEFF and its adaptation to NRIXS, calculations of theoretical spectra can be performed from arbitrary atomic coordinates without periodic boundary conditions. The implementations contain several numerical simplifications for the absorption and scattering problem. A brief overview of the key approximations and their effect on the results will be given now.

Finite atomic clusters

Due to the abdication of periodic boundary conditions, the theoretical spectra can only be calculated for a finite cluster of atoms. This typically only leads to a broadening of the spectra, but it can also result in a miscalculation of the fine structure. The error can be estimated by a successive calculation of a spectrum, beginning with a small and ending up with a larger cluster where the spectra show convergence. Calculations of the silicon $\mathrm{L_{II}}$–edge for different cluster sizes are presented in Fig. 2.2 as an example. However, the numerical effort for the calculations typically scales as $N^{2.5}$, where N is the number of atoms in the cluster.[26] Also the computer memory needed for the calculations grows strongly with increasing cluster size. Thus, the cluster size is a compromise between finite–size errors, memory demand and computing time. This can make the calculation with FEFF unfeasible for certain compounds. J.J. Kas *et al.*[27] report that for diamond, the spectra calculated by FEFF are not fully converged for clusters up to even 500 atoms.

---

[25] Anyway, one should note that especially for the very near edge structure a sufficient size of the cluster is crucial.

[26] A.L. Ankudinov *et al.* (2002), *Phys. Rev. B* **65**, 104107.

[27] J.J. Kas *et al.* (2007), *Phys. Rev. B* **76**, 195116.

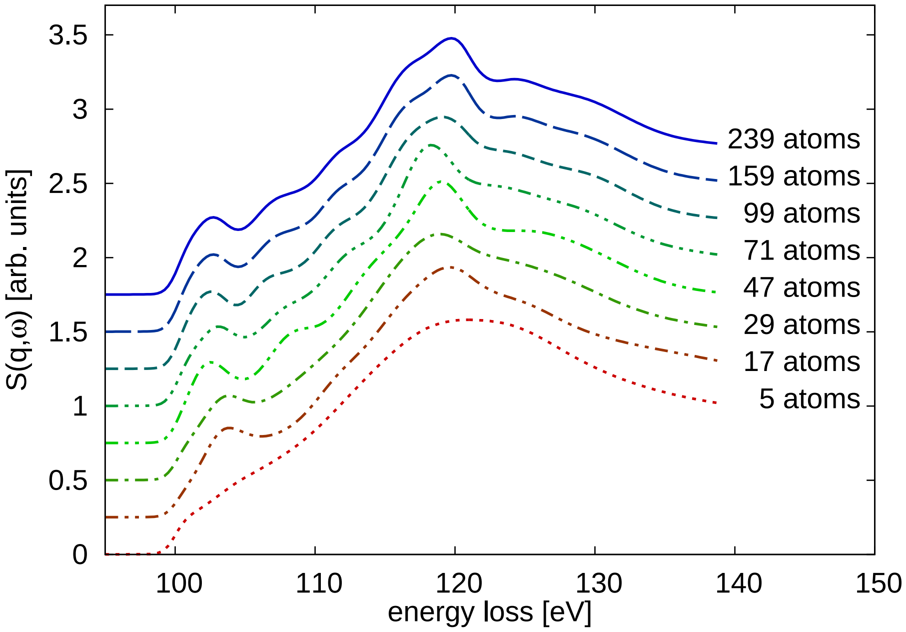

Figure 2.2: Convergence of FEFF calculations for different cluster sizes in the case of the silicon L_{II}–edge. The spectra are shifted vertically for clarity.

Self–consistent muffin–tin potential

Whereas the use of atomic orbitals as scattering potential can be sufficient for EXAFS calculations, Ankudinov *et al.*[28] have shown that a self–consistent core–potential calculation is necessary for the proper description of the near–edge structure of XAFS. FEFF supports an iterative calculation of the common potential for a given cluster of atoms to achieve self–consistency. However, the muffin–tin approximation[29] is used so that the basis for the calculation is not a space–filling full atomic potential. The potential is expanded into spherical harmonics in a sphere around each atom and the potential in the interstitial space between the partly overlapping spheres is approximated by a constant. Phase factors are determined so that the wave functions are continuous at the boundaries of the spheres. The strong simplification of the interstitial potential leads to inaccuracies, especially for compounds with large atomic distances such as tetrahedrally coordinated oxides.[30] Alternative approaches for the calculation of XAFS spectra beyond the muffin–tin approximation have been developed.[31]

---

[28] A.L. Ankudinov *et al.* (1998*a*), *Phys. Rev. B* **58**, 7565.

[29] A. Gonis and W.H. Butler (2000), *Multiple Scattering in Solids*, Springer, New York, chapter 5.

[30] A.R. Williams and J. van W. Morgan (1972), *J. Phys. C: Solid State Phys.* **5**, L293.

[31] K. Hatada *et al.* (2007), *Phys. Rev. B* **76**, 060102(R); Y. Joly (2001), *Phys. Rev. B* **63**, 125120; J.A. Soininen and E.L. Shirley (2001), *Phys. Rev. B* **64**, 165112; M. Taillefumier *et al.* (2002), *Phys. Rev. B* **66**, 195107.

Finite angular momentum

According to the interaction operator $\boldsymbol{\epsilon} \cdot \mathbf{r}$, only dipole excitations are allowed in an x–ray absorption process. Therefore, if the core state of an excited electron is of the angular momentum l', only final states $|l = l' \pm 1\rangle$ are allowed. In NRIXS, the multipole excitation operator can be expanded into spherical harmonics

$$e^{i\mathbf{q}\cdot\mathbf{r}} = 4\pi \sum_{l,m} i^l j_l(qr) Y^*_{lm}(\mathbf{e}_q) Y_{lm}(\mathbf{e}_r), \tag{2.10}$$

where $\mathbf{e}_q = \mathbf{q}/q$ and $\mathbf{e}_r = \mathbf{r}/r$. Hence, for any finite momentum transfer all excitation channels can contribute. However, depending on the atomic number Z of the studied elements, the contributions of terms with $l > 2$ are often negligible.[32]

Self–energy and core hole–electron interaction

The electron–electron interaction is described by the self–energy term. In the FEFF program, different approximations are implemented. The most important are the Hedin–Lundqvist[33] and the Dirac–Hara[34] approximation and a partially non–local model, in which core electrons are treated within Dirac–Fock and valence electrons within Hedin–Lundqvist approximation.[35]

The core–hole interaction can be taken into account by the *final–state rule*,[36] i.e., the electron excitation is calculated for a potential with a static core hole. Alternatively, the core hole can be neglected, which is also called the *initial–state rule*.[37] Dynamical two–particle or collective effects, which are disregarded in the final– and initial–state rule, require a treatment in, e.g., time dependent local density approximation (TDLDA).[38] Such an implementation in TDLDA is included in the current version[39] of the RSMS approach FEFF8.4. However, it is not available for the q–dependent RSMS code for the calculation of NRIXS spectra.

2.3 Decomposition of experimental NRIXS spectra

The measurement of the electron density of states can yield substantial information on the electronic properties of a material. Recently, Soininen *et al.*[40] showed that the core–excited

---

[32] It is referred to the decompositions of calculated NRIXS spectra shown in chapter 5.3.

[33] L. Hedin (1965), *Phys. Rev.* **139**, A796.

[34] P.A.M. Dirac (1930), *Proc. Camb. Phil. Soc.* **26**, 376.

[35] A.L. Ankudinov and J.J. Rehr (1997), *J. Phys. IV France* **7**, C2.

[36] U. von Barth and G. Grossmann (1982), *Phys. Rev. B* **25**, 5150.

[37] J.J. Rehr *et al.* (2005), *Physica Scripta* **T115**, 207.

[38] A. Zangwill and P. Soven (1980), *Phys. Rev. A* **21**, 1561.

[39] A.L. Ankudinov *et al.* (2003), *Phys. Rev. B* **67**, 115120.

[40] J.A. Soininen *et al.* (2006), *J. Phys.: Cond. Mat.* **18**, 7327.

electron l–DOS[41] $\rho_l(E)$ can be calculated from experimental NRIXS spectra for different momentum transfers employing equation (2.6). After directional averaging it is

$$S(q,\omega) = \sum_l (2l+1)\,|M_l(q,E)|^2\,\rho_l(E). \tag{2.11}$$

The matrix elements $M_l(\mathbf{q},E)$ can be approximated numerically, e.g. as done in the q–dependent adaptation of FEFF.[42] $\rho_l(E)$ can therefore be calculated by solving coupled linear equations for a set of spectra measured for different momentum transfer q_n. A comparison of the extracted $\rho_l(E)$ for the boron K–edge in MgB_2 to a calculated l–DOS shows very good agreement.[43]

2.4 Conclusions and outlook

In the view of ab–initio schemes, the calculation of q–dependent NRIXS spectra has made enormous progress during the past years. The interpretation of experimental spectra from solids profited significantly by the development of the FEFF adaptation and the BSE approach as, e.g., for beryllium,[44] or pure[45] and aluminum–doped[46] MgB_2. Another approach based on the StoBe–deMon code[47] employing transition potential approximation and Gaussian–like basis set within Kohn–Sham DFT has been developed for molecules and was successfully applied to calculate spectra of aromatic hydrocarbons and polyfluorene.[48] Comparisons of such calculations with experimental results allow the distinction between different excitation channels and therefore can give insight into the local electronic structure of the excited atom concerning, e.g., hybridization or charge transfer. Also the excitation process itself can be studied by comparison with theory, for instance regarding the core–hole screening.

However, certain applications are not yet feasible with today's available software. The muffin–tin approximation in the RSMS approach does not yield good results for compounds with large interatomic distances as it is the case for, e.g., tetrahedrally coordinated oxides. Full–potential approaches exist but are not feasible for NRIXS[49] or for large unit cells.[50]

---

[41] Projected density of states with respect to the angular momentum of the final state.

[42] J.A. Soininen *et al.* (2005), *Phys. Rev. B* **72**, 045136.

[43] J.A. Soininen *et al.* (2006), *J. Phys.: Cond. Mat.* **18**, 7327.

[44] C. Sternemann *et al.* (2003), *Phys. Rev. B* **68**, 035111.

[45] A. Mattila *et al.* (2005), *Phys. Rev. Lett.* **94**, 247003.

[46] A. Mattila (2007), "Studies of electronic structure by x–ray Raman and emission spectroscopy: applications to MgB_2 superconductors and high pressure physics", PhD thesis, University of Helsinki; A. Mattila *et al.*, "Electron hole counts in Al substituted MgB_2 from x-ray Raman scattering", submitted to Phys. Rev. B.

[47] K. Hermann *et al.* (2005), *StoBe Software*, 2005.

[48] A. Sakko *et al.* (2007), *Phys. Rev. B* **76**, 205115.

[49] E.g., the FDMNES code: Y. Joly (2001), *Phys. Rev. B* **63**, 125120.

[50] This is the case for the BSE approach.

Moreover, the study of giant resonances with NRIXS, as presented in chapter 7, calls for a q–dependent FEFF approach accounting for dynamical effects.

For a meaningful comparison of calculated spectra with an experiment for complex materials, the computational approaches have to be tested for simple and well–known systems to give an appropriate interpretation of the spectra. Therefore, a detailed analysis of calculations for elemental silicon, magnesium and sodium is presented in chapter 5 especially discussing the limits and advantages of the RSMS approach. This survey is a prerequisite for the study of complex compounds as presented later on in this work. First and foremost, experimental issues are addressed in the two following chapters, i.e. the principle layout of an NRIXS experiment and an algorithm for the proper extraction of q–dependent NRIXS spectra.

Chapter 3

Experimental setups for non–resonant inelastic x–ray scattering

This chapter deals with the experimental setups employed for the experiments presented in this work. At first, the key components of a general NRIXS–experiment setup are discussed. The special setups for beamlines ID16 (ESRF), BL12XU (SPring–8), and 20–ID (APS), at which the experiments have been performed, are presented next. Finally, the diamond–anvil cell used for the high–pressure experiments will be introduced. A table of the experimental parameters of all measurements presented in this work is given in Appendix A. Details for the preparation of the samples and the sample environments are given in chapters 4–7, in which the according experiments are discussed.

3.1 General remarks

For the accomplishment of NRIXS experiments, the x–ray source and the experimental setup have to fulfill certain requirements. Due to the low total cross section of NRIXS, a high photon flux at typical energies around 6–15 keV is required. The energy of the incident x–ray beam (or the energy of the analyzer unit) and the scattering angle have to be tunable to access different energy and momentum transfers respectively. In addition to that, a small focus[1] of the x–ray beam at the sample position is necessary for experiments in special sample environments. Third generation synchrotron sources matching these requirements are ESRF in Grenoble, France, SPring–8 in Nishi–Harima, Japan, and APS in Argonne, US.

The total energy resolution of standard experiments ranges between 0.7 and 1.5 eV. Nowadays, one can even achieve an energy resolution below 200 meV[2] or below 30 meV,[3] the latter by means of dispersion compensation using a pixel detector. The experimental

---

[1] Typically less than $100 \times 100\,\mu\text{m}^2$ spot size.

[2] Y.Q. Cai *et al.* (2004), *AIP Conf. Proc.* **705**, 340; J.P. Hill *et al.* (2007), *J. Synch. Rad.* **14**, 361.

[3] S. Huotari *et al.* (2005), *J. Synch. Rad.* **12**, 467.

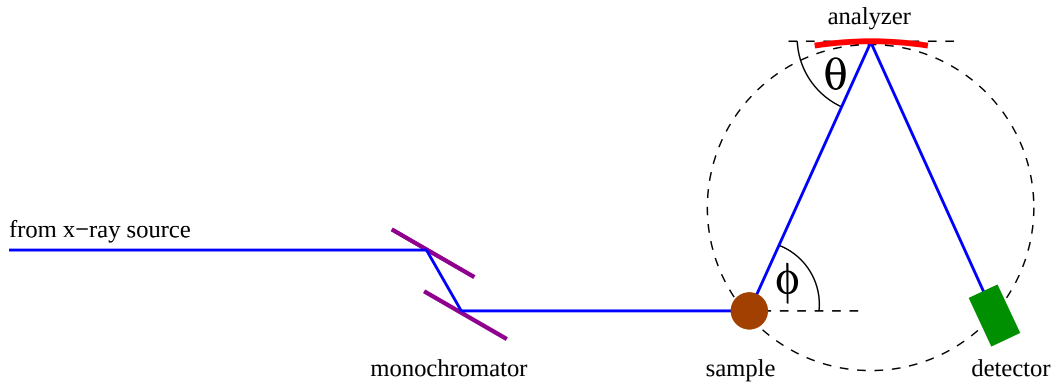

Figure 3.1: Rowland setup: The x–ray beam from the synchrotron is monochromatized by the monochromator (magenta) before impinging the sample (brown). The momentum transfer is determined by the scattering angle ϕ. In Rowland geometry, the sample, the analyzer crystal (red) and the detector (green) are located on the so–called Rowland circle.

energy broadening ΔE has to be smaller than the width of the expected fine structure. For the excitations studied in this work, an energy resolution of about 1 eV is typically appropriate.

A widely used analyzing scheme for NRIXS experiments to achieve high resolution with sufficient flux is the so–called *Rowland circle geometry* shown in Fig. 3.1. Here, the sample, the analyzer crystal, and the detector are positioned on a common circle. The analyzer is a bent crystal focussing the x–rays into the detector under a certain scattering angle. For a better energy resolution, the analyzer Bragg angle θ is usually chosen close to 90°. However, different energies can fulfill the Bragg condition for scattering originating from different parts of the sample. In the Rowland geometry, these contributions are projected on different spots on the Rowland circle so that energy resolution can be increased further using a position–sensitive detector. The momentum transfer q is determined by the angle ϕ between the incident and the scattered beam towards the position of the analyzer. The measurements themselves can be performed in two ways. Either the analyzer energy is changed for a fixed incident energy or the incident energy is scanned with a fixed analyzer energy. The latter setup is the so–called *inverse geometry*, which has been used in all experiments presented in this work.

3.2 Special beamline setups

The experiments presented in this work have been carried out at the beamlines ID16 of ESRF, BL12XU of SPring–8 and 20–ID of APS. An overview of the respective setups of these beamlines will be given in the following.

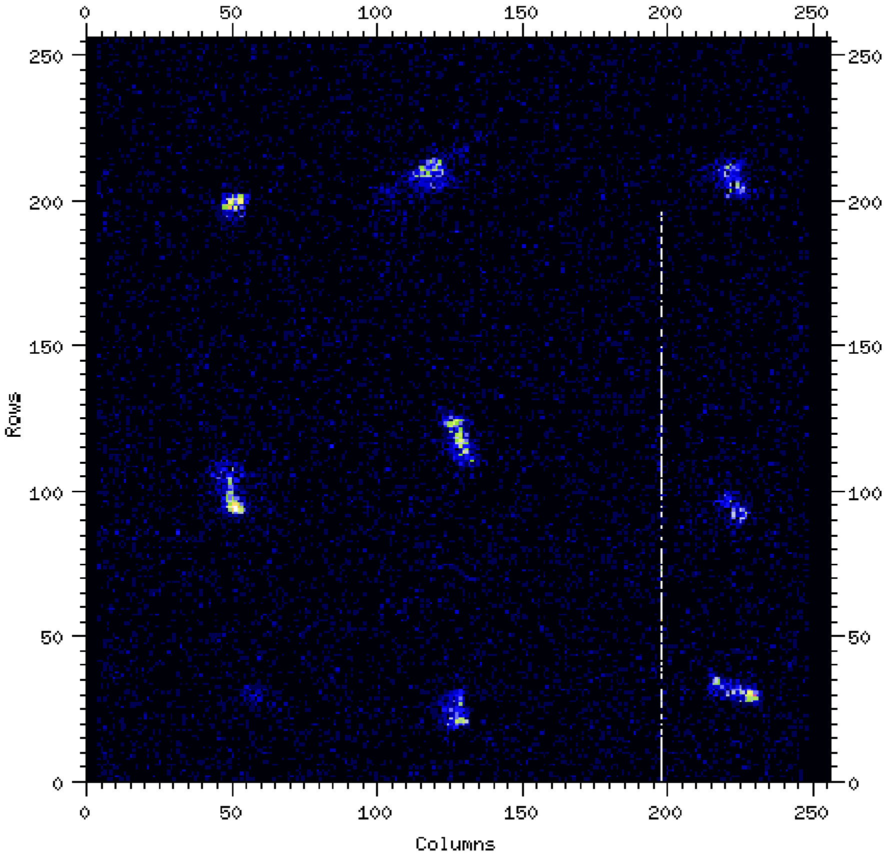

Figure 3.2: Image of the Medipix pixel detector in the current ESRF NRIXS setup. The nine spots of the analyzer crystals are focussed on different positions of the detector. The white pixels in column 198 are defective.

3.2.1 ID16 at ESRF

The x–ray source of beamline ID16 at the ESRF 6 GeV storage ring is a row of three U35 undulators. The white beam is monochromatized by a Si(111) crystal, which can be combined with a Si(220) channel–cut crystal. In 2006, a new NRIXS multi–analyzer setup in Rowland geometry was installed. It consists of nine analyzer crystals on a 1 m diameter Rowland circle focussing the x–rays to nine spots on a 256 × 256 Medipix[4] pixel detector as shown in Fig. 3.2.[5] Since bending leads to strain within the crystal lattice and therefore to a broadening of the Bragg reflection for high energy resolution experiments, diced analyzer crystals can be used.[6] However, in the experiments presented in chapter 7, an energy

---

[4] X. Llopart *et al.* (2002), *IEEE Trans. Nucl. Sci.* **49**, 2279.

[5] This setup will be referred to as the *Medipix setup*.

[6] These crystals consist of matrices of small unbent crystal dices. The dices are oriented with a small tilt towards each other leading to an overall curvature and a focussing of the beam. The crystals themself remain undistorted and show very narrow Bragg reflections.

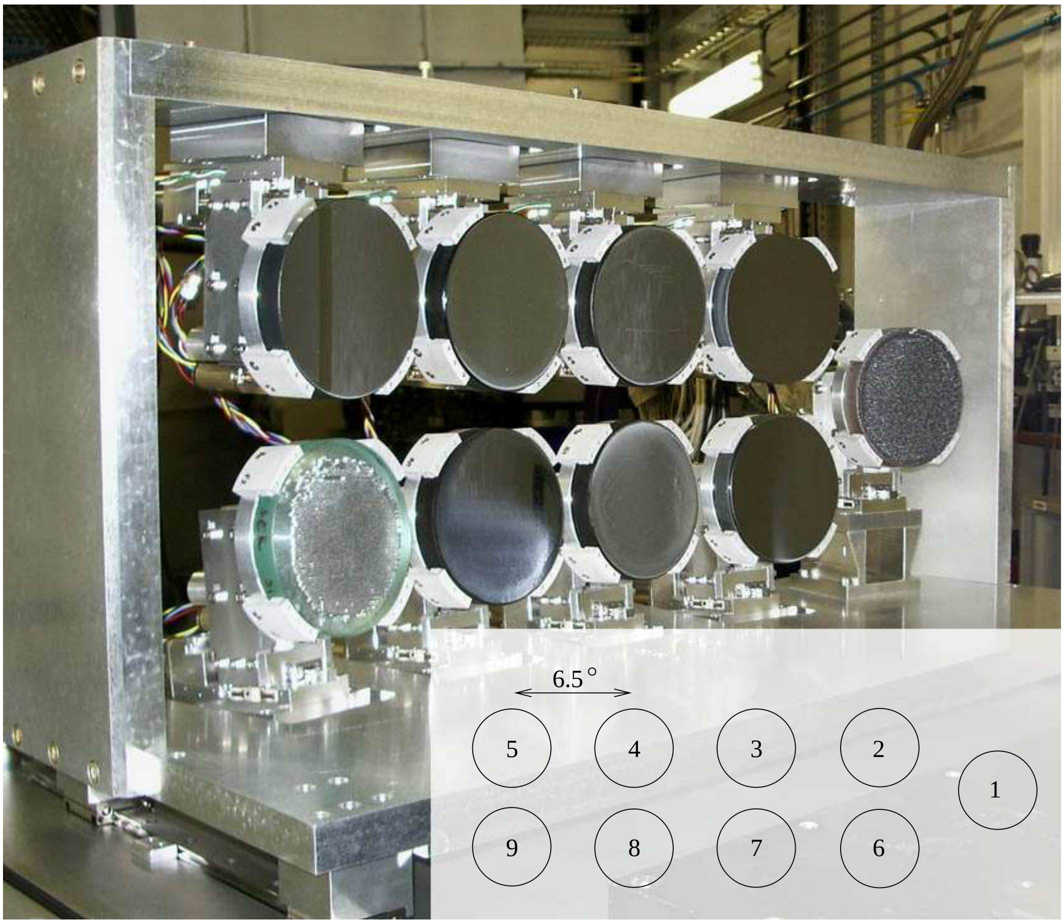

Figure 3.3: ESRF ID16 analyzer arrangement. Five scattering angles are covered with an angular distance of 6.5° each.

resolution of 1 eV was sufficient and regular bent Si(660) analyzer crystals were used. The spot size of the incident x–ray beam was $50 \times 100\,\mu\text{m}^2$ (V×H). The nine analyzers are arranged as shown in Fig. 3.3 covering five scattering angles of 6.5° distance each, i.e. with a total angular spread of 26°. For four angles, the signal from two detectors each can be added to increase the effective solid angle of detection without loss of q–resolution. The energy– and q–resolution can be increased by partly covering the analyzer crystals and therewith reducing the accepted solid scattering angle. However, this also decreases the signal so that an optimum has to be found concerning resolution and count rate.

In addition to the simultaneous acquisition of five momentum transfers and high energy and q–resolution, the setup also supports a real–space resolution in terms of the scattering volume. As illustrated in Fig. 3.4, the scattering from different parts within the sample

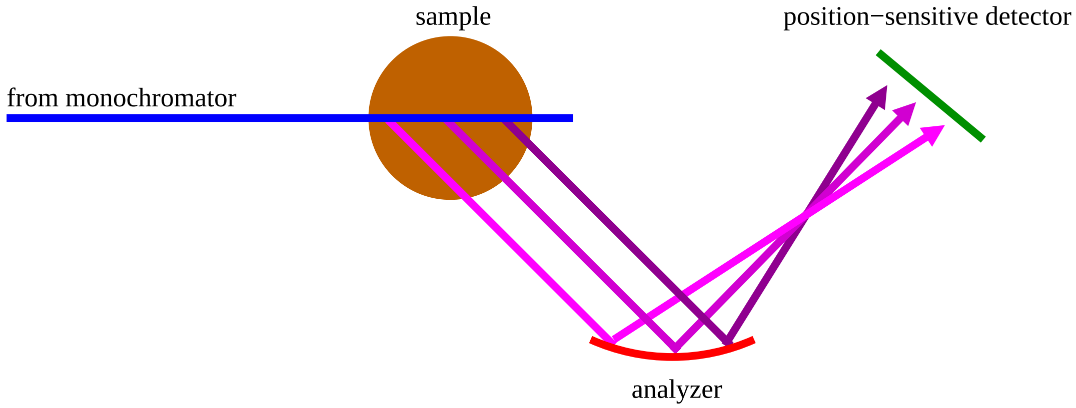

Figure 3.4: Discrimination of signals from different sample positions using the Medipix detector. The incident x–ray beam (blue) is scattered while penetrating the sample (brown). Thus, scattering from different parts of the sample falls onto the analyzer and is finally detected by the Medipix with spatial resolution.

is detected by different pixels on the detector. Thus, the scattering volume can be discriminated by software masking only the pixels of the scattering volume of interest. Such a spatial resolution allows the study of inhomogeneous samples and the discrimination of the sample in complex environments. In high–pressure experiments for instance, the parasitic scattering from the gasket complicates the study of the sample spectrum. With the presented setup, the gasket signal can be separated from the sample scattering. The importance of such a discrimination will be discussed further in chapter 7.

Some of the experiments[7] at ID16 have been performed using the former 1 m Rowland setup with a point detector. These experiments have been carried out at 9.89 keV using a Si(555) analyzer and at 12.4 keV using a Ge(880) analyzer. With the Si(111) monochromator the effective energy resolution of both setups is about 1.5 eV. An energy resolution of 0.8 eV could be achieved by means of the secondary Si(220) channel–cut monochromator. The incident beam was collimated to different spot sizes as listed in Tab. A.2.

3.2.2 BL12XU at Spring–8

The x–ray source of the Spring–8 8 GeV storage ring beamline BL12XU is a 4.5 m long U32 undulator. A Si(111) double crystal is used as monochromator. The setup used for the high–pressure experiments consists of a 2 m Rowland circle with a 15–element multiple analyzer system arranged in five columns with three analyzer mounts each so that for one scattering angle the signal from three analyzers can be summed up. However, due to the geometry of the diamond–anvil cell[8] used during the experiment, only the central

---

[7] See setup *d* in Tab. A.2.

[8] See chapter 7.5.

analyzer could be used. Since a spatial resolution as in the Medipix setup at ESRF ID16 is not yet available at BL12XU, focussing of the incident beam and collimation of the scattering is crucial for high–pressure experiments. The incident beam was focussed to a spot of $20 \times 25\,\mu\mathrm{m}^2$ (V × H) using Kirkpatrick–Baez (KB) mirrors[9] and a pinhole of $50\,\mu$m diameter. The signal from the sample could be discriminated in parts from the scattering of the beryllium gasket in which the sample was embedded by a $50 \times 500\,\mu\mathrm{m}^2$ tungsten slit between the sample and the analyzer. Fig. 3.5 shows the top and side view of the high–pressure setup and the path of the beam. With the Si(777) analyzer at 13.9 keV and the Si(111) double crystal monochromator, an energy resolution of 2 eV could be achieved.

3.2.3 XOR/PNC 20–ID at APS

At the 20–ID beamline of APS, a setup employing different scattering angles is installed for the simultaneous measurement of NRIXS spectra for multiple q. A detailed overview on this so–called LERIX[10] spectrometer is given by Fister *et al.*[11] In the actual stage of expansion, 19 Si(555) analyzers are arranged on a semicircle of 1 m radius with scattering angles between 9° and 171° and a fixed analyzer energy of 9.89 keV. A photo of the spectrometer is shown in Fig. 3.6. The Rowland–circle plane is perpendicular to the polarization of the x–ray beam so that the measured intensity is independent with respect to the linear polarization factor. Therefore, also scattering angles close to 90° can be employed. Originating from an undulator source, the x–ray beam is monochromatized by a Si(111) double crystal monochromator so that in total an energy resolution of 1.5 eV can be achieved. The spot size of the incident beam at the sample position is $400 \times 100\,\mu\mathrm{m}^2$ (V×H). The spectrometer is designated for studies of the momentum–transfer dependence of NRIXS spectra with medium energy resolution. Since all spectra are collected at the same time, artefacts due to transients or beam damage can be excluded in the comparison of different q. However, the study of the q–dependence has been limited insofar that the NRIXS spectra have to be extracted from underlying particle–hole contributions or Compton scattering. In chapter 4, an algorithm will be presented, which has been developed during this work to systematically subtract these contributions from the spectra.

---

[9] P. Kirkpatrick and A.V. Baez (1948), *J. Opt. Soc. Am.* **38**, 766.

[10] Lower energy resolution inelastic x–ray scattering spectrometer.

[11] T.T. Fister *et al.* (2006*b*), *Rev. Sci. Instr.* **77**, 063901.

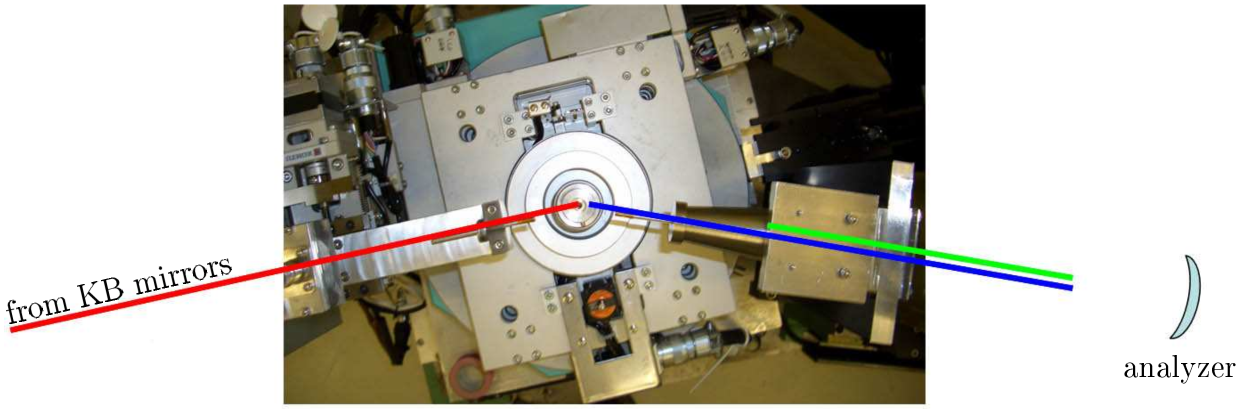

(a) High–pressure setup at SPring–8 BL12XU, top view.

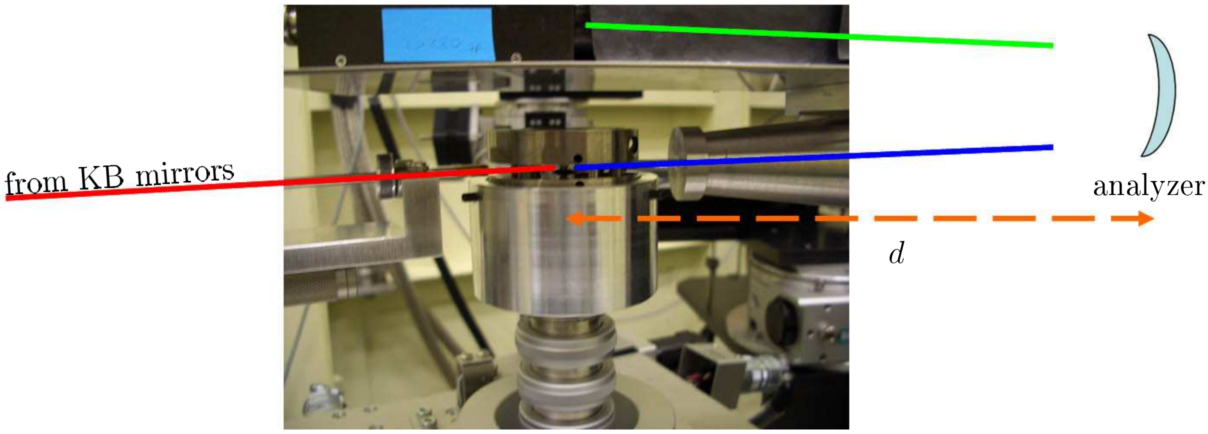

(b) High–pressure setup at SPring–8 BL12XU, side view.

Figure 3.5: SPring–8 BL12XU high–pressure setup. The monochromatized and focussed beam (red) is passing a pinhole before impinging the sample. The scattered beam (blue) is collimated by a tungsten slit close to the beryllium gasket to minimize parasitic scattering from the beryllium. The analyzer crystal reflects the beam (green) by a Bragg reflection at an angle close to 90°. The distance d between sample and analyzer (orange) is 2 m.

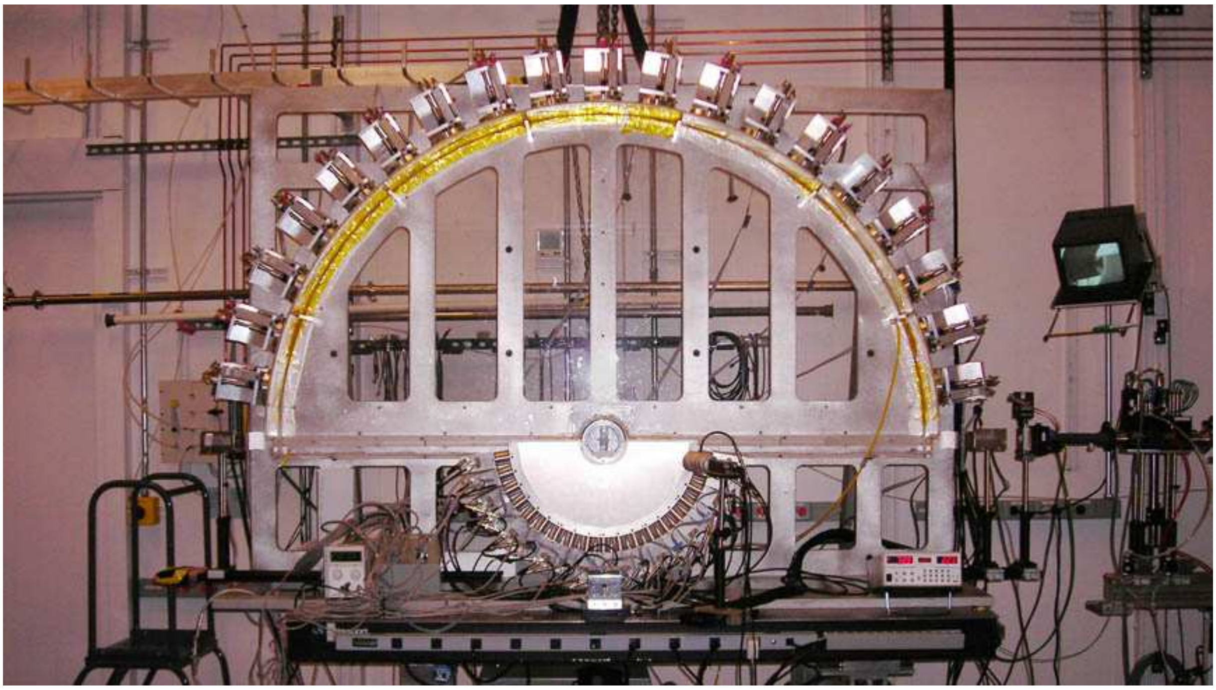

Figure 3.6: APS 20–ID LERIX spectrometer. The monochromatized beam enters the helium filled vessel on the right and impinges on the sample in the center. 19 analyzer crystals are aligned on a semicircle with Bragg angles close to 90°. The detectors are aligned on a smaller semicircle below the sample. (Photo: `http://www.pnc.aps.anl.gov`)

Chapter 4

A background–removal algorithm for non–resonant inelastic x–ray scattering spectra

The experimental setups for q–dependent NRIXS studies have become very sophisticated by using multiple analyzers in vertical scattering geometry or multiple–analyzer arrays in horizontal scattering geometry as presented in chapter 3. However, the distillation of the core contribution to $S(\mathbf{q}, \omega)$ from the raw experimental spectra is still a challenge. This is due to the fact that the core excitations of interest are usually superimposed by contributions of valence electrons or other core electrons. Therefore, an algorithm for subtraction of the scattering background to extract the relevant core–excitation spectrum has been developed and will be presented in this chapter. It is likely to be applicable to various samples because no theoretical calculations apart from tabulated Hartree–Fock core electron Compton profiles[1] are required. As an example, the algorithm is applied to extract the silicon L–edges in pure Si and the compound SiO_2 from a multiple–q NRIXS experiment conducted at beamline XOR/PNC 20–ID of the APS.

The chapter is organized as follows: After a brief overview on the measurements of the q–dependence in Si and SiO_2 NRIXS spectra, the theory important for the algorithm will be discussed. Energy–dependent corrections due to the experimental setup and the cross–section correction will be applied to the raw spectra. The experimental determination of the valence–electron contribution and the extraction of the silicon L–edges are then presented and exemplified for Si and SiO_2. Furthermore, the obtained silicon L–edges of Si and SiO_2 are compared with q–dependent calculations. A summary and a short outlook are given at the end of the chapter.

---

[1] F. Biggs *et al.* (1975), *Atomic Data Nuclear Tables* **16**, 201.

4.1 Experimental details

For the application of the background–removal algorithm, which will be presented in this chapter, NRIXS spectra have been recorded of the silicon L–edges in Si and SiO_2 for a broad range of momentum transfers. The experiment has been accomplished with the LERIX setup of the APS 20–ID.[2] The Si and SiO_2 powder samples[3] were pressed into pellets and aligned to the center of the analyzer circle. The incident angle was set to $\phi_i = 10°$ in reflection geometry so that the first two analyzers at $\theta = 9°$ and $\theta = 18°$ were partly or fully shadowed by the sample. The experimental parameters for the Si and SiO_2 experiment are given in Tab. A.2 (keys B_n). Spectra for a q–range from 1.25 a.u. to 5.34 a.u. have been recorded. For each sample, several single scans were performed and added up subsequently to exclude systematic errors during the measurement.[4] The added raw data of Si and SiO_2 for different scattering angles are shown in Fig. 4.1. The energy loss positions of the silicon $L_{II,III}$– (99.82/99.42 eV), L_I– (149.7 eV), and oxygen K– (543.1 eV) and L_I– (41.6 eV) edges are indicated by vertical lines. All spectra are vertically shifted with respect to their absolute value of momentum transfer calculated for the energy–loss positions of the silicon $L_{II,III}$–edges. The spectra are normalized to their peak–value.

4.2 Extraction algorithm for core electron excitations

In chapter 2, the principles of NRIXS theory have been outlined. Now, theoretical details shall be restated on a framework necessary for the algorithm. The double differential scattering cross section (DDSCS) can be expressed in terms of the dynamic structure factor $S(\mathbf{q}, \omega)$ as done in equation (2.3). In the limit of high momentum transfers, it can be expressed in terms of the so–called *Compton profile* $J(p_z)$:

$$\frac{d^2\sigma}{d\Omega d\omega} = r_0^2(\epsilon_1 \cdot \epsilon_2)\frac{\omega_2}{\omega_1}\frac{m}{q}J(p_z), \tag{4.1}$$

where $p_z = m/q\,\omega - q/2$ is the component of the scattered electron's momentum in the ground state parallel to the momentum transfer $\mathbf{q}$. Compton scattering provides access to the ground state electron momentum density distribution.[5]

Valence–electron excitations manifest themselves in the dynamic structure factor and transform from the typical plasmon and particle–hole excitation spectrum for low momentum transfer to the valence electron Compton profile at high momentum transfer. A

---

[2] See chapter 3.2.3.

[3] All samples were provided by A. Hohl, Institut für Materialwissenschaft, TU Darmstadt.

[4] This has also been done for all spectra shown in other chapters of this work.

[5] See, e.g., (2004), *X–ray Compton Scattering*, ed. by M.J. Cooper *et al.*, Oxford University Press or W. Schülke (2007), ***Electron dynamics by inelastic x–ray scattering***, Oxford University Press for a review on Compton scattering.

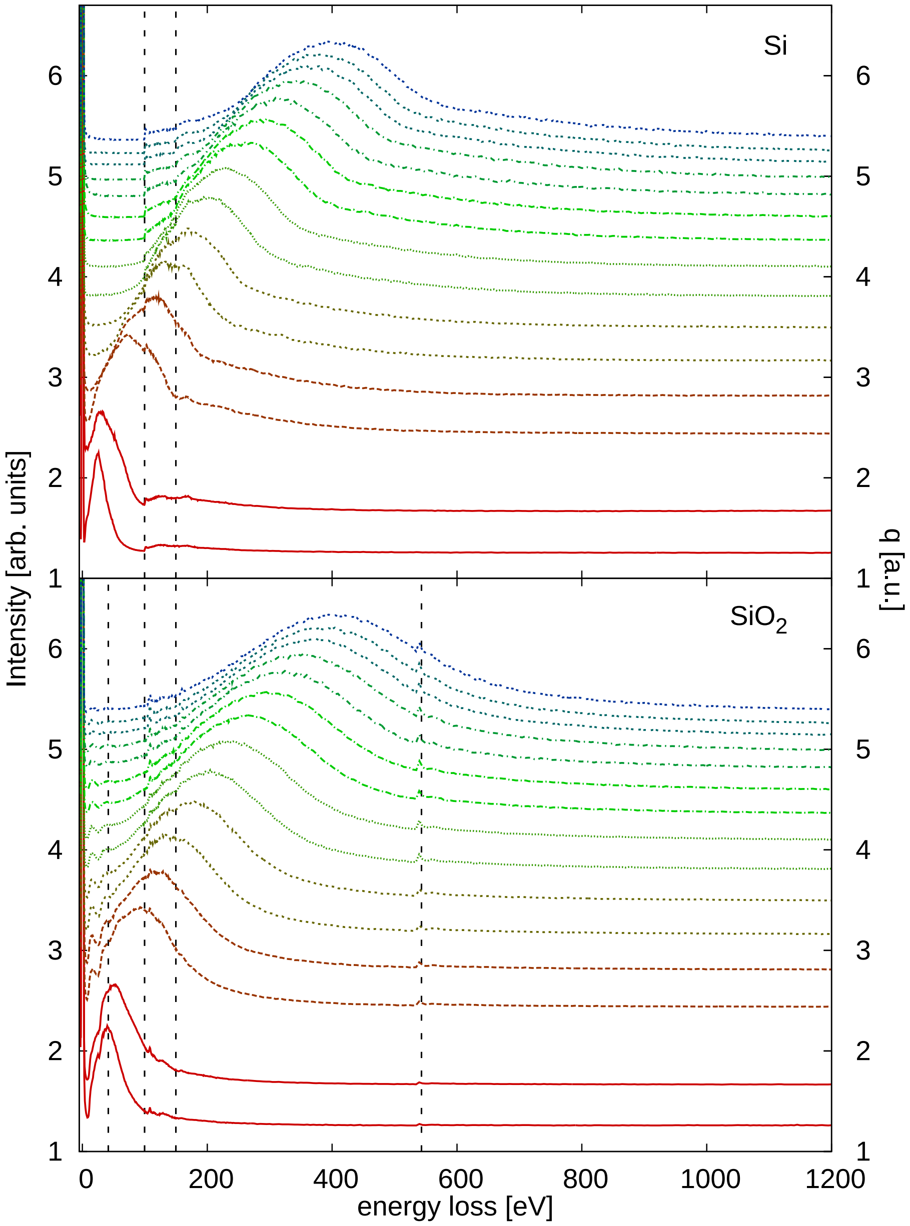

Figure 4.1: Raw NRIXS data of Si (top) and SiO$_2$ (bottom) for different momentum transfers. The spectra are vertically shifted with the axis of ordinates intercept at the according momentum transfer. For Si, the silicon L–edges are indicated by vertical lines. For SiO$_2$, also the positions of the oxygen K– and L$_\text{I}$–edges are shown.

calculation of the valence–electron contribution is difficult and not appropriate for an all–purpose extraction algorithm. Here, a model function has to be used to approximate the shape of the underlying valence–electron contribution. Within the Compton limit, the valence Compton profile can usually be extracted from the experimental data for a certain momentum–transfer value. This profile then properly reflects the valence–electron contribution to the NRIXS spectrum for higher momentum transfers. The core–electron contribution to the total NRIXS spectrum of an element or a compound is well described by atomic Hartree–Fock Compton profiles, which exist within impulse approximation[6] (IA) in tabulated form.[7] Such profiles can straightforwardly be included into a subtraction algorithm. Nevertheless, close to an absorption edge, where the corresponding core–electron contribution sets in, the spectrum is dominated by dynamical effects, the local environment of the excited atoms, and by their electronic structure. Thus, it shows significant deviations from the onset of a Hartree–Fock core electron Compton profile in the non–IA regime.

An algorithm scheme for the extraction of core–electron contributions to the NRIXS spectrum was developed and will be described in the following. Before such an absorption edge can be extracted, various energy–dependent corrections related to the experimental conditions have to be taken into account. These corrections will be shortly discussed, then the extraction of the valence electron Compton profile is described followed by a detailed demonstration of the silicon $L_{II,III}$ absorption edge extraction for the measured systems Si and SiO_2.

4.2.1 Energy–dependent corrections

The intensity measured in the detector has to be corrected for the background scattering, energy–dependent absorption of the incoming and scattered x–rays within the sample, and absorption of the incoming x–rays by, e.g., windows, foils, or air paths. Moreover, a cross–section correction has to be applied. Absorption and efficiency corrections might be necessary also for the monitor–detector signal. The appropriate energy–dependent corrections related to the LERIX setup are discussed in the following.

Absorption and self–absorption

In reflection geometry the correction for self–absorption of the incoming and scattered x–rays within a sample of thickness d is given by

$$I_{\mathrm{Re}} \propto I_0 \frac{1 - e^{-d(\mu_{\mathrm{i}}/\cos\phi_{\mathrm{i}} + \mu_{\mathrm{f}}/\cos\phi_{\mathrm{f}})}}{\mu_{\mathrm{i}}/\cos\phi_{\mathrm{i}} + \mu_{\mathrm{f}}/\cos\phi_{\mathrm{f}}}, \tag{4.2}$$

---

[6] P. Eisenberger and P.M. Platzman (1970), *Phys. Rev. A* **2**, 415.

[7] F. Biggs *et al.* (1975), *Atomic Data Nuclear Tables* **16**, 201.

where $\mu_{\mathrm{i/f}}$ are the absorption lengths for the incident and the analyzer energy, respectively. $\phi_{\mathrm{i/f}}$ are the corresponding scattering angles relative to the normal of the sample surface. For transmission geometry, the correction is

$$I_{\mathrm{Tr}} \propto I_0 \frac{e^{-d(\mu_{\mathrm{f}}/\cos\phi_{\mathrm{f}})} - e^{-d(\mu_{\mathrm{i}}/\cos\phi_{\mathrm{i}})}}{\mu_{\mathrm{i}}/\cos\phi_{\mathrm{i}} - \mu_{\mathrm{f}}/\cos\phi_{\mathrm{f}}}. \tag{4.3}$$

Further absorption, e.g. due to air, Be– or Kapton–windows in the beampath, can be accounted for by the simple transmission–correction factor

$$I_{\mathrm{Tr}} = I_0 e^{-d\mu_{\mathrm{i/f}}}. \tag{4.4}$$

This energy–dependent absorption correction has to be applied for the beampaths of the incident beam between the source of the normalization signal and the sample, because only the incident energy is varied in inverse geometry and the analyzed energy is kept constant. Corrections for the normalization detector itself have to be considered separately.

Compton cross section correction

For the extraction of the valence Compton contribution, the experimental Compton profile $J(p_z)$ has to be calculated from the DDSCS. In the non–relativistic limit, the Compton profile $J(p_z)$ is directly proportional to the DDSCS.[8] In the relativistic case, it needs to be corrected according to[9]

$$\frac{d^2\sigma}{d\Omega d\omega} = \frac{r_0^2}{2}\frac{\omega_2}{\omega_1}\chi(p_z)\frac{m}{q}J(p_z) \tag{4.5}$$

by the p_z–dependent[10]

$$\chi(p_z) = \frac{R}{R'} + \frac{R'}{R} - \sin^2\theta, \tag{4.6}$$

where θ is the scattering angle and the parameters R and R' are given by

$$\begin{aligned} R &= \omega_1\left(m - (\omega_1 - \omega_2\cos\theta)\frac{p_z}{q}\right), \qquad (4.7)\\ R' &= R - \omega_1\omega_2(1-\cos\theta). \end{aligned}$$

Fig. 4.2 shows the corrections due to the relativistic Compton cross section and the self–absorption in the sample. As typical for inverse geometry, both contributions compensate in parts. Fig. 4.2 further shows the absorption correction due to air and Kapton foils in the beampath.

---

[8] See Eqn. (4.1).

[9] P. Holm (1988), *Phys. Rev. A* **37**, 3706; R. Ribberfors (1975), *Phys. Rev. B* **12**, 2067.

[10] This is an approximation to R. Ribberfors (1975), *Phys. Rev. B* **12**, 2067, Eqn. (49).

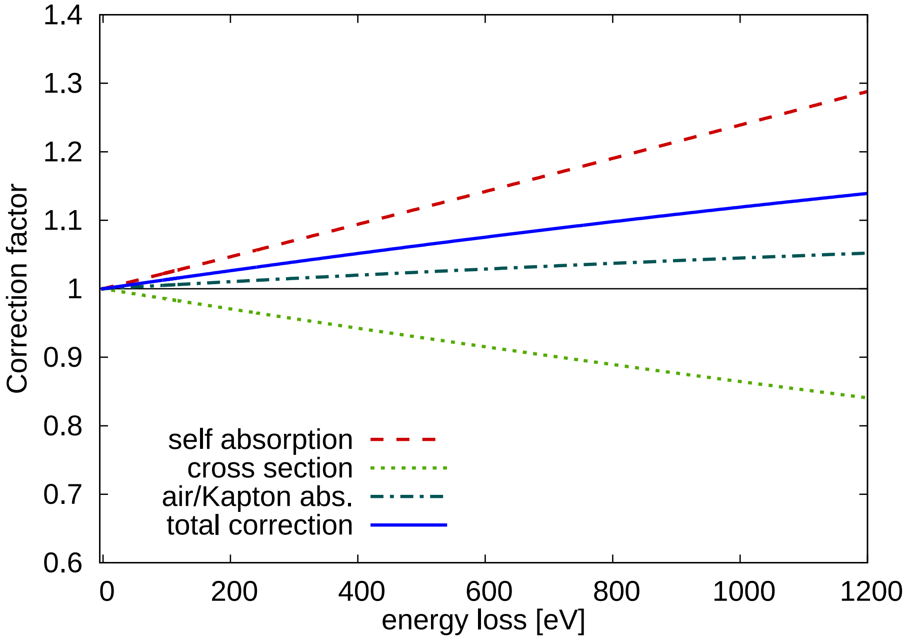

Figure 4.2: Energy–dependent correction factors due to absorption and relativistic Compton cross section corrections. The DDSCS has to be divided by the total correction to obtain the Compton profile $J(p_z)$.

Background

Parasitic scattering, e.g. from helium in the analyzer scattering path, leads to a background in the spectra, which in first approximation is assumed to be constant. For the estimation of the background level, scattering is recorded for energies below the quasi–elastic line. However, this often only yields an order of magnitude of the actual background. Since for energy losses far away from absorption edges in the system, the Hartree–Fock Compton core profiles should match the experimental scattering intensity very well, the background can be refined by adjusting the spectra to the calculation in that energy regime.

4.2.2 Determination of the experimental valence electron Compton profile

The contribution of core electrons to the Compton profile can be approximated well by atomic Hartree–Fock calculations. However, to model the valence electron Compton profile contributions adequately, more sophisticated calculations have to be used as discussed before. Nevertheless, this contribution can also be extracted from the experimental spectra, if — at a certain momentum transfer — the valence regime is not covered by an absorption edge. This should be possible for multi–q datasets as obtained with the LERIX setup. Fig. 4.3 shows the spectra of Si and SiO_2 for a momentum transfer of $q = 5.21$ a.u., at which the energy range of the valence–electron contribution extends beyond the onset of the silicon L–edges. For the separation of the valence profile from the core signal of the silicon L–edges (and the oxygen K–edge for SiO_2), an adequate description of the latter contribution is necessary. In the following, a scheme for modeling the core profile including its asymmetry will be discussed. Furthermore, the valence electron Compton profile also shows an asymmetry, which has to be taken into account for the final extraction of the NRIXS signal.

The core contributions of the silicon L–shell have been modeled by corrected Hartree–Fock calculations: The non–relativistic Compton cross section in impulse approximation is a symmetric function in p_z–space with its maximum at $p_z = 0$. However, Holm *et al.*[11] have calculated the first corrections for the 1s–, 2s– and 2p–shells showing asymmetries in terms of p_z. Widths and strengths of the corrections[12] $J_1^{1s}(p_z)$, $J_1^{2s}(p_z)$ and $J_1^{2p}(p_z)$ have been normalized by comparing the maximum of the non–relativistic expression[13] with the maximum of the Hartree–Fock profile of the according shell. The q–dependent core asymmetry corrections (CA) for Si are then added to the symmetric Hartree–Fock profiles. The corrected core profile for Si shown in the top part of Fig. 4.3 shows good agreement both at the onset of the silicon L–edges and for an energy loss beyond 600 eV, at which the valence contribution has vanished. However, the asymmetry correction calculated by Holm *et al.* can lead to deviations in magnitude and overall shape between the experiment and the model for the core profile.[14] Thus, within the presented extraction scheme, a scaling factor can be applied to the core asymmetry to yield better agreement with the experiment. In case of Si and SiO_2, a value of 1.5 is used. More sophisticated theories for the core asymmetries, as presented by S. Huotari *et al.*,[15] yield a better description but are not suitable to be used in a straightforward extraction algorithm. For samples, for which simple asymmetry theories fail to describe the experimental observation, the core asymmetry can also be directly extracted from the experiment and parameterized by a phenomenological function. The question of q–dependence of such an ad–hoc extraction then remains unanswered. After normalization of the experimental spectrum and the corresponding core–electron contribution to the number of electrons in p_z–space, the valence contribution of the Compton profile can be extracted from the spectrum without free parameters apart from the constant background. Artefacts in the tail of the extracted valence profile due to the onset of the silicon L–edges can be smoothly removed by fitting a Pearson function[16] in this energy regime. For SiO_2, the core contribution consists of the silicon L_I–, $L_{II,III}$–

---

[11] P. Holm and R. Ribberfors (1989), *Phys. Rev. A* **40**, 6251.

[12] ibid., Eqns. 54&55.

[13] ibid., Eqns. 51&52.

[14] S. Huotari *et al.* (2001), *J. Phys. Chem. Solids* **62**, 2205.

[15] ibid.

[16] See Eqn. (4.9).

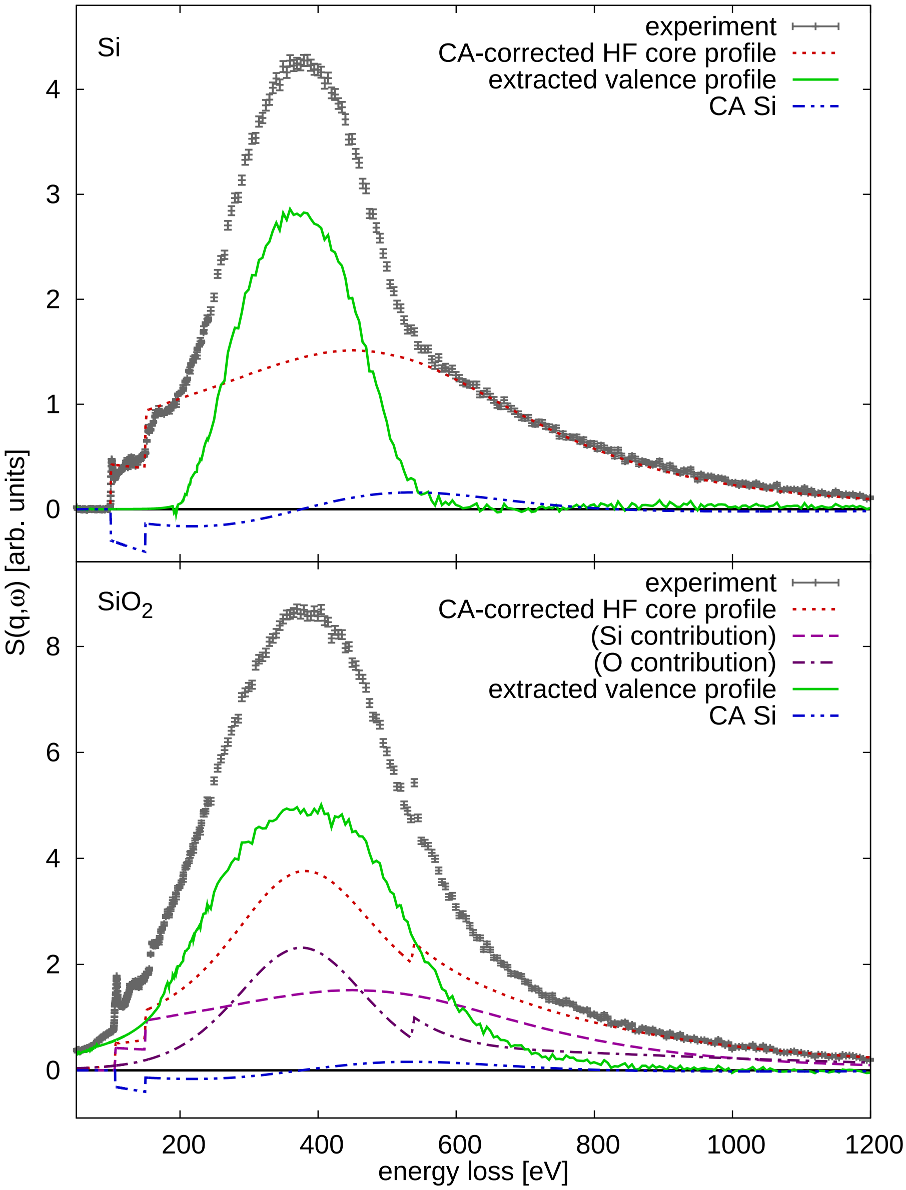

Figure 4.3: Extraction of the valence contribution to the Compton profile for Si (top) and SiO_2 (bottom) at q = 5.21 a.u. The asymmetry–corrected Hartree–Fock (HF) core contributions for silicon and oxygen are shown separately. For silicon, the correction to the non–relativistic Compton cross section (CA) is taken into account. The experimental spectra and the core profiles are normalized to the according number of electrons.

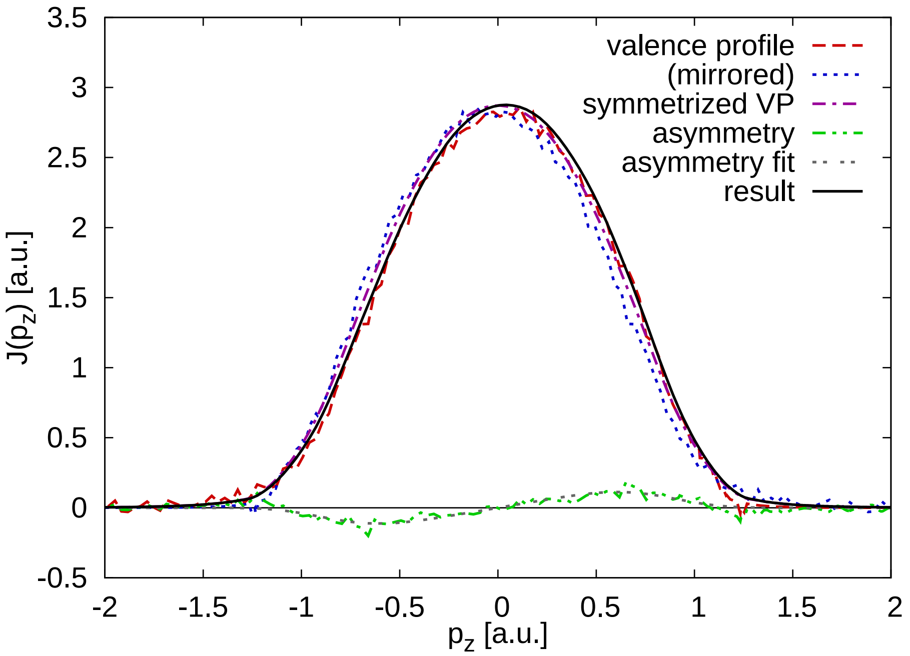

Figure 4.4: Asymmetry determination of the valence Compton profile. The spectrum is mirrored at $p_z = 0$. The asymmetry is then modeled as explained in the text. The resulting sum of the symmetrized valence profile and the modeled asymmetry is shown as well.

and oxygen L_I–edges. Thus, eight oxygen and four silicon valence electrons are assumed to contribute to the SiO_2 valence Compton profile. The valence profiles are then symmetrized with respect to $p_z = 0$ and smoothed by convolution with a Gaussian function. This leads to a further reduction of artefacts, especially in the tails of the profile. Employing the definition of p_z, the valence profiles can now be calculated for all momentum transfers.

The asymmetry of the valence Compton profiles[17] is modeled in p_z–space by the phenomenological function[18]

$$A(p_z) = \alpha_1 \tanh(p_z/\alpha_2) e^{-(p_z/\alpha_3)^4}, \tag{4.8}$$

as shown in Fig. 4.4 for Si. In a first approximation, this asymmetry is assumed to be independent of the momentum transfer and added to the symmetrized valence contributions for all q. A q–dependent modeling of an asymmetry of the valence profile is out of scope of this data treatment. The asymmetry–corrected valence profiles which are obtained from the extraction algorithm can now be used to discriminate the pure NRIXS spectrum of the silicon L–edges from the experimental spectra.

---

[17] S. Huotari *et al.* (2001), *J. Phys. Chem. Solids* **62**, 2205; C. Sternemann *et al.* (2000), *Phys. Rev. B* **62**, R7687.

[18] α_n are fitting parameters.

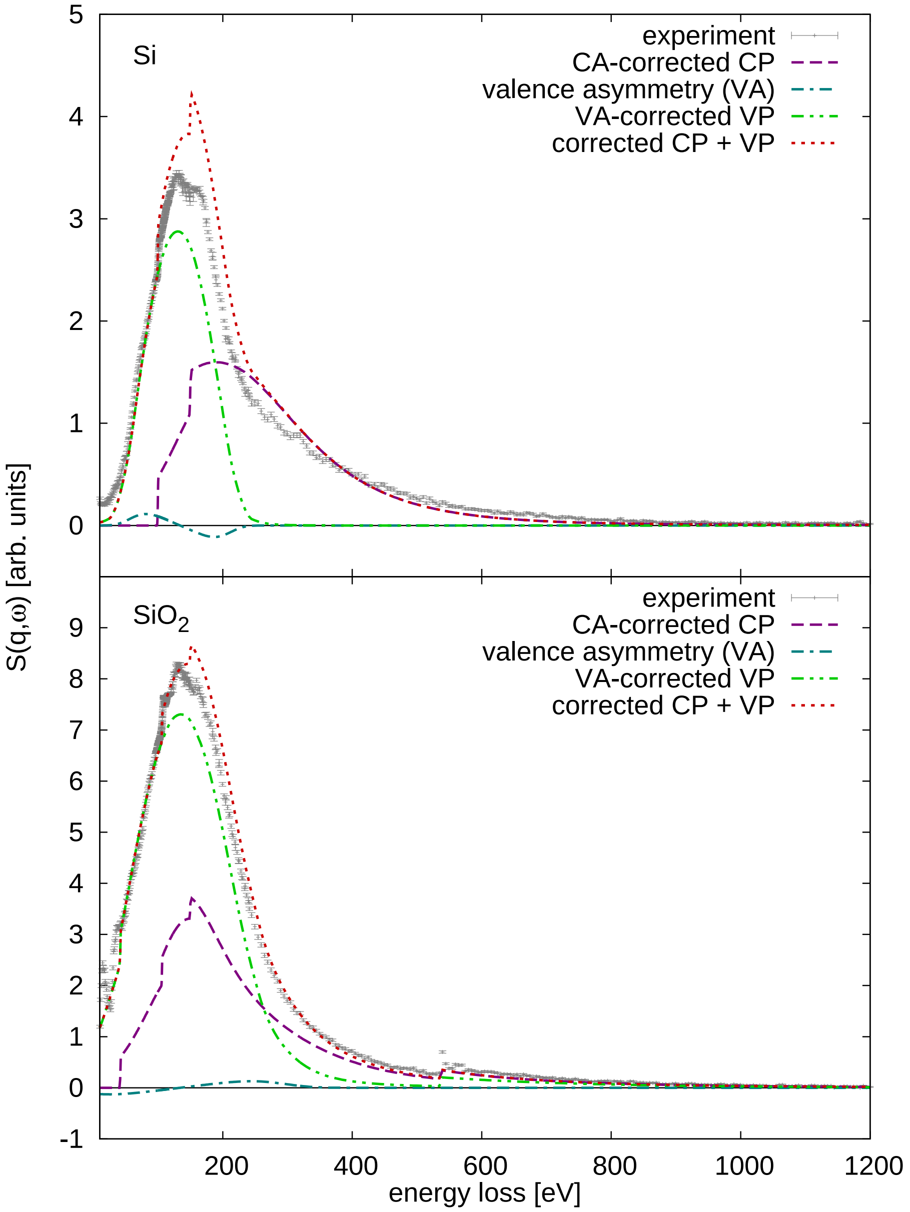

Figure 4.5: Extraction of the silicon L–edges in Si (top) and SiO$_2$ (bottom) for $q = 3.15$ a.u. by subtraction of the valence asymmetry (VA) corrected symmetrized valence profile (VP).

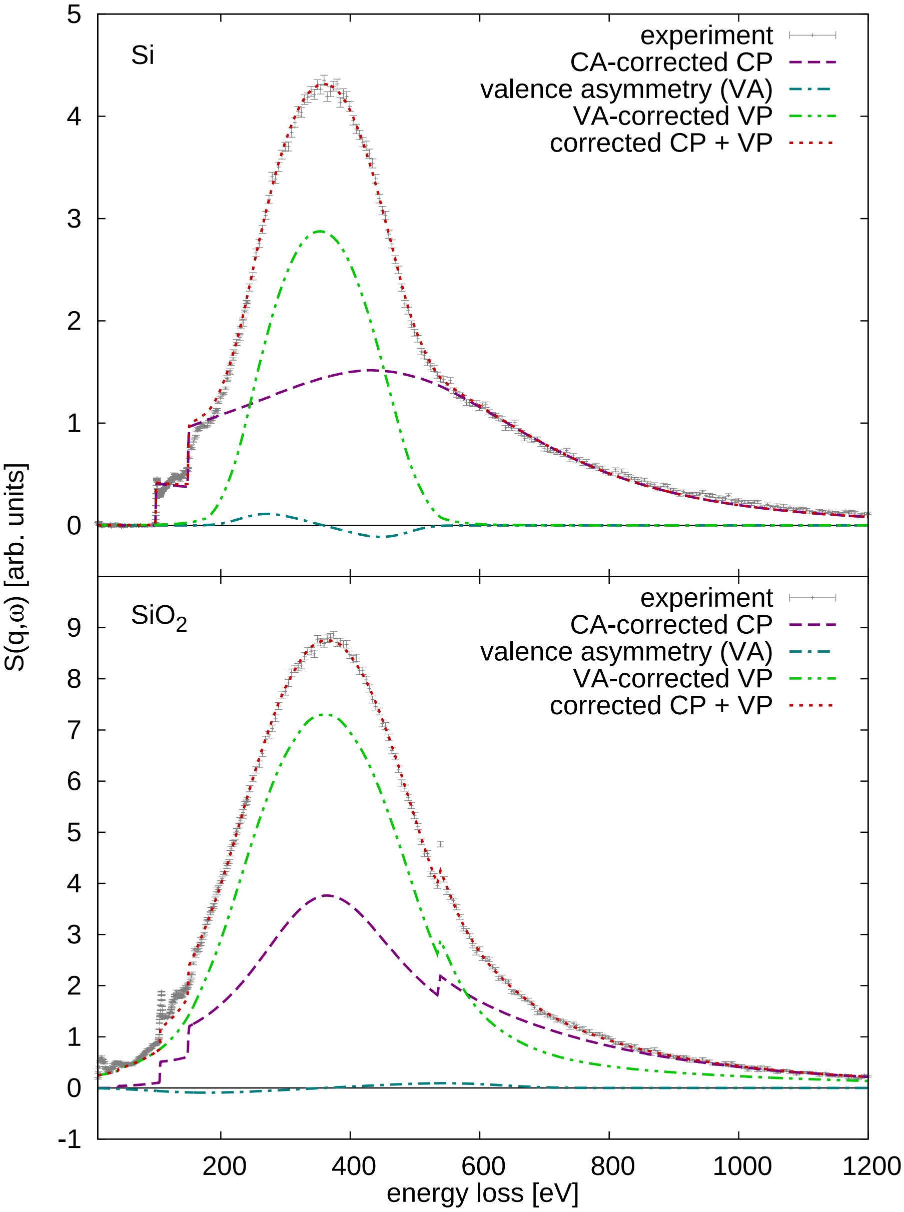

Figure 4.6: Extraction of the silicon L–edges in Si (top) and SiO_2 (bottom) for $q = 5.10$ a.u.

4.2.3 Extraction of the silicon $L_{II,III}$–edges

In the following, the extraction of the absorption edges of interest from the total signal will be discussed separately for high and intermediate momentum transfers and for low momentum transfers. Finally, the quality of the resulting spectra will be reviewed.

Intermediate and high momentum transfers

With the asymmetry–corrected symmetrized valence Compton profile the absorption edges can be distilled from the underlying background signal. In general, also the core–electron background can be subtracted as will be demonstrated later for SiO_2. The top parts of Figs. 4.5 and 4.6 show two examples for the extraction of the silicon L–edges in Si for an intermediate and a high momentum transfer respectively. The spectra are selected to show both the performance and the limitations of the presented algorithm. For intermediate momentum transfer, the sum of the corrected Hartree–Fock core profiles and the experimentally extracted valence profiles show adequate qualitative and quantitative agreement with the shape of the experimental spectrum on the full energy scale while it is nearly perfect for high momentum transfer. This is due to the fact that for intermediate and low q the impulse approximation is not valid and the approximations used in this approach are not fulfilled. It can be seen in Fig. 4.5 that the core asymmetry correction by Holm cannot give a proper description for the near–edge region of the silicon $L_{II,III}$–edges in Si. However, a treatment without the asymmetries does not yield better results. These deviations are not obvious in the case of SiO_2, in which the oxygen L_I–edge contribution dominates the spectrum. In this procedure, the constant scattering background value is refined to achieve the best agreement with the experiment. The silicon L–shell electron contributions can then be obtained by subtracting the corrected valence contributions from the spectra. Likewise, the extraction can be performed for the different momentum transfers. For other materials, the background may contain contributions from further core levels. They can, in general, be subtracted by the according corrected Hartree–Fock profiles. The comparison of the corrected sum of valence and core contributions with the experiment exhibits a measure for the quality of the NRIXS extraction. This is strongly depending on the relative position of the edge onset to the Compton spectrum. For the spectra above $q = 3.7\,\text{a.u.}$, the onset of the silicon $L_{II,III}$–edges (≈ 100 eV) is sufficiently far away from the Compton maximum. Therefore, only the spectral weight of the full profile is affected by the background refinement and the quality of the valence profile, whereas the near–edge structure shows only low sensitivity. For intermediate q ($2.4\,\text{a.u.} < q < 3.2\,\text{a.u.}$), the edge onset is very close to the maximum of the valence contribution. Especially the near–edge regime of the silicon $L_{II,III}$–edges is rather sensitive to the shape of the valence profile and the parameterization of its asymmetry concerning the fine structure and to the core electron Compton profile concerning spectral weight. For $q < 2.4\,\text{a.u.}$, the subtraction of a Pearson function yields better results than the valence subtraction as will be discussed in the next paragraph. For SiO_2 (lower parts of Figs. 4.5 and 4.6), the overall agreement between the total sum of the corrected Compton profiles with the experiment is of good quality. However, in Fig. 4.5, the experimental spectrum shows modulations close to the onset of the silicon $L_{II,III}$–edges. They can be attributed to EXAFS–like oscillations in the vicinity of the oxygen L_I–edge at 41.6 eV, which cannot be removed by the subtraction of the valence electron contribution. Thus, the error of the extracted NRIXS spectra is systematically and inherently increased close to the edge onset. Though beyond the scope of this work, an approach to compensate such oscillations could be a theoretical computation of the EXAFS spectrum, for instance employing the ab–initio FEFF code.[19] The valence profile and its asymmetry correction is very broad for SiO_2 since it includes the oxygen 2p electrons. Hence, the NRIXS extraction is critical because the edge onset lies close to the Compton maximum for a wider q–range ($2.4\,\text{a.u.} < q < 3.8\,\text{a.u.}$) than for Si. For the spectra with the edge onset closest to the maximum of $S(\mathbf{q},\omega)$ ($2.4\,\text{a.u.} < q < 2.8\,\text{a.u.}$), a proper subtraction of the valence–electron contribution was not possible. A subtraction of a Pearson function is also inadequate close to the Compton maximum, so that the two spectra in this regime were excluded from analysis. Above $q = 4.2\,\text{a.u.}$, the extraction is very robust again.

Small momentum transfers

For momentum transfers below 2.4 a.u., the modeled Compton profile can only poorly approximate the particle–hole excitations/plasmon spectrum. The slowly decreasing high energy loss tail of these contributions, which is strongly influenced by electron–electron correlation and bandstructure effects,[20] cannot be modeled by simple theoretical ab–initio approaches within the scope of an extraction scheme as presented in this work. Hence, the extraction of the silicon L–edges is performed by fitting a parameterized function to the region before the edge onset as shown in Fig. 4.7. A Pearson–VII function[21] was found to be a good representation for the slowly decreasing tail of the excitation spectrum for low q:[22]

$$P(\omega) = \beta_1 \left(\beta_3^2 (\omega - \beta_2)^2 + 1\right)^{-\beta_4} . \tag{4.9}$$

Whereas the near–edge region is hardly affected by the slope of the background function, uncertainties for the absolute intensity of the extracted edges grow especially for high

---

[19] A.L. Ankudinov *et al.* (1998*a*), *Phys. Rev. B* **58**, 7565; J.A. Soininen *et al.* (2005), *Phys. Rev. B* **72**, 045136.

[20] C. Sternemann *et al.* (2005*b*), *Phys. Rev. Lett.* **95**, 157401.

[21] H. Wang and J. Zhou (2005), *J. Appl. Cryst.* **38**, 830.

[22] β_n are fitting parameters.

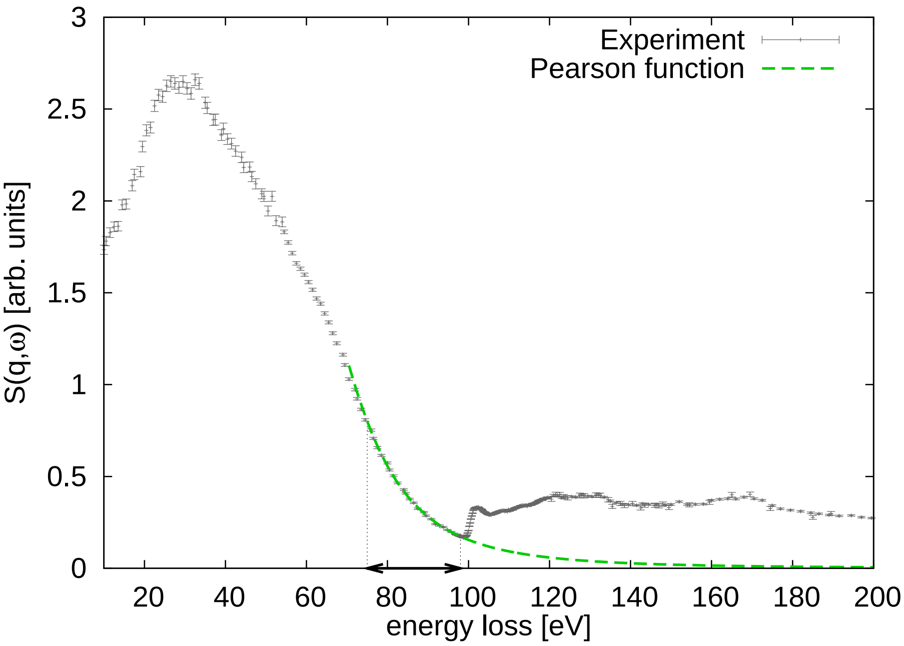

Figure 4.7: Extraction of silicon L–edges in Si for $q = 1.66\,\text{a.u.}$ by subtraction of a Pearson function. The fitting range is indicated by an arrow on the abscissa.

curvatures in the background function.

Local–field correction

An alternative approach for the background subtraction would be the modification of the experimentally extracted valence Compton profile with the phenomenological local–field correction (LFC) factor $G(q)$ in the dielectric function[23]

$$\epsilon(\mathbf{q},\omega) = 1 + \frac{\epsilon_{\text{sym}}(\mathbf{q},\omega) - 1}{1 - G(q)(\epsilon_{\text{sym}}(\mathbf{q},\omega) - 1)}. \tag{4.10}$$

The complex function $\epsilon_{\text{sym}}(\mathbf{q},\omega)$ can be calculated from the valence profile employing the relation $S(\mathbf{q},\omega) = \Im(-1/\epsilon(\mathbf{q},\omega))$ and a Kramers–Kronig transformation. The LFC factor introduces an additional asymmetry into the valence profile to model the typically increasing skewness of $S(\mathbf{q},\omega)$ for lower momentum transfer in a phenomenological way. An example for the effect of $G(q)$ is given in Fig. 4.8. Nonetheless, for the low–q extraction of the spectra presented in this work, the Pearson method yields the better results and is therefore applied.

---

[23] J. Hubbard (1957), *Proc.R. Soc. London Ser. A* **240**, 539.

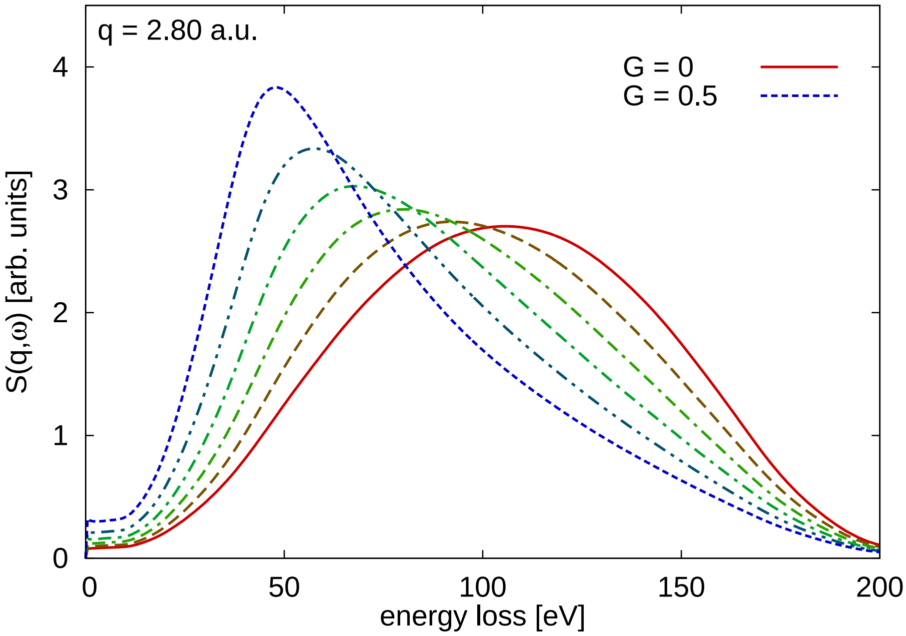

Figure 4.8: Phenomenological modification of $S(\mathbf{q},\omega)$ according to the local–field correction. $S(\mathbf{q},\omega)$ is shown for $G(q) = 0, 0.1, \ldots 0.5$.

Result

For Si, the extraction of the silicon L–edges can be performed as described in the two preceding sections for 16 different momentum transfers. For $q = 2.41$ a.u., the maximum of $S(\mathbf{q},\omega)$ is decorated by a fine structure. Therefore the extracted valence Compton profile only shows poor agreement in the energy region before the edge onset and the spectrum was taken out of the analysis. The resulting spectra are shown in the top part of Fig. 4.9 and evolve consistently for increasing momentum transfer. q–dependent NRIXS calculations of the silicon L–edges have been performed employing the adaptation[24] of the real space multiple scattering code FEFF[25] presented in chapter 2.2. The results are shown in the bottom part of Fig. 4.9 and exhibit very good qualitative and quantitative agreement with the experimental spectra over the full energy range. As discussed elsewhere[26] the interaction of the photo–electron with the core hole is important to explain the structure of the near–edge region whereas its neglect yields better agreement in energetic positions for higher energy losses. So, calculations for the full range without a core–hole interaction have been performed, whereas the core hole was taken into account for the near–edge region presented in the inset of Fig. 4.9. The broadening of the edge onset in the calculations and the absence of the peaked white line around 102 eV energy loss can be attributed

---

[24] J.A. Soininen *et al.* (2005), *Phys. Rev. B* **72**, 045136.

[25] A.L. Ankudinov *et al.* (1998*a*), *Phys. Rev. B* **58**, 7565.

[26] H. Sternemann *et al.* (2007*a*), *Phys. Rev. B* **75**, 075118. See also chapters 5.3.2 & 5.3.3.

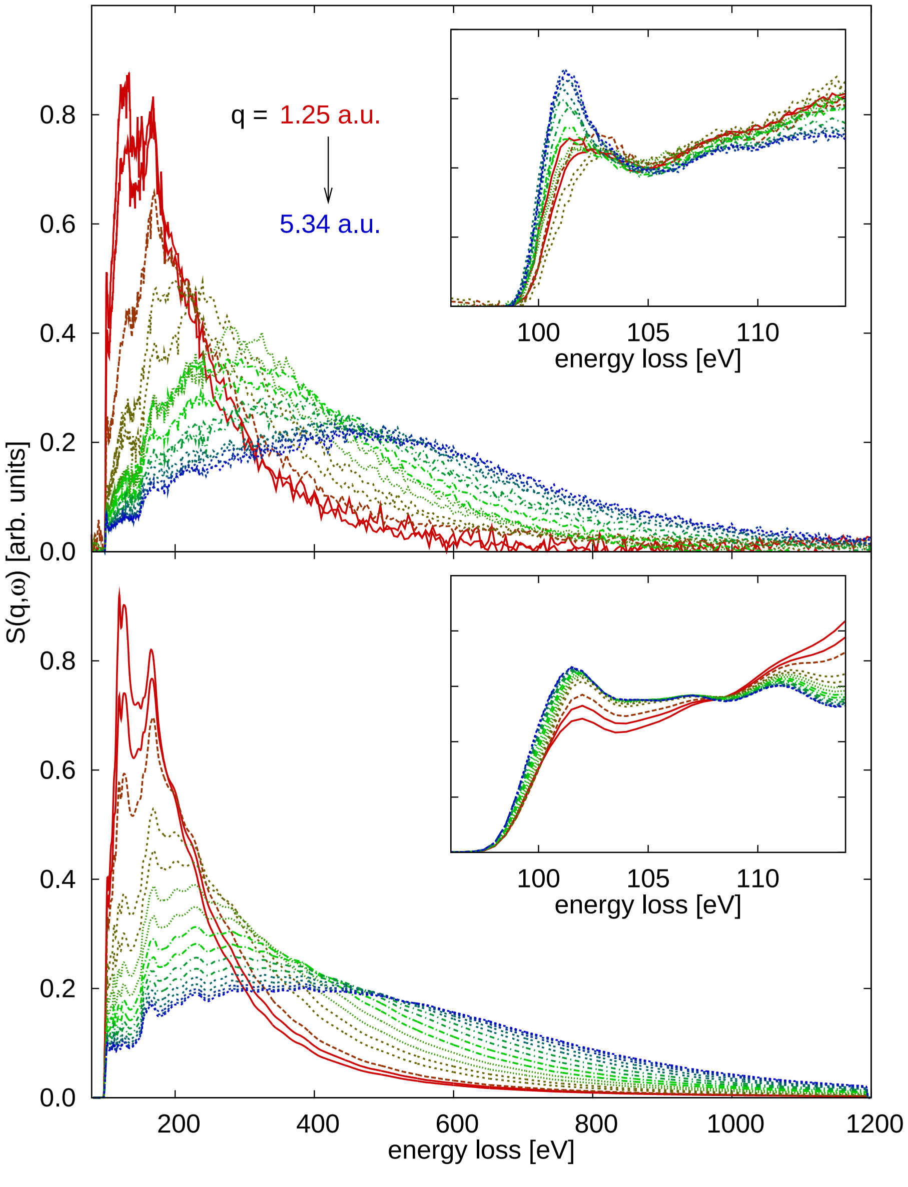

Figure 4.9: Top: Extracted silicon L–edges of Si for different q. The spectra are normalized to the full area. The inset shows the near–edge region of the silicon $L_{II,III}$–edges normalized to the area between 95 and 110 eV. Bottom: RSMS calculations of the silicon L–edges in Si for the same q and with the same normalization. The wide spectra have been calculated neglecting the core hole–electron interaction while it has been accounted for in the near–edge calculations presented in the inset.

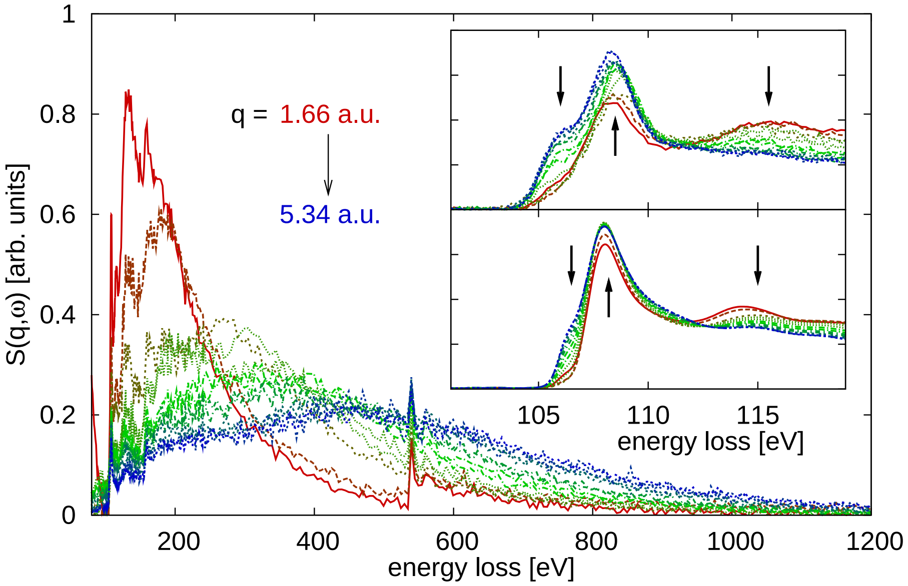

Figure 4.10: Extracted silicon L–edges and oxygen K–edge of SiO_2 for different q. The near–edge region in the top part of the inset is normalized to the area between 100 and 120 eV and the pre–edge region is shifted to zero to compensate for the offset due to the oxygen L_I–edge. The bottom part of the inset shows q–dependent calculations of the silicon $L_{II,III}$–edges employing an ab–initio NRIXS approach based on the StoBe–deMon code. Corresponding features of experiment and theory are indicated by arrows.

to approximations used in the RSMS computation as discussed for Si by Sternemann *et al.*[27] For SiO_2, the extraction is good for 14 momentum transfers. The results are shown in Fig. 4.10. The modulations of the oxygen L_I–edge at 41.6 eV lead to systematic errors in the silicon $L_{II,III}$–edges. This results in a q–dependent contribution of the NRIXS spectrum below the energy onset, whereas it should be zero for perfect subtraction as it is the case for Si. The correction of these effects is not possible within the algorithm presented in this article but would require a theoretical treatment of the oxygen L_I–edge fine structure. However, the extracted NRIXS spectra show a consistent q–dependence on the whole energy scale. Since the oxygen L_I–edge oscillations are assumed to be smooth very close to the absorption edge, they can be approximated by a constant offset. The inset of Fig. 4.10 shows the very near–edge region of the silicon $L_{II,III}$–edges normalized to its area. The consistency of the q–dependence can also clearly be seen here. Momentum–transfer dependent calculations of the silicon $L_{II,III}$–edges have been performed employing a density–functional theory ab–initio NRIXS approach based on the StoBe–deMon code.[28] Spectra for the 14 momentum transfers were calculated for an α–quartz SiO_2 cluster of

---

[27] H. Sternemann *et al.* (2007*a*), *Phys. Rev. B* **75**, 075118. See also chapter 5.3.1.

[28] See chapter 2.4 and A. Sakko *et al.* (2007), *Phys. Rev. B* **76**, 205115.

72 atoms.[29] The results presented in the bottom part of the inset of Fig. 4.10 show very good agreement with the experiment concerning the overall shape and especially the q–dependence of the features indicated by the arrows.

4.3 Conclusions and outlook

In this chapter, an algorithm for the subtraction of the Compton– and $S(\mathbf{q},\omega)$–background from NRIXS spectra was presented and shown to be applicable for a broad q–range. The algorithm is universal in a sense that apart from atomic Hartree–Fock core Compton profiles no sample–dependent calculations are necessary to model the background. The valence contribution to the Compton profile can directly be extracted from the experiment and used for the extraction of the edges of interest. As a proof of principle, the algorithm was applied to the silicon L–edges in Si and SiO_2, in which the extraction proved to be very successful for most of the momentum transfers. The robustness and difficulties for the extraction were discussed in detail for the different momentum–transfer ranges. A comparison of q–dependent NRIXS calculations for Si and SiO_2 show the good quality of the extraction both concerning overall shape and q–dependence. Based on this study, the presented algorithm yields a tool for the proper treatment of multi–q NRIXS spectra. This is the prerequisite for the studies presented later in this work but it is also of special importance for, e.g., future studies demanding a detailed study of the q–dependence of core excitation or an extraction of the projected density of states.

---

[29] The DFT calculations were performed by A. Sakko, Department of Physical Sciences, University of Helsinki. The linewidth for Lorentzian broadening was 0.1 eV below 107 eV and 2.5 eV above 110 eV with a linear increase between 107 and 110 eV energy loss. The Gaussian linewidth was 0.8 eV.

Chapter 5

Study of L–shell excitations by NRIXS: different computational approaches

Non–resonant inelastic x–ray scattering from s atomic core levels has become a well established method to study the near–edge structure of shallow absorption edges.[1] Incident x–ray energies of about 10 keV are used to measure K absorption edges ranging from lithium (54.7 eV) to fluorine (696.7 eV). As the atomic number Z increases, the energy of the K–edge becomes too high for NRIXS measurements with current experimental methods. Therefore, it is important to extent such studies to cover elements with medium or high Z by the measurement of their L–, M– and N–edges.[2] For a deeper understanding of the electronic structure studied by NRIXS, comparisons with theoretical approaches are needed. Most recently, the far–edge structure has been discussed in detail by Fister *et al.*[3] using the RSMS approach based on FEFF.[4] In this regime, the EXAFS–like fine structure of the absorption edges basically contain information on the local atomic structure and the calculations show very good agreement with the experiment. Close to the edge onset, electronic effects are significantly more important and a proper description by theory is not straightforward.

In this chapter, a detailed study of the L near–edge structure for the metals sodium and magnesium and for the semiconductor silicon is presented based on a comparison with two different computational formalisms. First–principles calculations performed with the RSMS approach and the BSE formalism[5] will be compared with each other and experi-

---

[1] U. Bergmann *et al.* (2002), *Microchem. J.* **71**, 221; Y. Feng *et al.* (2004), *Phys. Rev. B* **69**, 125402; K. Hämäläinen *et al.* (2002), *Phys. Rev. B* **65**, 155111; M. Krisch and F. Sette (2002), *Surf. Rev. Lett.* **9**, 969; A. Mattila *et al.* (2005), *Phys. Rev. Lett.* **94**, 247003; Ph. Wernet *et al.* (2004), *Science* **304**, 995.

[2] C. Sternemann *et al.* (2005*a*), *Phys. Rev. B* **72**, 035104.

[3] T.T. Fister *et al.* (2006*a*), *Phys. Rev. B* **74**, 214117.

[4] See chapter 2.2 and J.A. Soininen *et al.* (2005), *Phys. Rev. B* **72**, 045136.

[5] See chapter 2.1 or J.A. Soininen (2001), “Final–state interactions in inelastic x–ray scattering”, PhD thesis, University of Helsinki; J.A. Soininen and E.L. Shirley (2001), *Phys. Rev. B* **64**, 165112; J.A. Soininen *et al.* (2001), *J. Phys.: Condens. Matter* **13**, 8039; J.A. Soininen *et al.* (2005), *Phys. Rev. B* **72**, 045136.

ments. Especially the q–dependence is used to study the performance of different computational approaches to simulate NRIXS spectra. This provides a more stringent test since, in principle, it gives more insight into how the approaches work for different components of the l–DOS for the same core–hole state. The role of screening and the dependence of the spectra on the momentum transfer will be emphasized. These questions have not been studied so far for NRIXS L–edges but they play an important role for evaluating the multiple–scattering approach.[6] This is fundamental for the study of the near–edge structure of medium–Z elements in general.

In the following two sections, details will be given on the RSMS calculations and the experiment. The comparison between experiment and computed spectra for the three elements will be discussed in chapter 5.3. A conclusion is given at the end.

5.1 Computational details

In the experiments presented in this part, the focus is set on the near–edge region, i.e. the first 50 eV above the edge onset, where multiple–scattering processes predominate. Therefore, the spectra shown in this chapter have been calculated regarding multiple scattering to an infinite order for a finite cluster of atoms. Typical cluster sizes of 300 atoms have been used in the calculations. The potential is calculated self–consistently within clusters of 70 to 100 atoms. Moreover, close to the edge onset, the interaction of the electron with the core hole as well as the electron's self–energy become important. Calculations have been performed, both considering a core hole and for the case of complete screening. As discussed in chapter 2.2.3, the FEFF8.2 code allows different treatments of the self–energy. Here, the Hedin–Lundqvist approximation[7] has been used in all calculations except for sodium. The case of sodium will be discussed in detail in 5.3.3. All results are orientationally averaged corresponding to polycrystalline and powder samples.[8] Spectra for the L_{I}– and the $L_{II,III}$–edges have been calculated separately and were weighted with the multiplicity of the initial state. Since absolute edge positions are usually estimated with an error of some eV,[9] the calculations have been shifted to match the edge onsets of the measured spectra. Finally, the calculations were convoluted with the according experimental energy resolution. The BSE approach yields a more realistic model for the electronic structure and two–particle interactions of the system. However, it assumes periodic boundary conditions so that studying non–periodic systems is unfeasible. Moreover, it does not include

---

[6] A.L. Ankudinov *et al.* (1998*a*), *Phys. Rev. B* **58**, 7565; J.A. Soininen *et al.* (2005), *Phys. Rev. B* **72**, 045136.

[7] U. von Barth and L. Hedin (1972), *J. Phys. C: Solid State Phys.* **5**, 1629.

[8] For the RSMS approach, the directional averaging is algebraically embedded in the code whereas for the BSE approach, calculations were performed for different orientations of the q–vector and then averaged.

[9] See, e.g., A.L. Ankudinov *et al.* (1998*b*), *Phys. Rev. B* **57**, 7518.

dynamical core–hole effects and can only address the near–edge region.[10]

5.2 Experimental details

The experiments were performed at the inelastic x–ray scattering beamline ID16 at ESRF. The magnesium sample was a polycrystalline metal disc of 99.9% purity (Goodfellow). The silicon powder sample of 99.999% purity with a particle size less than 44 μm (MaTecK) was pressed to a pellet of about 0.5 mm thickness. Both samples were kept under vacuum (1 mbar) during the experiment. The polycrystalline sodium sample of about 10 mm thickness was prepared under argon atmosphere and kept in a sample holder under high vacuum conditions (10^{-6} mbar) during that experiment in order to avoid hydroxide formation. Spectra for magnesium, sodium and silicon have been recorded for two different momentum transfers each.[11] The raw NRIXS data was normalized to a monitor signal and corrected for a constant background, absorption and scattering cross section as described in chapter 4. For low momentum transfers, the plasmon contribution to the scattering signal was subtracted by fitting a Pearson–VII function[12] to the plasmon tail close to the absorption edge. The ratio between the signal of the plasmon tail and the absorption edge was found to be 1:1 for silicon, 1:3 for magnesium and 1:6 for sodium at the edge onset. As discussed in chapter 4.2, for high momentum transfers, the contribution of the valence electron Compton profile has to be accounted for in the EXAFS energy regime. However, for the small energy range close to the edge, as discussed in this chapter, such a contribution is found to be negligible and thus requires no further correction. The resulting experimental NRIXS spectra are presented in Figs. 5.1, 5.3, and 5.5 together with the corresponding calculations using the BSE approach and the RSMS implementation for NRIXS.

5.3 Results and discussion

Calculations for all NRIXS spectra have been performed with the q–dependent RSMS code as well as with the BSE approach. In the following, the results are presented and discussed in detail for each sample. The particularities of semiconductor calculations are emphasized for silicon with the focus on the projected density of states. In the case of magnesium, the core–hole effect is discussed and decompositions of the calculations with respect to the angular momentum of the final state are shown as an example. Different treatments of screening within the RSMS approach are compared for sodium.

---

[10] All BSE calculations have been performed by J.A. Soininen. For more details of the computational method, see J.A. Soininen *et al.* (2001), *J. Phys.: Condens. Matter* **13**, 8039.

[11] The experimental parameters are given in table A.2 (key A_n).

[12] See chapter 4.2 or H. Wang and J. Zhou (2005), *J. Appl. Cryst.* **38**, 830.

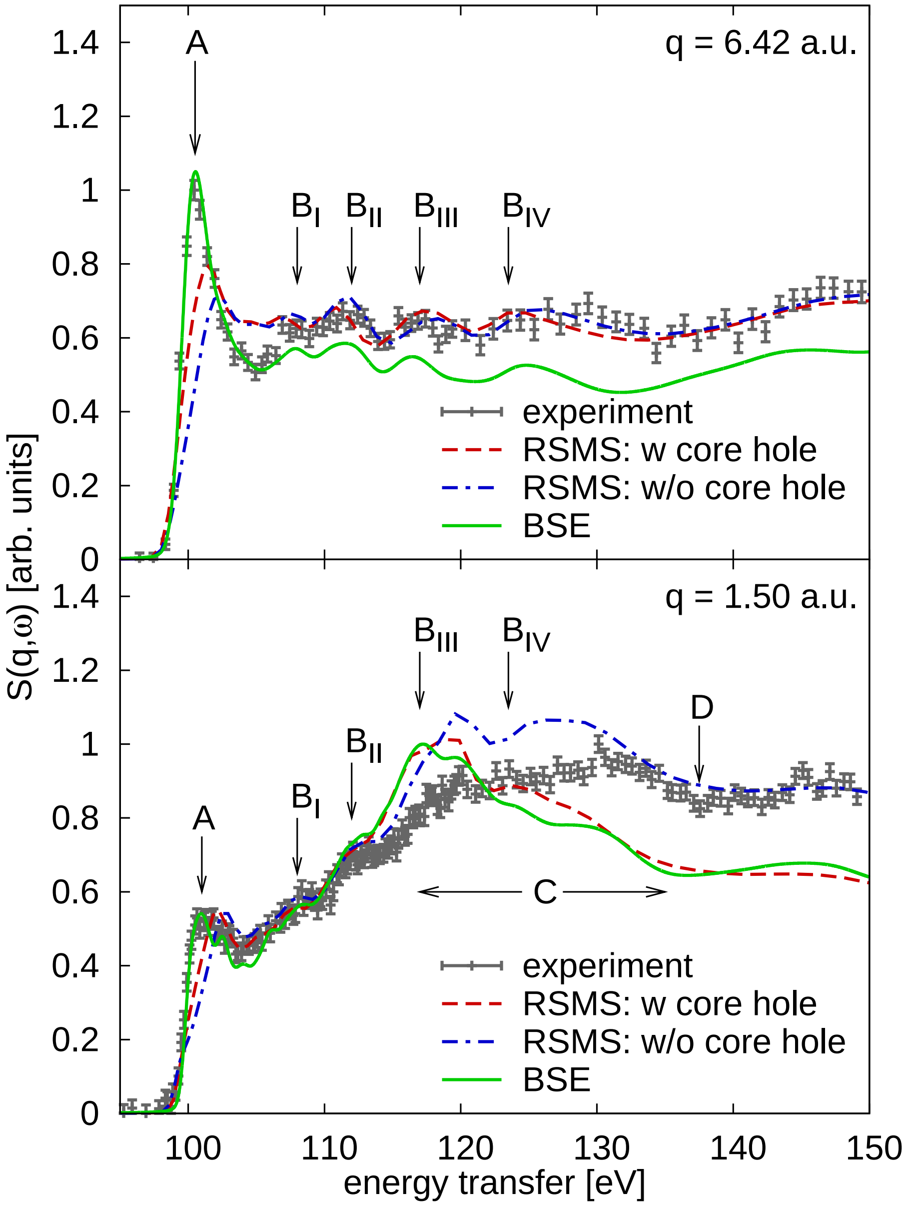

Figure 5.1: NRIXS spectra of the silicon $L_{II,III}$–edges at $q = 1.50$ a.u. (bottom) and $q = 6.42$ a.u. (top). RSMS calculations are shown with and without core–hole interaction. The result of the BSE calculations is shown for comparison.

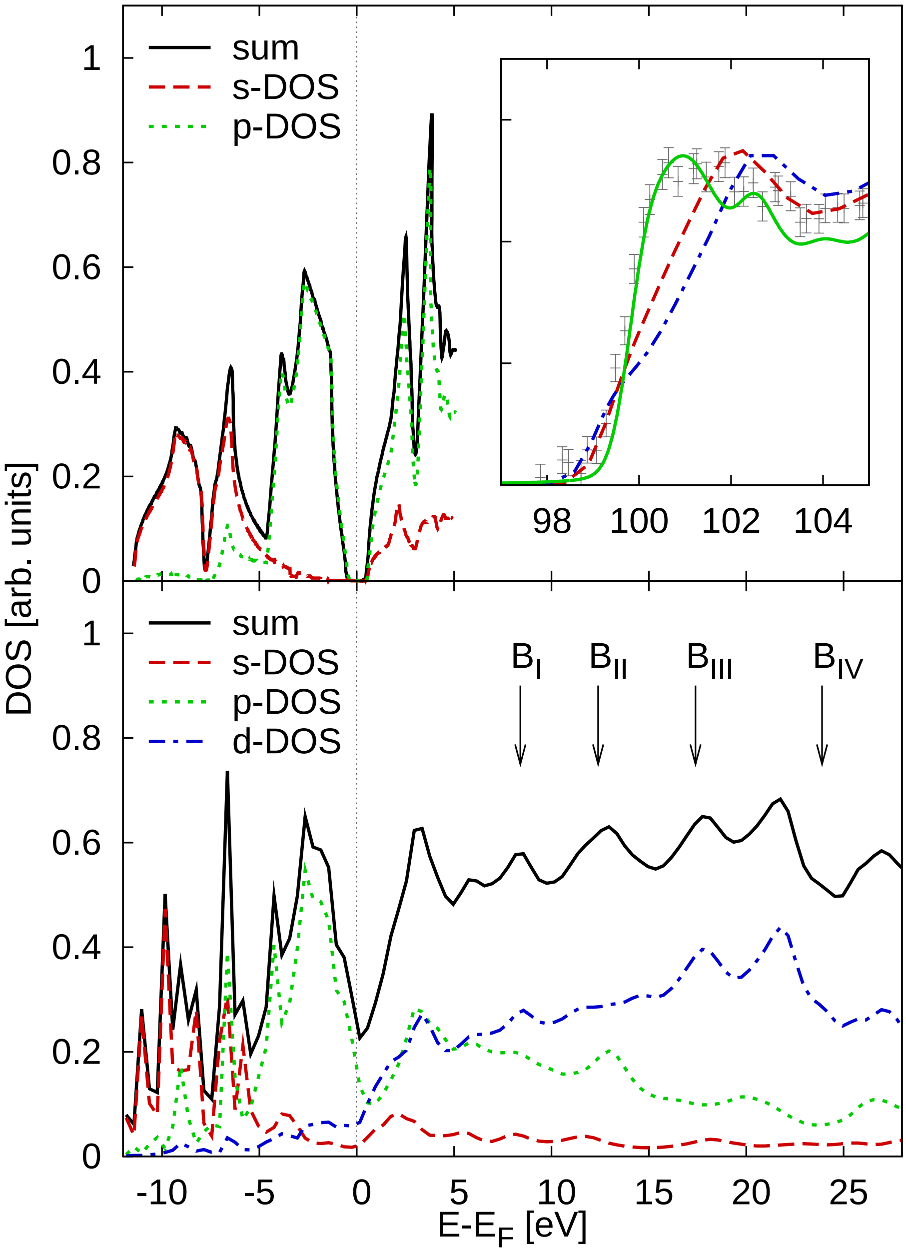

Figure 5.2: l–DOS of silicon: Calculation with RSMS assuming full screening of the core hole (bottom) and SK–LCAO parameterized DFT ground–state calculation by Papaconstantopoulos (top). The inset shows a magnification of the silicon $L_{II,III}$–edge onset at $q = 1.50$ a.u. from Fig. 5.1.

5.3.1 Silicon

Due to the general importance of silicon in material science, the near–edge structure of the silicon L–edges has been studied extensively in the past.[13] Especially, the effect of the core hole to the edge onset was discussed controversially.[14] By comparing the full potential linearized augmented plane wave calculations with the x–ray absorption spectra, Buczko *et al.*[15] emphasize the importance of the core–hole treatment to properly describe the very near–edge structure. In contrast, Weng *et al.*[16] conclude that the edge onset can be described well without consideration of the core hole. These studies were limited to energy ranges up to 5 eV above the edge. A recent comparison of the silicon $L_{II,III}$–edge with BSE calculations supports the results of Buczko *et al.*[17] Within this work, measurements of the silicon $L_{II,III}$–edges up to 50 eV above the edge onset are presented emphasizing the particularities of RSMS calculations.

The results of the calculations for silicon are shown in Fig. 5.1 for $q = 6.42$ a.u. and $q = 1.50$ a.u. The overall agreement with the experiment is good for all calculations. The shape of the edge onset is well reproduced by the BSE calculations whereas the peak at the edge (the so–called white line, indicated by A) is significantly underestimated for high momentum transfer using the RSMS method. Besides the edge onset, the multiple–scattering calculations match the experiment very well for both momentum transfers. The fine structures $\mathsf{B_n}$ are qualitatively reproduced whereas their position is found more accurately by neglecting the core–hole interaction. In the case of low q, this is also true concerning the width of the broad feature C between 120 and 135 eV and for the position of D. Yet, the amplitude of feature C is overestimated in the calculation without the core hole. However, despite these quantitative discrepancies, the experimental fine structure can obviously be related to features predicted by theory (see, e.g., $\mathsf{B_n}$ in Fig. 5.1 and 5.2).

Concerning the shape of the edge onset the RSMS calculations show shoulders in the first two eV of the edge onset and a flattened–out white line for both momentum transfers as can be seen for low q in the inset of Fig. 5.2. This can be explained in view of the l–DOS, which was calculated with the RSMS code and is shown in the bottom part of Fig. 5.2. It is also known from other calculations[18] within the local–density approximation (LDA) that the bandgap of semiconductors is usually underestimated. Instead of 1.1 eV for

---

[13] See, e.g., P.E. Batson (1993), *Phys. Rev. B* **47**, 6898; R. Buczko *et al.* (2000), *Phys. Rev. Lett.* **85**, 2168; J.R. Dahn *et al.* (1994), *J. Appl. Phys.* **75**, 1946; H. Ma *et al.* (1990), *J. Appl. Phys.* **68**, 288; X. Weng *et al.* (1989), *Phys. Rev. B* **40**, 5694; X. Weng *et al.* (1990), *Solid State Comm.* **74**, 1013.

[14] R. Buczko *et al.* (2000), *Phys. Rev. Lett.* **85**, 2168; X. Weng *et al.* (1990), *Solid State Comm.* **74**, 1013.

[15] R. Buczko *et al.* (2000), *Phys. Rev. Lett.* **85**, 2168.

[16] X. Weng *et al.* (1990), *Solid State Comm.* **74**, 1013.

[17] C. Sternemann *et al.* (2005*a*), *Phys. Rev. B* **72**, 035104.

[18] R.W. Godby *et al.* (1988), *Phys. Rev. B* **37**, 10159; J.P. Perdew and M. Levy (1983), *Phys. Rev. Lett.* **51**, 1884; L.J. Sham and M. Schlüter (1983), *Phys. Rev. Lett.* **51**, 1888.

silicon, only about 0.6–0.7 eV is found computationally.[19] Moreover, the spectra are also broadened due to the finite cluster size in the RSMS calculations. Papaconstantopoulos[20] has calculated the DOS for silicon with a LCAO[21] parameterized DFT using the Slater–Koster (SK) method[22] (see the top part of Fig. 5.2). While these results show a bandgap of 1.1 eV with a sharp onset of the conduction band, no band gap is obtained in the l–DOS of the calculations presented here. It shows only a smooth minimum at the Fermi energy E_{F}. Thus, unoccupied states contribute to the NRIXS spectra where the gap is expected and the edge onsets in the spectra are smeared out. A part of this discrepancy could also be due to the approximate treatment of electron–hole interactions used in the RSMS. Typically, the region close to the edge is most sensitive to the details of the approximations used to model the electron–hole interactions.

The RSMS calculations including the core hole yield a better description of the edge onset, which is in line with the results of Buczko *et al.*[23] emphasizing the importance of core–hole effects. Nevertheless, only the BSE method is able to satisfactorily reproduce the edge onset. This can be attributed to the deficiency of the RSMS calculations failing to account for the proper bandgap. However, in the energy regime around 10 to 40 eV above the edge, the agreement between calculation and experiment with respect to energy positions of distinct spectral features is good but it can be improved by neglecting the core hole. This effect will now be discussed in more detail for the case of magnesium.

5.3.2 Magnesium

Spectra of the magnesium $\mathrm{L}_{\mathrm{II,III}}$–edges for momentum transfers of 0.61 a.u. and 6.42 a.u. are shown in Fig. 5.3. Recently, experimental data of the q–dependence of magnesium NRIXS spectra of for eight momentum transfers between 0.42 a.u. and 5.34 a.u. have been published by Fister *et al.*[24] The experimental results of that work are in good agreement with the results presented here when compared to the corresponding momentum transfer. The RSMS calculations have been performed, both including the core–hole effect and for full screening. For low q, the two calculations show good overall agreement with the experiment. The near–edge fine structure A is well reproduced, whereas the maximum B and the minimum C in the calculation including the core hole are shifted when compared to the experiment. These shifts are of the order of 1–2 eV towards lower energy losses and

---

[19] W.G. Aulbur *et al.* (2000), "Solid State Physics", ed. by H. Ehrenreich and F. Spaepen, vol. 54, Academic, New York, 1.

[20] D. Papaconstantopoulos (1986), *Handbook of the Band Structures of Elemental Solids*, Plenum, New York.

[21] Linear Combination of Atomic Orbitals.

[22] J.C. Slater and G.F. Koster (1954), *Phys. Rev.* **94**, 1498.

[23] R. Buczko *et al.* (2000), *Phys. Rev. Lett.* **85**, 2168.

[24] T.T. Fister *et al.* (2006*a*), *Phys. Rev. B* **74**, 214117.

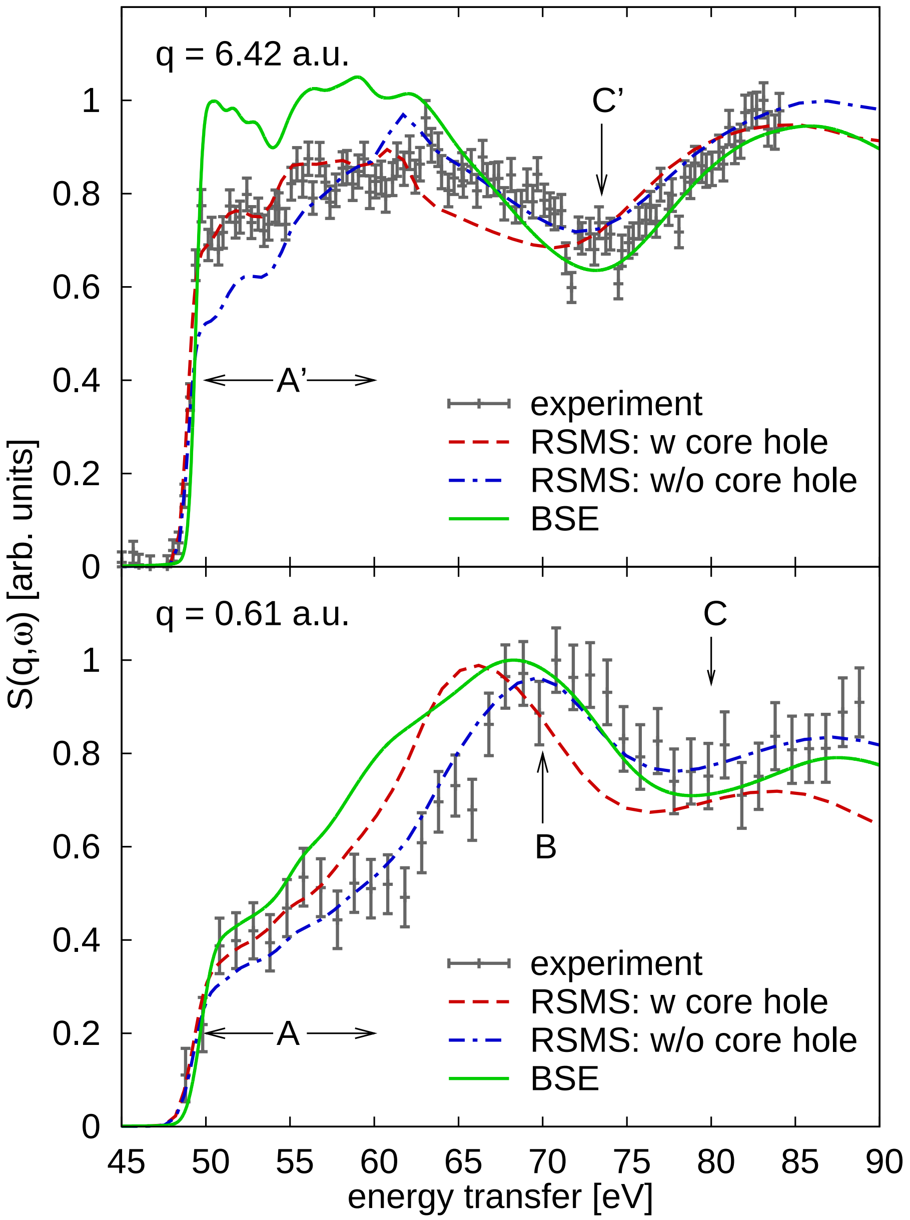

Figure 5.3: NRIXS spectra of the magnesium $L_{II,III}$–edges at $q = 0.61$ a.u. (bottom) and $q = 6.42$ a.u. (top). Calculations as in Fig. 5.1.

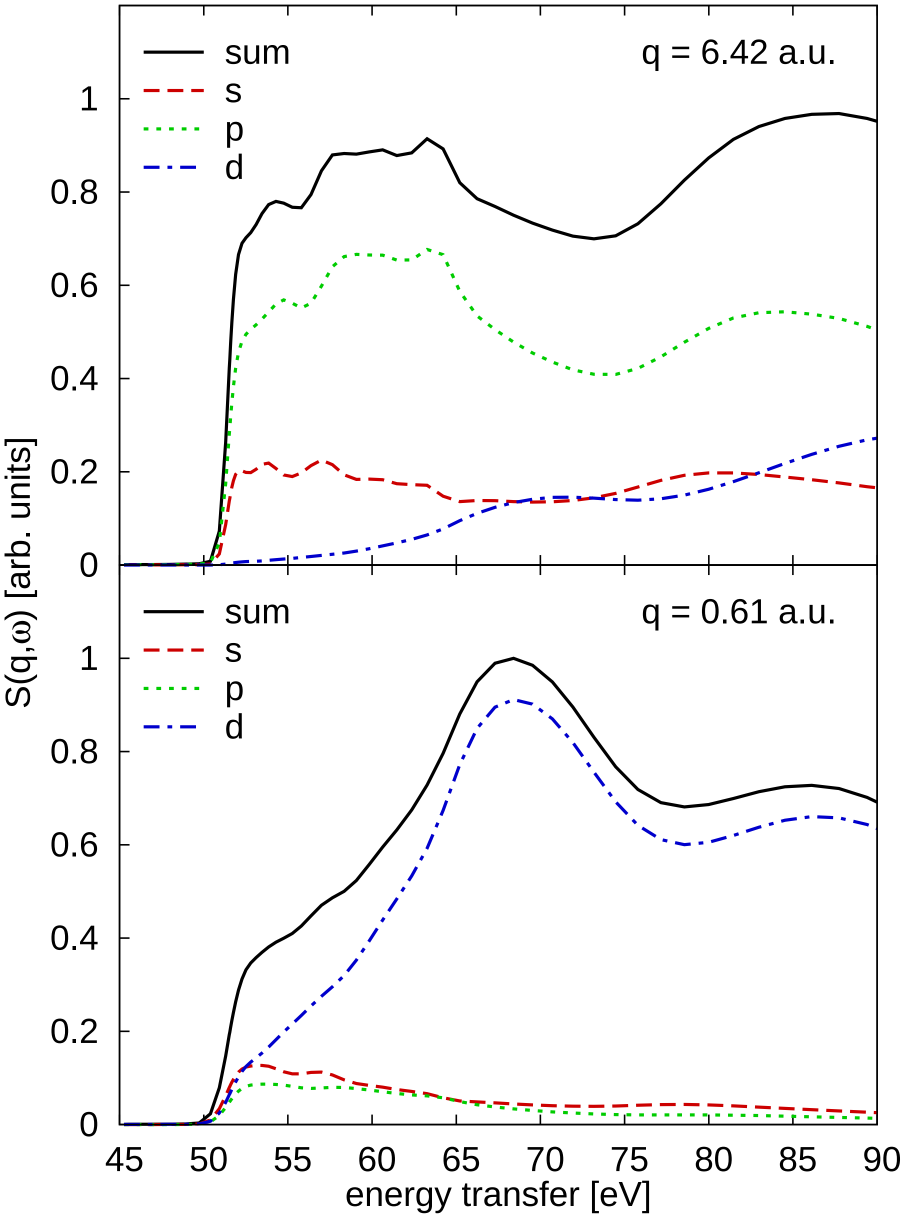

Figure 5.4: Decomposition of the RSMS calculations of the magnesium $L_{II,III}$–edges at $q = 0.61$ a.u. (bottom) and $q = 6.42$ a.u. (top) with respect to the angular momentum of the final state.

can also be observed for the case of silicon. Part of the reason for deviations in the energy positions between the experiment and RSMS computations could be the quasi–particle shift due to the real part of the self–energy when using the Hedin–Lundqvist approximation. Calculations of the copper K–edge in Rehr *et al.*[25] show similar shifts of the fine structures using a single plasmon–pole model in contrast to more sophisticated multi–pole calculations and experiments. This can also be observed for feature C′ in case of the high–q spectrum of magnesium in Fig. 5.3. Some eV above the edge, the positions of the designated features are better estimated ignoring the core hole. Especially for high q, the RSMS calculation including the core hole shows excellent agreement with the experiment for the pre–edge region A′. This regime in the spectrum is overestimated by the BSE result. Apart from that, the general shape and the fine structures are very well reproduced by the BSE. The treatment of the core hole is enhanced in this approach. Thus, it is plausible that the position of the experimental maximum at 70 eV energy loss is found more accurately than with the RSMS calculation including the core hole.

Theoretical decompositions concerning the angular momentum of the final state are shown in Fig. 5.4 for the RSMS calculations including the core hole. The dipole transition p → d dominates the spectrum for $q = 0.61$ a.u. corresponding to the expansion of the transition operator in Eqn. (2.5). By increasing the momentum transfer, the weight of the non–dipole contribution p → p increases significantly. The quadrupole transition p → f is calculated to be negligible and not shown in Fig. 5.4. Furthermore, it is apparent that also the shape of the decomposed contributions is modified for different q. So, for example, the weight of the two maxima in the d–projection for magnesium at $q = 0.61$ a.u. is reversed for $q = 6.42$ a.u. These changes are due to the momentum– and energy–transfer dependence of the matrix elements. Decompositions of the calculations for silicon and sodium are shown in appendix B.

5.3.3 Sodium

Many efforts have been made to study the onset of the sodium $\mathrm{L}_{\mathrm{II,III}}$–edges by means of the theory by Mahan, Nozières, and De Dominicis,[26] which is discussed extensively in literature.[27] The focus of these studies has naturally been to analyze the near edge only up to 3–4 eV above the onset. A study of the near–edge region up to 30 eV has been

---

[25] J.J. Rehr *et al.* (2006), arXiv:cond-mat/0601241, 2006. See also J.J. Kas *et al.* (2007), *Phys. Rev. B* **76**, 195116.

[26] G.D. Mahan (1967), *Phys. Rev.* **163**, 612; P. Nozières and C.D. De Dominicis (1969), *Phys. Rev.* **178**, 1097.

[27] M. Alouani *et al.* (1986), *Solid State Comm.* **60**, 657; P.A. Bruhwiler and S.E. Schnatterly (1990), *Phys. Rev. B* **41**, 8013; T.A. Callcott *et al.* (1978), *Phys. Rev. B* **18**, 6622; P.H. Citrin *et al.* (1979), *Phys. Rev. B* **20**, 3067; R.P. Gupta and A.J. Freeman (1976), *Phys. Lett.* **59A**, 223; W. Hänsch and W. Ekardt (1982), *Phys. Rev. B* **25**, 7815; K. Saito and T. Sagawa (1981), *J. Phys. Soc. Jpn.* **50**, 1660.

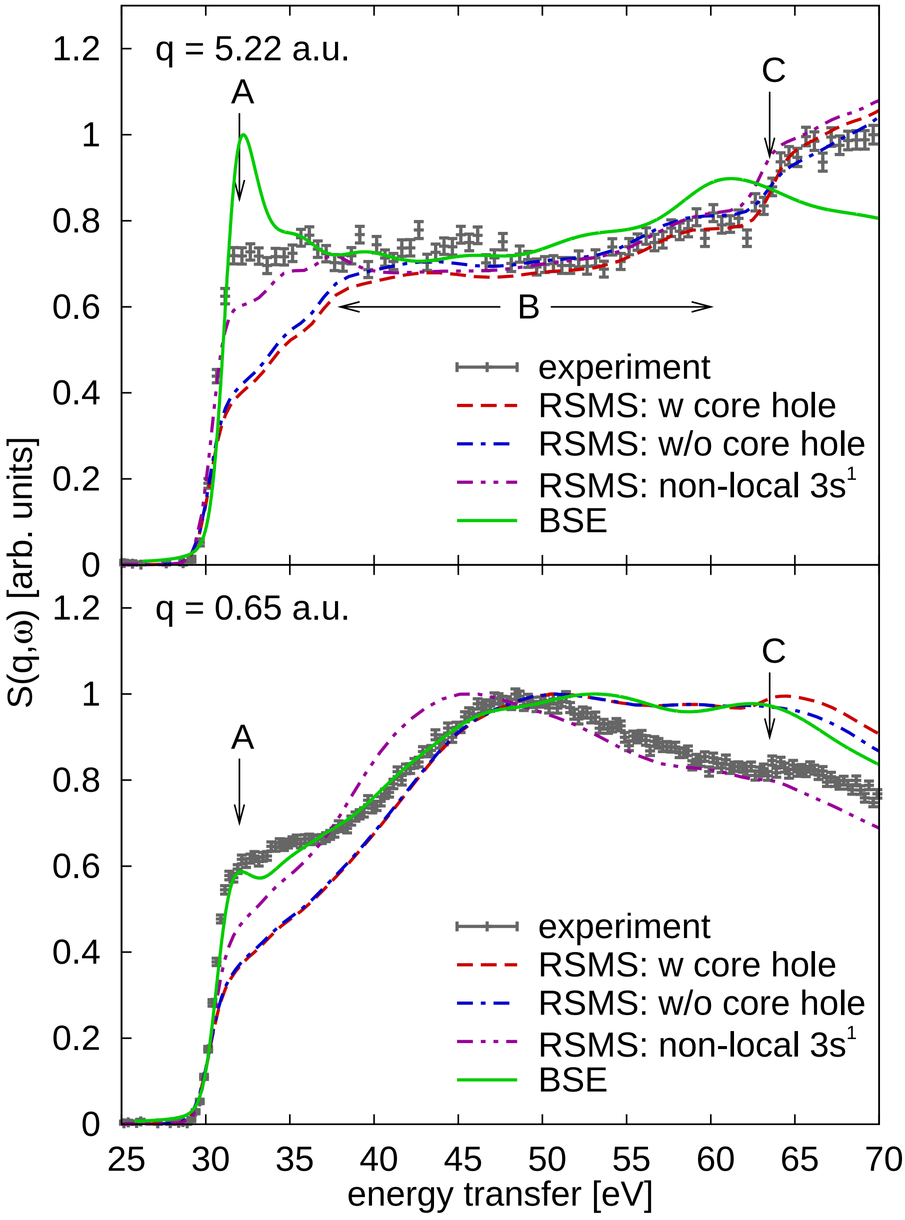

Figure 5.5: NRIXS spectra of the sodium $L_{II,III}$–edges at $q = 0.65$ a.u. (bottom) and $q = 5.22$ a.u. (top). Calculations as in Fig. 5.1. The sodium L_I–edge is not included in the BSE calculations. Moreover, the result of the RSMS calculation with the non–local exchange model assuming only the 3s^1 electron in the valence band is shown (dotted line).

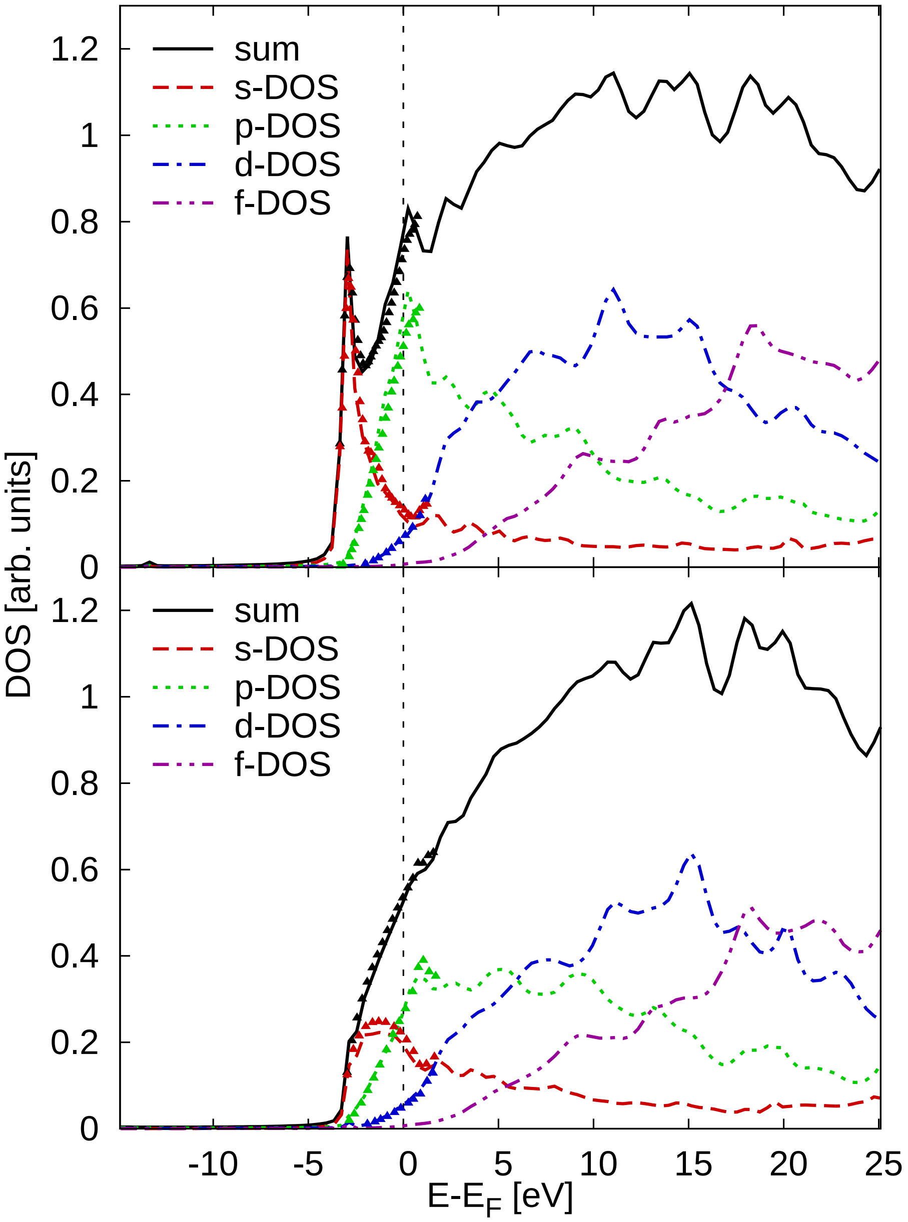

Figure 5.6: l–DOS of sodium. Lines: Final–state l–DOS of sodium calculated by the RSMS using the Hedin–Lundqvist self–energy (bottom) and a partially non–local model in $3s^1$ configuration (top) as discussed in the text. Symbols: LCAO calculations by von Barth and Grossmann for uncharged Na (bottom) and for Na^+ with a hole in the $2p$ band.

accomplished only recently using NRIXS, and the results were discussed in the framework of BSE calculations.[28] In the following, the general shape and fine structure of the sodium L–edges over an energy regime of 40 eV are discussed using different approaches for the treatment of the self–energy within RSMS calculations.

The results for sodium are shown in Fig. 5.5. For the two momentum transfers, there is only little difference between the RSMS calculations with and without core hole. Thus, it can be assumed that the core hole is almost completely screened by the outer electrons within this approach. The energy onset is always underestimated while BSE fits very well for low q and even overestimates the white line for high q. For the RSMS approach, better results have been achieved using a partially non–local model for the self–energy.[29] In this approach, the Hedin–Lundqvist self–energy is used for valence electrons, whereas core electrons are treated within the Dirac–Fock model.[30] The default valence configuration in the FEFF8.2 code is $\mathsf{2p^6 3s^1}$. In the calculations shown here, only the $\mathsf{3s^1}$ electron is defined as a valence electron. These changes cause parts of the electron density to be pushed out of the core region leading to a more attractive final–state potential. This causes the enhancement of the near–edge features as compared to the calculation based on Hedin–Lundqvist exchange. Similar changes in the spectrum due to the non–local exchange were also observed in Cu by Ankudinov *et al.*[31] The calculation with modified valence occupation and a non–local exchange model shows better agreement for both q with the experiment at the edge onset as can be seen in Fig. 5.5.

As presented in Fig. 5.6, for the pure Hedin–Lundqvist calculation, the projected l–DOS exhibits very good agreement with LCAO calculations of sodium by von Barth and Grossmann.[32] Furthermore, it shows a good qualitative agreement with similar SK–LCAO parameterized DFT calculations by Papaconstantopoulos[33] not shown here. For the calculations using the partially non–local model the l–DOS agrees well with LCAO calculations[34] for Na^+ assuming a hole in the 2p band. The strong peak of the p–DOS explains the rise of the RSMS calculation close to the edge. Since p → p is a dipole forbidden monopole transition it becomes clear why this effect is predominantly visible for high q. The better agreement within a calculation showing the l–DOS similar to a Na^+ gives rise to the assumption that the screening of the core hole is overestimated in the calculations with a pure Hedin–Lundqvist exchange model. For high momentum transfer, all calculations show good agreement with the experiment in range B. The shape and the relative weight

---

[28] C. Sternemann *et al.* (2005*a*), *Phys. Rev. B* **72**, 035104.

[29] A.L. Ankudinov and J.J. Rehr (1997), *J. Phys. IV France* **7**, C2.

[30] A.L. Ankudinov *et al.* (1996), *Comp. Phys. Comm.* **98**, 359.

[31] A.L. Ankudinov *et al.* (1998*a*), *Phys. Rev. B* **58**, 7565.

[32] U. von Barth and G. Grossmann (1979), *Solid State Comm.* **32**, 645.

[33] D. Papaconstantopoulos (1986), *Handbook of the Band Structures of Elemental Solids*, Plenum, New York.

[34] U. von Barth and G. Grossmann (1979), *Solid State Comm.* **32**, 645.

of the sodium L_I–edge (feature C) is well reproduced by all RSMS calculations, especially for high q. This seems reasonable since larger screening can be expected for deep–lying initial states.

5.3.4 General remarks

The RSMS implementation takes the interaction of the electron with the core hole into account by means of the final–state rule.[35] The effect of the core hole can be estimated by comparison with calculations assuming full screening. Calculations with the core hole show better agreement near the edge onset. The position of the features far above the edge is better with full screening. This might in part be due to the inaccuracies of the Hedin–Lundqvist quasi–particle shift. In magnesium, for example, at large momentum transfer, the near edge is hardly reproduced neglecting the core hole, whereas agreement is very good for higher energy transfer and low q. In case of sodium, the difference between the two calculations is negligible. This indicates that the core hole is screened completely and can be manually adjusted by using the non–local exchange model instead of Hedin–Lundqvist. In the case of semiconductors, as shown here for silicon, the edge onset can be broadenend due to the LDA approximation and due to finite cluster size. Apart from that, the quality of the calculations is as good as for the metals. Altogether, the BSE calculations show good overall agreement with the measured spectra, especially at the edge onset, and also most of the fine structures are well reproduced. For the edge onset of sodium, the results are excellent for low momentum transfer. For large q, the calculations yield an extra peak not present in the experiment. On the high energy side of the silicon edge for low momentum transfer, the deviations between BSE and experiment are quite large, whereas the agreement is much better at high q.

Except for the details discussed above, the quasi one–particle RSMS calculations agree with the BSE results, both in the general shape as well as in the fine structure. Overall one can conclude that the RSMS yields reliable descriptions of the non–resonant inelastic x–ray scattering spectra and can be applied to more complex systems, for which other methods are not feasible. Thus, FEFF can be used to study complex systems using NRIXS in a manner similar to XAS.

5.4 Conclusions and outlook

It has been demonstrated that RSMS is capable of reproducing the q–dependent non–resonant inelastic x–ray spectra of L–edges. The general shape of the edges and most of the fine structures agree well with the experiments. However, in the case of silicon, the

---

[35] J.A. Soininen *et al.* (2005), *Phys. Rev. B* **72**, 045136.

RSMS approach is not able to reproduce the edge onset, which can be related to finite cluster size broadening and the deficiency of LDA calculations concerning the bandgap of semiconductors and insulators. Nevertheless, some eV above the edge, the calculations for silicon agree well with the experiment. Although differences between the experiment and the results from the NRIXS adaptation of the FEFF8.2 code have been found as discussed in the text, in general the overall shape along with the q–dependence of the spectra is reproduced. Thus, this approach can be applied to systems which are not accessible with other computational methods. These include amorphous materials as well as systems with large unit cells.

Chapter 6

Disproportionation of bulk amorphous silicon monoxide

Bulk amorphous silicon monoxide (a–SiO) is a promising material regarding the search for new materials in (opto–)electronics and semiconductor technology. Structures containing silicon nanocrystallites in an oxide matrix are valuable alternatives to fragile, porous silicon on the way towards high–efficient photoluminescence from silicon–based materials.[1] Amorphous SiO shows a phase separation (disproportionation) under annealing combined with the formation of Si clusters. Therefore, it has attracted great interest as a starting material for the production of photoluminescent structures.[2] By phase separation within superlattices of SiO/SiO_2, even a size–controlled growth of Si nanoclusters could be achieved.[3] Another application of SiO_2 embedded Si nanocrystals prepared from SiO_x/SiO_2 multilayer structures has been discussed by Lu *et al.*[4] Due to the small size of the Si crystals and their charge–storage stability, these structures are important candidates for advanced non–volatile flash memories. The compatibility of SiO/SiO_x to the prevailing silicon technology in microelectronics makes SiO the favorable material for such applications. SiO_2 is the most important insulator for silicon integrated circuits. With the still ongoing gate miniaturization, oxide layers nowadays have a thickness of only a few nanometers. Due to the lattice mismatch, SiO_2 cannot directly grow on silicon in a crystalline phase but has to be amorphous.[5] The structural characterization of amorphous silicon/oxygen systems is therefore of particular relevance. The dependence on the Si and SiO_2 cluster sizes is of special interest and not well understood yet. For the development of theoretical descriptions of the SiO_x structure, mainly for the suboxide region, bulk–sensitive experiments are necessary. They, however, are still a challenge.

---

[1] A. Zimina *et al.* (2006), *Appl. Phys. Lett.* **88**, 163103.

[2] V. Kapaklis *et al.* (2005), *Appl. Phys. Lett.* **87**, 123114; M. Mamiya *et al.* (2001), *J. Cryst. Growth* **229**, 457.

[3] M. Zacharias *et al.* (2002), *Appl. Phys. Lett.* **80**, 661.

[4] T.Z. Lu *et al.* (2006), *J. Appl. Phys.* **100**, 014310.

[5] D.R. Hamann (2000), *Phys. Rev. B* **61**, 9899.

Since silicon/germanium alloys moved into the focus for nanoelectronic applications,[6] also the study of amorphous ternary $Si_xGe_yO_z$ compounds became important, especially at the SiGe/oxide interface. An approach to their structure can result from a comparison of a–SiO and a–GeO.

In this chapter, a study of the disproportionation process of bulk a–SiO by means of NRIXS will be presented. NRIXS is sensitive to the chemical environment, i.e. the different oxidation states of the silicon atoms. The momentum–transfer dependence allows the selection of excitation channels and therewith a maximization of the spectral differences between Si/SiO_2 and SiO_x. As discussed in chapter 4, in general, also the retrieval of the projected density of states is possible for multi–q experiments. This would yield a deeper understanding of the local electronic and chemical structure in SiO. Furthermore, in contrast to soft x–ray absorption, the high incident energy in NRIXS comes along with a high bulk sensitivity so that surface effects, as e.g. oxidation, can be neglected.

The chapter is organized as follows: First, different structure models for a–SiO will be outlined, then the experimental results will be presented and compared for different annealing temperatures. The findings on the disproportionation process will be discussed and compared with results of a similar experiment on bulk amorphous GeO by means of RIXS. A summary and a short outlook will be given at the end.

6.1 Models for bulk amorphous silicon monoxide

Bulk crystalline Si and SiO_2 consist of tetrahedrally coordinated Si atoms with four neighboring silicon or oxygen atoms respectively. The silicon atoms are therefore all in the same oxidation states, Si^0 for Si and Si^{4+} for SiO_2. In principle, silicon atoms in bulk a–SiO can be surrounded by four arbitrary silicon or oxygen atoms in the first coordination shell, i.e. $Si(Si_{4-n}O_n)$ clusters with $0 \leq n \leq 4$. Therefore, all five oxidation states Si^{+n} with $0 \leq n \leq 4$ are possible. Depending on configuration and oxidation of the neighboring atoms, the clusters vary in their bonding distance so that in total 75 different coordinations are possible. Also considering a random distribution of the second coordination shell and therewith a random distribution of bonding angles, silicon atoms in a–SiO can appear in a vast number of different surroundings.

In the past decades, the atomic structure of bulk amorphous silicon monoxide has been studied by various techniques and several structure models have been proposed.[7] However, so far, there has been no unambiguous experimental evidence for a certain model. The

---

[6] S. Balakumar *et al.* (2007), *Appl. Phys. Lett.* **90**, 032111; T. Busani *et al.* (2001), *J. Non–Cryst. Solids* **280**, 177; M. Zacharias *et al.* (1997), *J. Appl. Phys.* **81**, 2384.

[7] For a comprehensive overview see: A. Hohl *et al.* (2003), *J. Non–Cryst. Solids* **320**, 255, and references therein.

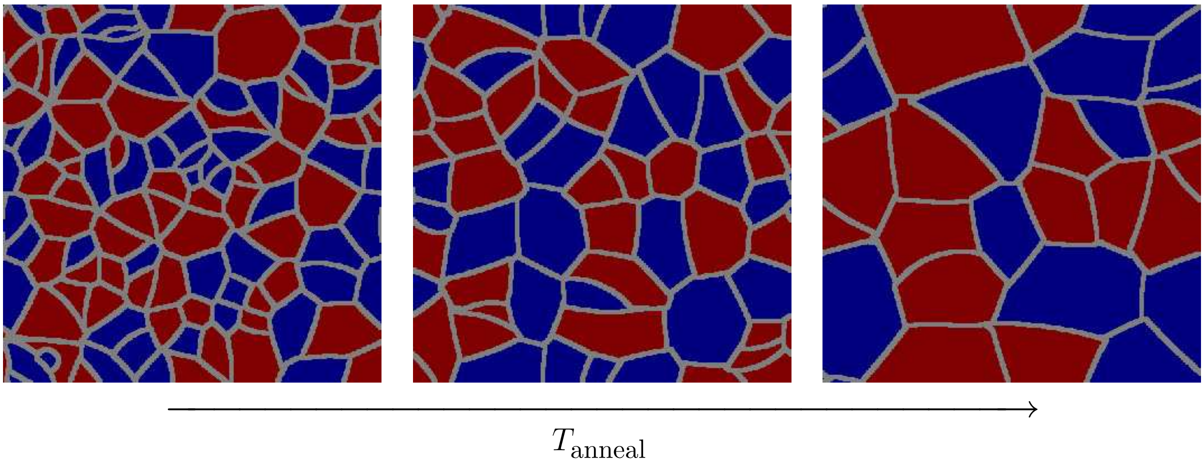

Figure 6.1: Illustration of the a–SiO disproportionation for increasing annealing temperatures T_{anneal} within the ICM model. Si (blue) and SiO_2 (red) domains are separated by a suboxide SiO_x interface (gray). For increasing annealing temperature, the Si and SiO_2 domains grow in size and the volume fraction of the suboxides decreases.

limiting theories for the a–SiO structure are the *random–bonding* (RB) model by Philipp[8] and the *random–mixture* (RM) model by Temkin.[9] The RB model describes a continuous random network with a binomial distribution of $Si(Si_{4-n}O_n)$ tetrahedrons. Within the RM model, instead, a disproportionation into separate phases of Si and SiO_2 is assumed. However, the proposed grain size of the different phases is in the nanometer–length scale and leads to a significant interfacial region between Si and SiO_2, which is neglected in the RM model. NMR[10] and XANES studies by Friede *et al.*[11] and Belot *et al.*[12] indicate that none of these models can fully explain the experimental results.

Recently, Hohl *et al.*[13] proposed an *interface clusters mixture* (ICM) model similar to the RM model but also taking the suboxide contribution[14] between domains of Si and SiO_2 into account. Native bulk amorphous SiO is assumed to be a frozen non–equilibrium system of a disproportionation in the initial state. Depending on the production conditions, it consists of amorphous SiO_2 clusters, amorphous nanometer–sized Si clusters, and suboxide interfaces (approx. 10 at.%) between these clusters. The structure of a–SiO is therefore between the limits of the RB (almost only suboxides) and the RM model (no suboxides). Therefore, these two limits define a range of possible degrees of disproportionation for

---

[8] H.R. Philipp (1971), *J. Phys. Chem. Solids* **32**, 1935; H.R. Philipp (1972), *J. Non-Cryst. Solids* **8–10**, 627.

[9] R.J. Temkin (1975), *J. Non-Cryst. Solids* **17**, 215.

[10] Nuclear magnetic resonance.

[11] B. Friede and M. Jansen (1996), *J. Non-Cryst. Solids* **204**, 202.

[12] V. Belot *et al.* (1991), *J. Non-Cryst. Solids* **127**, 207.

[13] A. Hohl *et al.* (2003), *J. Non-Cryst. Solids* **320**, 255.

[14] A suboxide phase consists of $Si(Si_{4-n}O_n)$ tetrahedra with $1 \leq n \leq 3$.

a–SiO.

The disproportionation process can externally be induced by temperature exposure. The growth of the Si and SiO_2 domains with increasing annealing temperature is illustrated in Fig. 6.1. In the low temperature initial state the small size of the grains leads to a large internal surface and thus to a significant suboxide volume fraction. If the disproportionation is more advanced at higher annealing temperatures, this contribution becomes less and less significant until it is fully negligible in the limit of the RM model.

For a quantitative study of the interfacial suboxide contribution, NRIXS is a suitable method due to its high bulk sensitivity. The existence of suboxides in the bulk has already been proven by this technique.[15] In the following, two experiments will be presented to study the disproportionation process of a–SiO and a–GeO by comparing the Si L–edges and Ge K–edge respectively, for samples annealed at different temperatures.[16]

6.2 Experiment

6.2.1 Amorphous silicon monoxide

The a–SiO experiment has been carried out at the APS beamline XOR/PNC 20–ID employing the LERIX setup.[17] NRIXS spectra have been recorded at 19 different momentum transfers for native a–SiO,[18] a–SiO after annealing at 800 ℃ and 1000 ℃, and for the references Si and SiO_2. The important experimental parameters are given in table A.2 (keys B_n). The powder samples were pressed into pellets and the experiments were performed in reflection geometry with an incident angle of 10°. Thus, the two smallest momentum transfers at scattering angles $\phi = 9°$ and $\phi = 18°$ were partially or fully shadowed by the sample. All a–SiO NRIXS spectra were extracted from the raw data sets as for Si and SiO_2 utilizing the algorithm presented in chapter 4. The q–dependence of the near–edge region of the three a–SiO samples are shown in Fig. 6.2. As discussed in chapter 4.2.3 for SiO_2, the silicon $L_{II,III}$–edge spectra in a–SiO are superimposed by EXAFS–like oscillations of the oxygen L_I–edge (41.6 eV). Since only the first 15 eV above the silicon $L_{II,III}$–threshold will be considered in the following, the oxygen L_I–contribution is approximated by a constant so that below the silicon $L_{II,III}$–threshold, the spectra are set to zero. For high momentum transfer, i.e. when the maximum of the Compton profile is at higher energy losses than

---

[15] C. Sternemann *et al.* (2005*c*), *J. Phys. Chem. Solids* **66**, 2277.

[16] The a–GeO experiment has been performed with RIXS at the germanium K–edge instead of NRIXS. The bulk sensitivity is ensured by the high incident energy corresponding to the electron binding energy of 11103 eV.

[17] See chapter 3.2.3 for details of the beamline and experiment setup.

[18] All a–SiO samples were prepared by A. Hohl, Institut für Materialwissenschaft, TU Darmstadt. Native a–SiO is condensed from a gas phase and has a corresponding annealing temperature of about 600 ℃ due to this process.

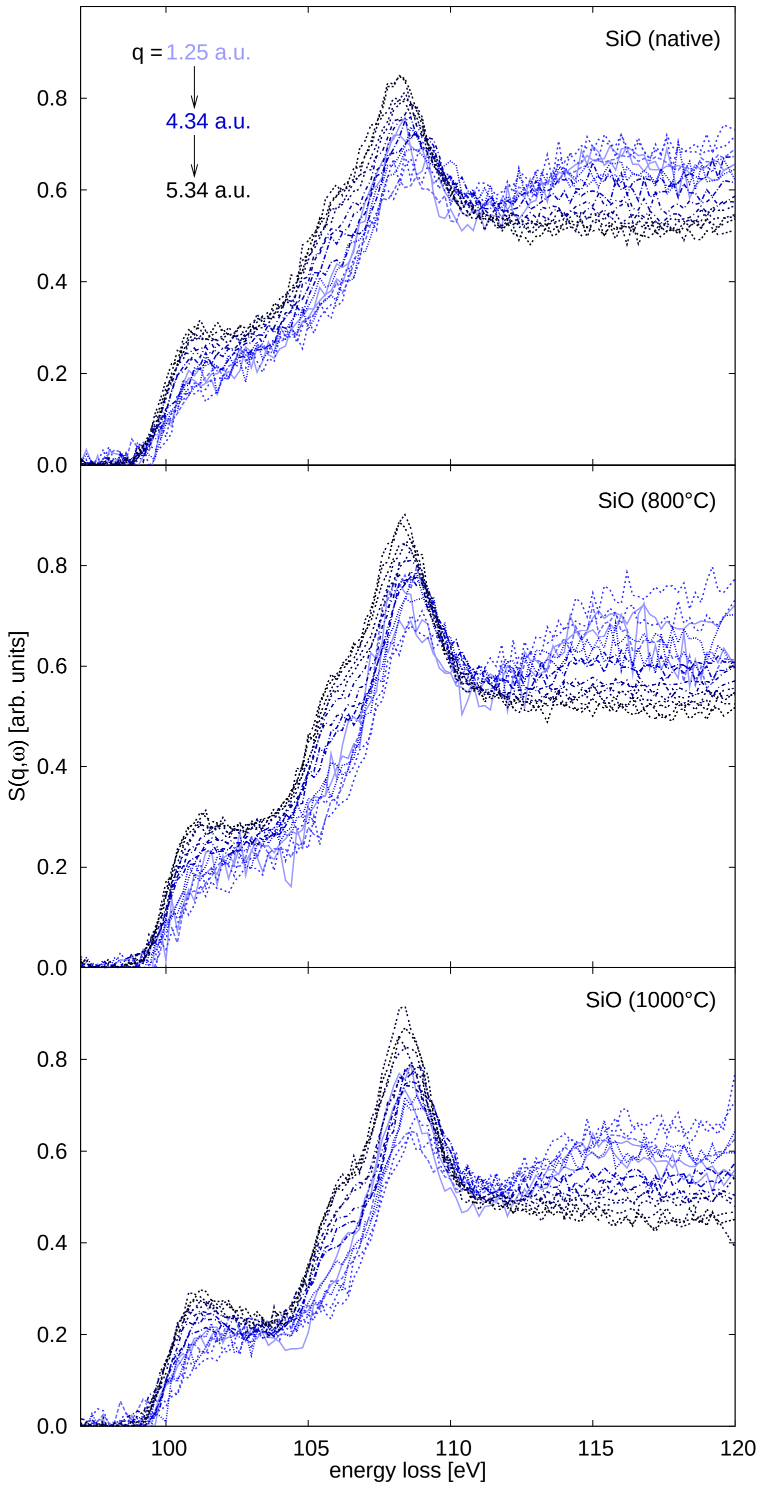

Figure 6.2: Extracted NRIXS spectra of the silicon $L_{II,III}$–edges in native a–SiO (top), after annealing at 800 ℃ (middle) and at 1000 ℃ (bottom). All spectra are normalized to their area between 95 eV and 120 eV.

the silicon $L_{II,III}$–edge onset, absolute normalization of the full spectrum to the number of electrons shows good results for the a–SiO spectra with different annealing temperatures. For low q, this normalization is impossible since a Pearson function is used for background subtraction instead of normalized Compton or particle–hole profiles. For intermediate momentum transfer, the background subtraction is performed as for high q, but systematic errors are larger. Thus, for the determination of spectral differences, the full spectrum up to an energy loss of 1200 eV was used for normalization of the four largest momentum transfers and the area between energy losses 95 eV and 120 eV for the others. In Fig. 6.2, however, all spectra are normalized to the same area as the smaller momentum transfers to give a comparable picture of the data quality and q–dependence.

6.2.2 Amorphous germanium monoxide

The study of the disproportionation of bulk amorphous GeO has been accomplished[19] by means of Resonant Inelastic X–ray Scattering (RIXS) at the 1 m Rowland circle setup of BL9 at the Dortmunder Elektronenspeicherring–Anlage DELTA.[20] The x–rays from a superconducting asymmetric wiggler source were monochromatized using a Si(311) double crystal monochromator. With the Si(553) analyzer crystal, a total energy resolution of 3.1 eV could be achieved. The RIXS spectra were recorded in partial fluorescence yield by scanning the incident energy with a fixed analyzer at the germanium K_{α_1}–fluorescence (9.886 keV for atomic germanium). The scattering angle ϕ was chosen to be 90° to reduce the background from elastic scattering.

The Ge powder sample (Goodfellow, 99.999% purity) was pressed into a pellet and brought into the beam in reflection geometry. The amorphous GeO samples were condensed as a μm–thick film on a molybdenum substrate.[21] The wafer was sliced into 10×10 mm^2 pieces which were then annealed under high vacuum conditions (10^{-7} mbar) for 30 minutes at different temperatures T_{anneal} up to 400 ℃. During the experiment, some of the samples were annealed ex–situ under vacuum ($5 \cdot 10^{-6}$ mbar) for temperatures up to 720 ℃. However, for $T_{\text{anneal}}>500$ ℃, a change of the stoichiometry was observed a posteriori by energy dispersive x–ray analysis.[22] For the highest annealing temperature, the stoichiometry was determined to be GeO_2. Thus, the according RIXS spectrum is used as GeO_2 reference for the analysis. All measured spectra were corrected for background scattering. The absorption correction could not be included due to the lack of absorption factors for the sample. The spectra for a–GeO with $T_{\text{anneal}}<500$ ℃ and for Ge and GeO_2

---

[19] A. Schacht (2007), "Untersuchung der Disproportionierung von massivem amorphen Germaniummonoxid", diploma thesis, Universität Dortmund.

[20] C. Krywka *et al.* (2006), *J. Synch. Rad.* **13**, 8.

[21] All a–GeO samples were prepared by A. Hohl, Institut für Materialwissenschaft, TU Darmstadt.

[22] J.C. Russ (1984), *Fundamentals of energy dispersive x–ray analysis*, Butterworths, London.

T_{anneal} [°C]	suboxide contribution [%]
native: 600	15.5±0.5
800	12.5±0.5
1000	6±1

Table 6.1: Suboxide contribution in a–SiO for different annealing temperatures.

were normalized to the area between incident energies of 11100 eV and 11150 eV and are shown in the top part of Fig. 6.5. By x–ray diffraction for T_{anneal}>500 °C a recrystallization of the sample could be observed as well. This leads to additional fine structure in the according RIXS spectra as indicated by the arrow in Fig. 6.5 for GeO_2. However, this sample turned out to be favorable as reference compared to a commercially available GeO_2 crystalline powder.

6.3 Results and discussion

The extracted silicon $L_{II,III}$–edges for Si, SiO_2 and three a–SiO samples are presented for three momentum transfers in the left part of Fig. 6.3. The quality of the spectra is best for higher momentum transfers since the Compton background is lower and can be removed with higher accuracy. It also turns out that the feature–rich shape of the high–q absorption edge yields higher sensitivity for the suboxide contributions. For rising annealing temperatures, the near–edge structure of the silicon $L_{II,III}$–edges in a–SiO shows various spectral changes. Around an energy loss of 104 eV (vertical line B), a decrease of weight is observed. At this energy loss, contributions from the Si suboxides are expected due to their smaller chemical shifts compared to SiO_2. In contrast to that, the weight of the pure Si contribution (see vertical line A in Fig. 6.3) and that of the characteristic SiO_2 white line (vertical line C) increases.

For increasing T_{anneal}, the a–SiO spectra approach the 1:1–superposition of the Si and SiO_2 spectra, which is the expected edge shape for a–SiO after full disproportionation, i.e. when no significant amount of suboxides is left. The differences between the a–SiO spectra and this (Si+SiO_2)–model are presented in the right part of Fig. 6.3 showing the disappearance of differences to the 1:1–model.

The spectral contribution from the suboxides, i.e. the signal from $Si(Si_{4-n}O_n)$ with $1 \leq n \leq 3$ can also be extracted directly from the a–SiO spectrum at $q = 5.34$ a.u. by subtraction of the corresponding signal from Si and SiO_2. For the suboxide contributions presented in Fig. 6.4, before subtraction, the (Si+SiO_2)–spectrum was normalized to the edge onset of the a–SiO spectrum, to which only $Si(Si_4O_0)$ contributes. The comparison of the integral between 95 eV and 120 eV of these spectra to the full a–SiO spectrum reveals

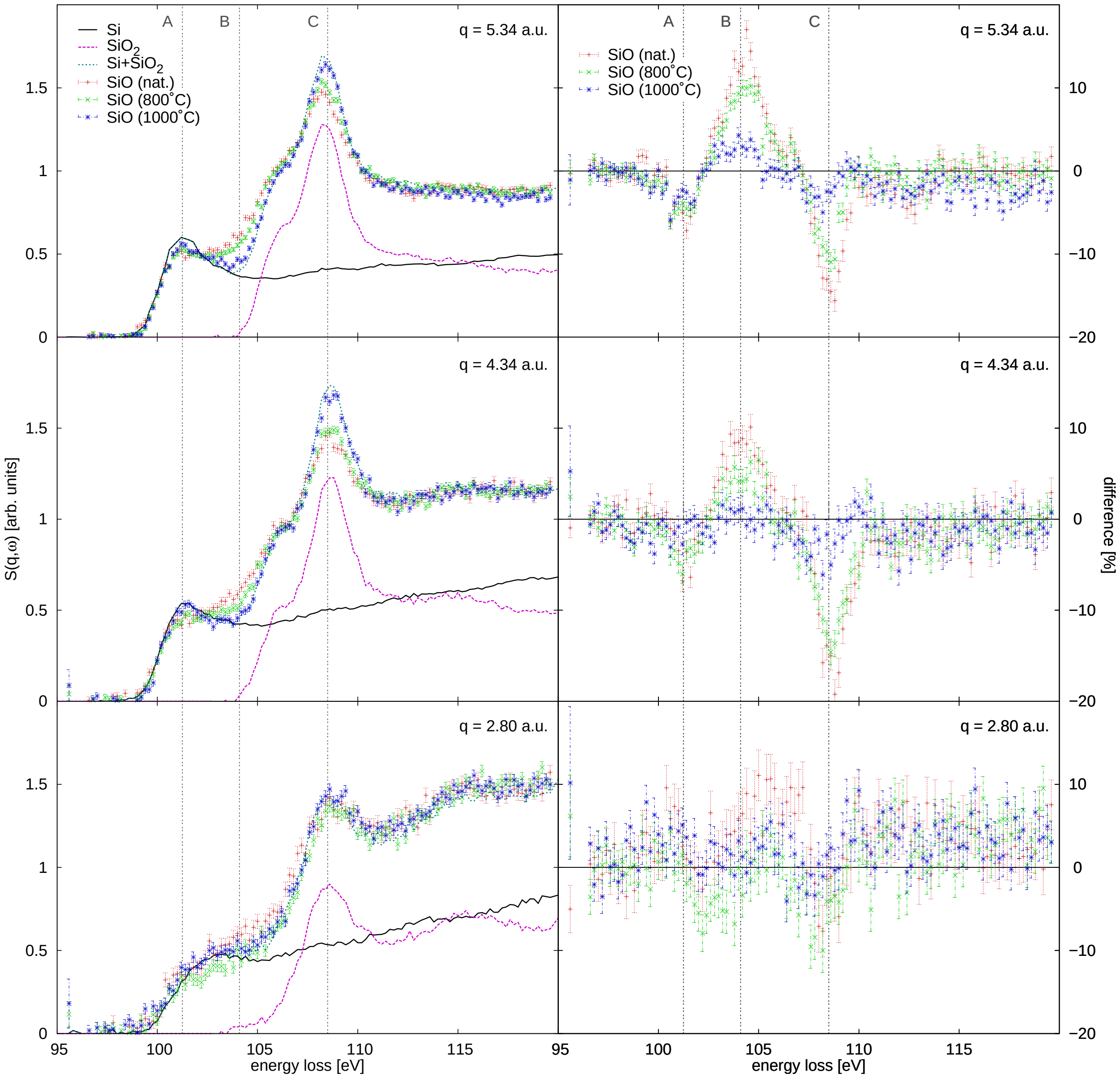

Figure 6.3: T_{anneal}–dependence of the silicon $L_{\mathrm{II,III}}$–edges in a–SiO for three different momentum transfers. The extracted spectra are compared to a 1:1–superposition of pure Si and SiO_2 (left). The differences to this spectrum show a progressive decline for higher annealing temperatures T_{anneal} (right). The differences are given relative to the maximum value of the ($Si+SiO_2$)–spectrum. Considering the q–dependence of the absorption–edge shape, the spectra for high momentum transfer prove to be most sensitive to suboxide contributions, i.e. to the disproportionation process. The vertical lines indicate the signal from pure Si (A), the maximum of the suboxide contribution (B) and the characteristic sharp white line of SiO_2 (C).

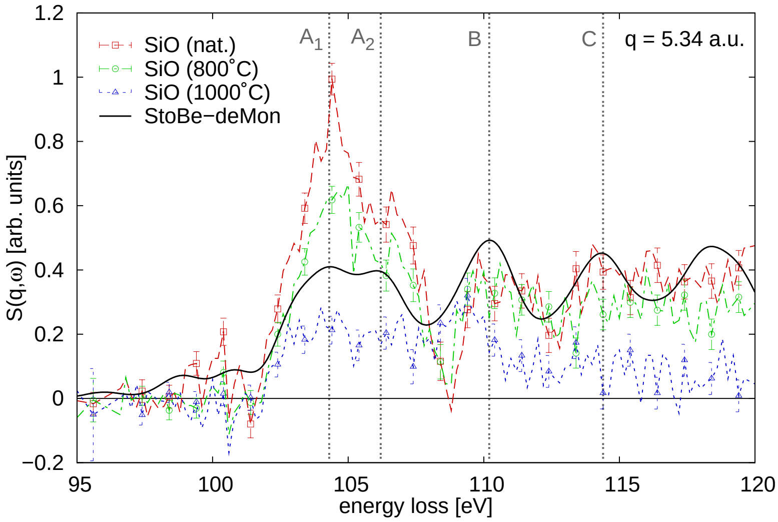

Figure 6.4: Suboxide contribution extracted from the a–SiO spectra ($q = 5.34$ a.u.) by subtraction of the $Si(Si_4O_0)$– and $Si(Si_0O_4)$–signal. The results are compared to ab–initio DFT calculations based on the StoBe–deMon code. Prominent spectral features of the calculations are assigned by A–C.

an atomic proportion of $(15.5 \pm 0.5)\%$ for native a–SiO, $(12.5 \pm 0.5)\%$ after annealing at 800 ℃ and $(6 \pm 1)\%$ after annealing at 1000 ℃. The errors are estimated by the dependency on the upper integration limit.[23] The results are also summarized in Tab. 6.1.

The spectra in Fig. 6.4 are compared to calculations which have been performed by A. Sakko employing an ab–initio NRIXS approach based on the StoBe–deMon code.[24] NRIXS spectra were calculated for suboxide forming tetrahedra, convoluted with the experimental energy resolution and then added according to an assumed binomial distribution for the suboxides according to the RB model.[25] The qualitative agreement between theory and experiment is good. The broad onset with the two maxima assigned by $A_{1,2}$ is well reproduced in width and maxima spacing. Also widths and position of the maxima assigned by B and C seem to be in agreement, although fine structure at this energy regime above the excitation threshold can be significantly influenced by the second or third coordination shell and thus definitive conclusions demand calculations for larger clusters. This is also the case for spectral weights of the fine structure. However, the calculations indicate the proper experimental extraction of the suboxide contributions in a–SiO. Therefore, a study of the signal originating only from the suboxide interfaces is worthwhile. Moreover, the StoBe–deMon approach yields a promising tool to understand the suboxide contributions of a–SiO from a theoretical point of view.

---

[23] This, however, might not be the only source of systematic errors. Statistical errors for the integral are negligible compared to systematic errors.

[24] See chapter 2.4 and A. Sakko *et al.* (2007), *Phys. Rev. B* **76**, 205115.

[25] See chapter 6.1.

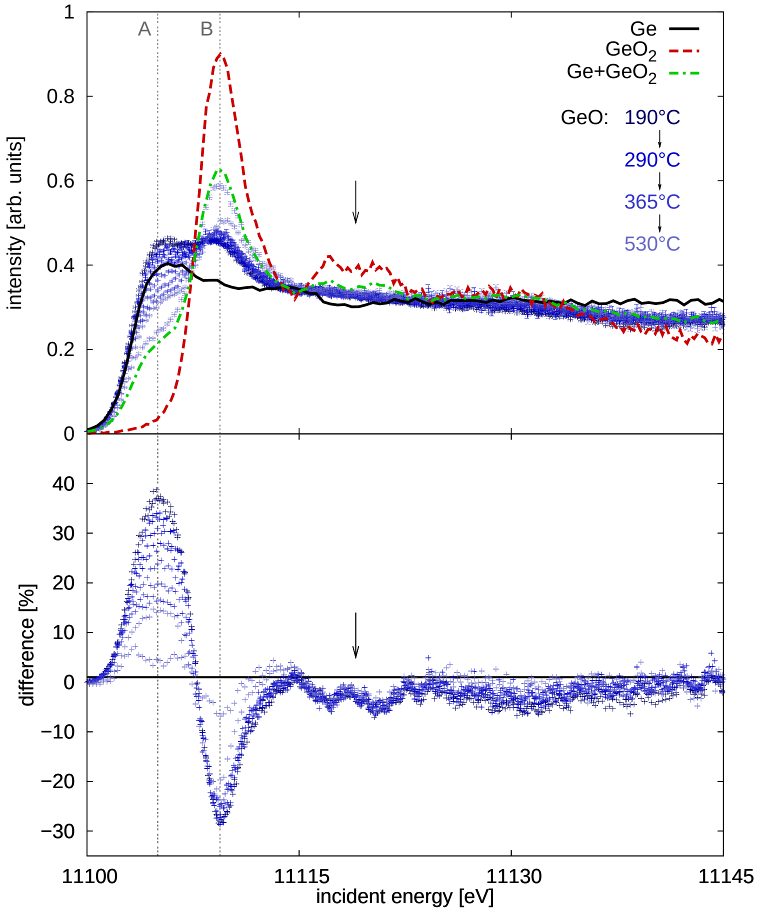

Figure 6.5: T_{anneal}–dependence of the germanium K_{α_1}–edge in a–GeO. The RIXS spectra are compared to a 1:1–superposition of pure Ge and GeO$_2$ (top). The arrow indicates fine–structure due to recrystallization in the GeO$_2$ reference.

The germanium K_{α_1}–edge in a–GeO shows a T_{anneal}–dependence very similar to the a–SiO results. It can be seen in the top part of Fig. 6.5 that, for rising temperature, the spectra show a convergence towards the 1:1–superposition of the Ge and GeO$_2$ spectra. For native a–GeO, the characteristic sharp GeO$_2$ white line is strongly suppressed (vertical line B) but gains weight during the disproportionation process. Simultaneously, the spectral weight below the GeO$_2$ onset (vertical line A) decreases. As for a–SiO, this is the energy regime, at which the onsets of the suboxide contributions are expected. The bottom part of Fig. 6.5 shows the differences between the a–GeO spectra and the (Ge+GeO$_2$)–model. The structure indicated by the arrow origins from the GeO$_2$ reference spectrum showing a certain degree of recrystallization.

To quantify the temperature dependence of the disproportionation process of a–SiO and a–GeO, a parameter A for the degree of disproportionation will now be derived. The spectral weight of the germanium K_{α_1}–edge in a–GeO can be assumed to be a linear

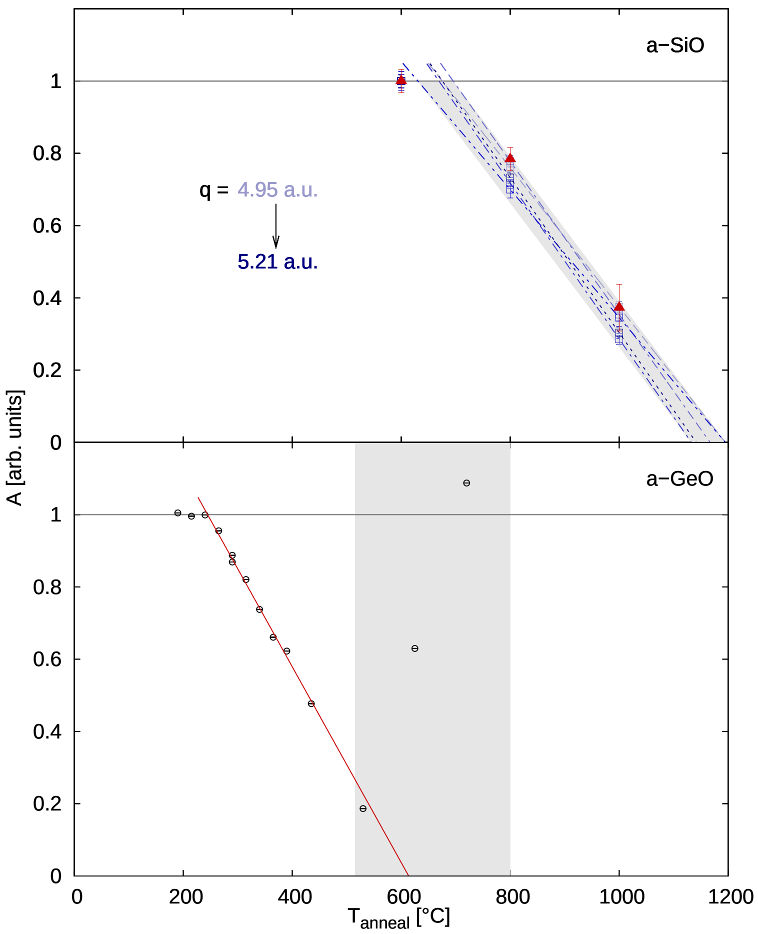

Figure 6.6: Disproportionation of a–SiO (top) and a–GeO (bottom). The results of the integral A for different q are shown for a–SiO (open squares). The shadowed region yields the according uncertainty for the onset temperature and the disproportionation course. The suboxide fractions from Fig. 6.4 were normalized to the result for native a–SiO and are shown for comparison (filled triangles). For a–GeO, samples in the shadowed temperature region showed a change in stoichiometry due to the annealing process and also partial recrystallization.

combination of the contributions from $Ge(Ge_{4-n}O_n)$ with $0 \leq n \leq 4$. For a fraction x of germanium atoms in suboxide surrounding (i.e. $1 \leq n \leq 3$), the total intensity $I_{\mathrm{GeO}}(\omega)$ can be written as

$$I_{\mathrm{GeO}}(\omega) = (1-x) \cdot [I_{\mathrm{Ge}}(\omega) + I_{\mathrm{GeO_2}}(\omega)] + x \cdot I_{\mathrm{sub}}(\omega), \tag{6.1}$$

where I_{sub} is the contribution from the suboxides. The differences shown in the bottom part of Fig. 6.5 can then be expressed as

$$d = I_{\mathrm{GeO}}(\omega) - [I_{\mathrm{Ge}}(\omega) + I_{\mathrm{GeO_2}}(\omega)] = x \cdot (I_{\mathrm{sub}}(\omega) - [I_{\mathrm{Ge}}(\omega) + I_{\mathrm{GeO_2}}(\omega)])\,. \tag{6.2}$$

Since the difference is proportional to the suboxide fraction x, the integral A of the absolute difference $|d|$ is a reasonable measure for the degree of disproportionation:

$$A = \int_{E_1}^{E_2} |I_{\mathrm{GeO}}(\omega) - [I_{\mathrm{Ge}}(\omega) + I_{\mathrm{GeO_2}}(\omega)]|\, d\omega, \tag{6.3}$$

where E_1 =11098 eV and E_2 =11113 eV to exclude the GeO_2 EXAFS–like structure indicated by the arrow in Fig. 6.5. For native a–GeO, A is normalized to one and it is shown for different annealing temperatures in the bottom part of Fig. 6.6. Up to $T_{\mathrm{anneal}} = 240\,°C$, no changes in the absorption edges are observed, then A shows a linear decrease till $T_{\mathrm{anneal}} \approx 500\,°C$. For full disproportionation, A should approach zero since the germanium K_{α_1}–edge in fully disproportionated GeO is expected to be a linear combination of the germanium K_{α_1}–edge in Ge and in GeO_2. Thus, an extrapolation of the linear fit in the bottom part of Fig. 6.6 predicts $T_{\mathrm{anneal}} = 600\,°C$ as end–temperature for the disproportionation process. By contrast, the experimental results show a rising of A for temperatures above 500 °C. This is due to the change in stoichiometry during the annealing process from a–GeO to GeO_2. For a study of the disproportionation behavior in this temperature regime, an experiment with optimized annealing conditions, especially with better vacuum during the annealing process, is required.

The considerations for a–GeO concerning disproportionation parameter A are also valid for the case of a–SiO. A has been calculated in analogy to Eqn. (6.3) for differences of the silicon $L_{\mathrm{II,III}}$–edges as presented in Fig. 6.3. The integration has been carried out between energy losses E_1 = 100 eV and E_2 = 110 eV. In the top part of Fig. 6.6 the results are shown for the five largest momentum transfers between 4.95 a.u. and 5.34 a.u., where the changes in the spectrum for different temperatures are the strongest. The behavior of A as a function of T_{anneal} is very similar for the different q and give a consistent general view. A mean start temperature of $(660 \pm 50)\,°C$ was found for the disproportionation process. According to the linear fits for each q–value, the end–temperature lies between 1100 °C and 1200 °C. For smaller q, the results show larger deviations from the shadowed area in Fig. 6.6. This can be due to the larger errors because of worse statistics and smaller changes of the spectra during the disproportionation process. However, Fig. 6.6 also shows the relative suboxide contributions to the full a–SiO spectra presented in Tab. 6.1 (red triangles). The good agreement with the temperature dependence of parameter A supports these results. In conclusion, the disproportionation behavior of a–SiO is comparable to the behavior of a–GeO, but the according temperature regime is significantly higher. For a finer determination of the disproportionation onset and the final temperature point, a similar study is required for several annealing temperatures between $T_{\mathrm{anneal}} = 600\,^{\circ}\mathrm{C}$ and $T_{\mathrm{anneal}} = 1200\,^{\circ}\mathrm{C}$.

6.4 Conclusions and outlook

The disproportionation process of amorphous silicon monoxide has been studied by means of NRIXS. At different momentum transfers, spectra for native a–SiO and for a–SiO after an annealing process at 800 °C and 1000 °C were compared to a Si+SiO_2 reference. For rising annealing temperatures, the spectra show a convergence towards the assumed spectrum for a–SiO after full disproportionation. The remaining deviations to this reference spectrum could be used as a measure for the degree of disproportionation. The results for the different momentum transfers yield a consistent temperature behavior. The onset of the disproportionation process could be determined to be $(660 \pm 50)\,^{\circ}\mathrm{C}$. The temperature of full disproportionation could be extrapolated to a temperature regime between 1100 °C and 1200 °C.

Furthermore, for the first time, the spectral contributions of the suboxides to the full spectra could be extracted for different annealing temperatures. The results were compared to ab–initio DFT calculations showing a good agreement. From the spectral weight of the suboxide contribution the proportion of SiO_x in a–SiO could be quantitatively estimated. The results are in very good agreement with the disproportionation behavior studied by the differences of the spectra. A comparison with a similar RIXS study on the disproportionation of bulk amorphous germanium monoxide shows the similarity in behavior for rising annealing temperatures. The results of both studies are in line with the assumed disproportionation behavior according to the ICM model. The temperature regime for a–SiO, however, is much higher than for a–GeO.

According to the presented studies, the a–SiO disproportionation process is determined to take place between 600 °C and 1200 °C, whereas the temperature region is 240 °C to 600 °C for a–GeO. Further studies of a–SiO with a finer grid of annealing temperatures in the disproportionation range can now be used to improve the accuracy of the results. Moreover, a study of the end point of disproportionation can answer the question of the minimum amount of suboxides possible in a–SiO.

The similarities of the disproportionation behavior of a–SiO and a–GeO give also rise to a future study of the disproportionation of ternary $\mathrm{Si}_x\mathrm{Ge}_y\mathrm{O}_z$ compounds. In the light of silicon/germanium nanostructures[26] and growth of faster metal oxide semiconductor field effect transistors (MOSFETs) on silicon/germanium alloys,[27] these compounds are of special industrial interest since the oxide films can strongly influence the quality of nanoelectronic devices.

---

[26] M. Zacharias *et al.* (1997), *J. Appl. Phys.* **81**, 2384.

[27] S. Balakumar *et al.* (2007), *Appl. Phys. Lett.* **90**, 032111; T. Busani *et al.* (2001), *J. Non–Cryst. Solids* **280**, 177.

Chapter 7

Study of the barium giant dipole resonance in nanostructured silicon compounds

For many decades, silicon has been the most important element for electronic devices. The electronic properties of silicon can be altered by doping with donors and acceptors, which makes it a versatile substrate in semiconductor industry. In the recent years, complex nanostructured bulk silicon compounds revealing attractive physical properties have become the focus of fundamental research and material science. One of the most prominent classes of such compounds are clathrates.

Silicon clathrates are networks built up from different silicon nanocages, which can contain guest atoms. These materials have attracted much interest in the past years due to their special physical properties. Depending on the guest atom, the clathrates exhibit a wide range of behavior from superconductivity to magnetic order.[1] The guest atom can also induce special band–electronic and thermo–electric structure in the system.[2] For various doped clathrates surprising high–pressure properties have been revealed.[3] Especially the silicon clathrate Ba_8Si_{46} has been studied extensively due to its rich high–pressure phase diagram of structural and electronic phase transitions.[4] Ba_8Si_{46} and also $Ba_{24}Si_{100}$ are prepared from the orthorhombic $BaSi_2$ by application of high–temperature (about 800 ℃) and high–pressure conditions (about 1.5–3 GPa).[5] Recently, it was discovered by Yamanaka

---

[1] C.L. Condron *et al.* (2005), *Inorg. Chem.* **44**, 9185; H. Kawaji *et al.* (1995), *Phys. Rev. Lett.* **74**, 1427; Y. Mudryk *et al.* (2002), *J. Phys.: Condens. Matter* **14**, 7991.

[2] G.B. Adams *et al.* (1994), *Phys. Rev. B* **49**, 8048; D. Kahn and J.P. Lu (1997), *Phys. Rev. B* **56**, 13898; G.S. Nolas *et al.* (2001), *Semicond. Semimet.* **69**, 255.

[3] See, e.g., A. San Miguel and P. Toulemonde (2005), *High Pressure Res.* **25**, 159 and references therein for a comprehensive overview.

[4] T. Kume *et al.* (2003), *Phys. Rev. Lett.* **90**, 155503; A. San Miguel *et al.* (2005), *Europhys. Lett.* **69**, 556; L. Yang *et al.* (2006), *Phys. Rev. B* **74**, 245209.

[5] H. Fukuoka *et al.*, *J. Organomet. Chem.* **611**, 543; S. Yamanaka *et al.*, *Inorg. Chem.* **39**, 56.

et al.[6] that at even higher temperatures (1000 ℃) and pressures (15 GPa), a new silicon–rich Ba/Si structure $BaSi_6$ is formed. Its structure is visualized in Fig. 7.1, as are the structures of Ba_8Si_{46} and $Ba_{24}Si_{100}$.[7] Unlike clathrates, the $BaSi_6$ crystal is not composed of cages but barium atoms are enclosed in deformed polyhedra of 16 silicon atoms each. DFT calculations predict metallicity for $BaSi_6$.[8]

Questions like the bonding of the barium atoms in complex silicon networks and their role for physical properties of the material require an insight into the electronic and the structural neighborhood of the dopants. Provided that the enclathrated atoms show atomic giant dipole resonances, as is the case for atomic barium, their study can be used to obtain a deeper understanding of the local and electronic structure.

7.1 The barium giant dipole resonance

The giant dipole resonance[9] of atomic and ionized barium in the $4\mathsf{d} - \mathsf{f}$ transition regime is an extensively studied phenomenon caused by collective excitations of 4d electrons.[10] Connerade[11] presents a simple quantum–well model for the potential in the inner region. Below a certain critical atomic number Z, the potential in the quantum well is not strong enough for a bound state of the 4f wave functions in the inner region. For $Z \geq 55$ (Cs), the 4f orbitals then collapse and are localized within the quantum well.[12] Thus, the spatial overlap of 4d and 4f orbitals leads to a strong excitation channel for $4\mathsf{d} \rightarrow \mathsf{f}$ excitations. In a condensed matter view the giant resonance of barium might be understood as a single damped oscillator of the 4d–shell electrons driven by the electric field of the x–rays. This induces a dipole charge separation and thus a time–dependent internal electric field. According to Zangwill,[13] the charge oscillation is in phase with the external field below the resonance threshold, so that the induced field screens the external field inside the 4d–shell charge radius. Above the resonance onset, the charge oscillates out–of–phase so that the

---

[6] S. Yamanaka and S. Maekawa (2006), *Z. Naturforsch.* **61b**, 1493.

[7] The structures are visualized by means of a parallel stereoscopic figure, i.e. it can be viewed three–dimensionally by looking at the left picture with the left eye and at the right picture with the right eye.

[8] S. Yamanaka and S. Maekawa (2006), *Z. Naturforsch.* **61b**, 1493.

[9] The term "giant resonance" was originally introduced in nuclear physics for collective excitations of the nucleons as observed by Baldwin and Klaiber: G.C. Baldwin and G.S. Klaiber (1947), *Phys. Rev.* **71**, 3; G.C. Baldwin and G.S. Klaiber (1948), *Phys. Rev.* **73**, 1156.

[10] C. Bréchignac and J.P. Connerade (1994), *J. Phys. B: At. Mol. Opt. Phys.* **27**, 3795; (1987), *Giant Resonances in Atoms, Molecules, and Solids*, ed. by J.P. Connerade *et al.*, Plenum, New York; M. Richter *et al.* (1989), *Phys. Rev. A* **39**, 5666; G. Wendin (1973), *Phys. Lett. A* **A–46**, 119.

[11] J.P. Connerade (1987), "Controlled collapse and the profiles of 'giant resonances'", *Giant Resonances in Atoms, Molecules, and Solids*, Plenum, New York.

[12] U. Becker (1987), "The 4d + 4f giant resonance from barium through the rare–earths", *Giant Resonances in Atoms, Molecules, and Solids*, Plenum, New York.

[13] A. Zangwill (1987), "A condensed matter view of giant resonance phenomena", *Giant Resonances in Atoms, Molecules, and Solids*, Plenum, New York.

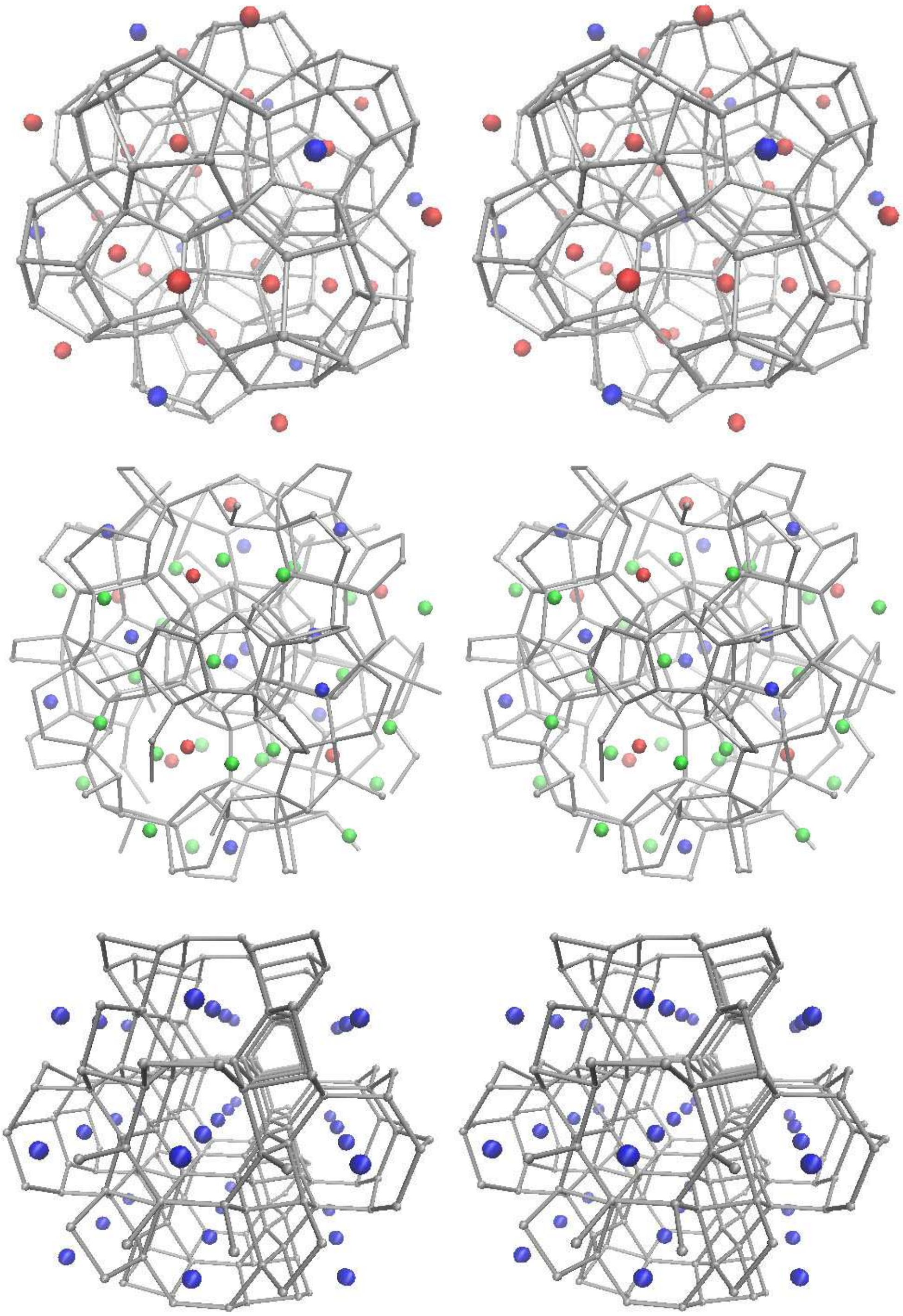

Figure 7.1: Stereoscopic images (parallel) of the structure of Ba_8Si_{46} (top), $Ba_{24}Si_{100}$ (center), and $BaSi_6$ (bottom). Barium atoms are colored blue, red and green designating the different symmetry sites of barium for each structure.

internal field amplifies the external field in this regime.

As an intrinsic atomic feature, shape and strength of the giant resonance have shown to be independent of the atomic bonding state, i.e. whether it is a single atom, part of a molecule, or even in the condensed phase.[14] However, when such an atom is placed inside complex surroundings, e.g. cagelike nanostructures, modulations in the fine structure of the resonances are predicted by theory.[15] They can be attributed to the symmetry of the cage and the position of the intercalated atom. This was emphasized by Luberek and Wendin,[16] who presented calculations of the x–ray absorption near–edge spectra of endohedral fullerenes Ba@C_n. Their modeled spectra show fingerprint–like structures in the shape of the barium giant resonance depending on the size and the shape of the carbon cages as well as on the position of the guest atom in a cage. A strong distortion of the Xe $\mathsf{4d-f}$ giant resonance in Xe@C_{60} was predicted recently by calculations of Amusia *et al.*[17] The resonance fine structure of a barium trapped in a fullerene is predicted to be highly sensitive to changes of the local environment of the barium atom because of modulations caused by standing waves of the scattered electron within the carbon cages. For the theoretical description of the giant resonance, dynamical screening of the electromagnetic x–ray field has to be accounted for. Within the calculations of Luberek and Wendin or Amusia *et al.*, dynamical screening was considered employing TDLDA.

As discussed in chapter 2.2.3, also version 8.4 of the real space multiple scattering approach FEFF supports dynamical screening by a TDLDA implementation for XAFS calculations. To probe the quality of this approach, in this work, spectra were calculated within random–phase approximation (RPA) for Ba@C_{60} (with centered and off–centered barium atom) and Ba@C_{90} and were compared with the results of Luberek and Wendin[18] in Fig. 7.2. In all three cases, the spectra show good qualitative agreement concerning the general shape and fine structure. Quantitative discrepancies are found for positions and weight of the spectral maxima. Nevertheless, the comparison allows to conclude that modulations of the barium giant resonance can in principle be calculated employing FEFF. The comparison of the spectra for Ba@C_{60} with centered and off–centered barium makes clear that only a slight change of the guest atom position can lead to dramatic changes in the fine structure as calculated by theory. This prediction emphasizes the potential of experiments on the barium giant resonance.

Experimentally, the barium giant resonance has been observed in a solid for, e.g., La–

---

[14] So the barium giant resonance has an asymmetric profile of about 40 eV width with a steep onset above 100 eV energy loss, a flattened maximum around 110–115 eV and a smooth decrease up to 140 eV.

[15] G. Wendin and B. Wästberg (1993), *Phys. Rev. B* **48**, 14764.

[16] J. Luberek and G. Wendin (1996), *Chem. Phys. Lett.* **248**, 147.

[17] M.Y. Amusia *et al.* (2006), *J. Exp. Theor. Phys.* **102**, 53.

[18] The valence contribution to the absorption cross section in the calculations of Luberek and Wendin has been subtracted by a function $\sigma_{\mathrm{v}}(\omega) \propto \omega^{-3}$.

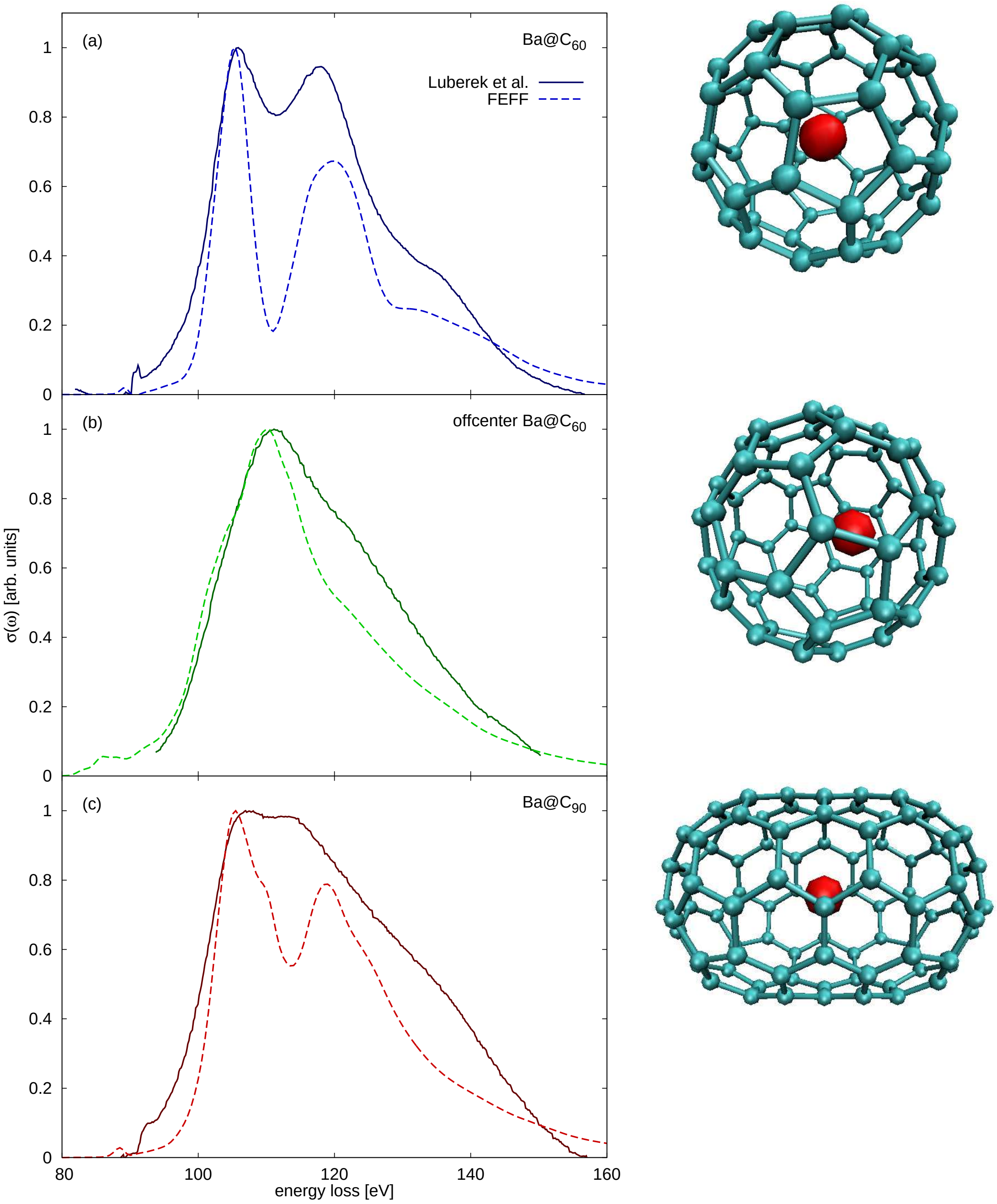

Figure 7.2: Photoabsorption cross section of the barium giant resonance for (a) Ba@C_{60}, (b) offcenter Ba@C_{60}, and (c) Ba@C_{90} within TDLDA. The RPA FEFF results (dashed) are compared with the calculations of Luberek *et al.* (solid). The structure of each intercalated fullerene is shown on the right.

and Ce–halides[19] or $YBa_2Cu_3O_{7+x}$.[20] In 2005, Mitsuke *et al.*[21] found first experimental evidence in ionized Ce@C_{82} for the appearance of the giant resonance with the resonating atom trapped inside a complex cage–like environment. However, the latter experiment indicates the existence of the resonance but hardly allows conclusions on its particular shape and fine structure. Therefore, the modulation of the resonance by the local surrounding has not been proven so far.

Barium–doped silicon clathrates and $BaSi_6$ have comparable structures to the Ba@C_n network. Therefore the barium giant resonance spectra are also expected to be sensitive to their surrounding. A study of the resonance for these compounds can therefore help to answer the questions stated above, i.e. the character of the bonding between dopant and host network and the dopant's role for the physical properties of the material and the understanding of the giant resonance in general. It is also of special interest in the view of high–pressure studies as changes in the local environment, e.g. off–center positions of the guest atoms in the Si cages, can be induced across phase transitions and would manifest themselves in the modulation of the resonance's shape.

This chapter is organized as follows: First, details will be given on the experiment and on the RSMS calculations of the giant resonance in different barium/silicon compounds. Then, the q–dependence and fine structure of the giant resonance in NRIXS spectra will be discussed. Furthermore, the results of a first high–pressure NRIXS experiment of Ba_8Si_{46} will be presented. A conclusion and an outlook are given at the end.

7.2 Calculation of the barium NRIXS spectrum

Calculations of the barium giant resonance have been performed within TDLDA for the clathrates Ba_8Si_{46} and $Ba_{24}Si_{100}$ and for the compounds $BaSi_6$, $BaSi_2$, and $BaSO_4$ by means of the RSMS approach FEFF, version 8.4. The crystallographic data of these structures is summarized in Tab. 7.1. Further structural information is given in appendix C. The unit cells of each system contain barium atoms at different symmetry positions. The calculation of the resonance was hence performed for each position separately and the results were added up considering the multiplicity of each position. An example of the calculations shall be given now for Ba_8Si_{46}: It is a type I silicon clathrate of space group $Pm\overline{3}n$ and consists of two different types of silicon cages, Si_{20} and Si_{24}, where each silicon atom is shared by four cages. The unit cell consists of 46 silicon atoms forming two dodecahedra and six tetrakaidecahedra, so that the number of the larger cages is three times the number of the smaller ones. With the barium atoms occupying the eight resulting cages, this leads

---

[19] S. Suzuki *et al.* (1975), *J. Phys. Soc. Japan* **38**, 156.
[20] M. Onellion *et al.* (1987), *Phys. Rev. B* **36**, 819.
[21] K. Mitsuke *et al.* (2005), *J. Chem. Phys.* **122**, 064304.

Compound	Space group	a [Å]	b [Å]	c [Å]	N_{sym}	$N_{\text{sym}}^{\text{Ba}}$
$BaSi_2$	Pnma	8.92	6.75	11.57	5	2
$BaSi_6$	Cmcm	4.49	10.38	11.97	4	1
Ba_8Si_{46}	$Pm\overline{3}n$	10.33	—	—	5	2
$Ba_{24}Si_{100}$	$P4_132$	14.07	—	—	9	3
$BaSO_4$	Pbnm	7.15	8.88	5.45	5	1
Si	$Fd\overline{3}m$	5.43	—	—	2	—
Si_{136}	$Fd\overline{3}m$	14.62	—	—	3	—

References: J. Evers (1980), *J. Solid State Chem.* **32**, 77 ($BaSi_2$), S. Yamanaka and S. Maekawa (2006), *Z. Naturforsch.* **61b**, 1493 ($BaSi_6$), S. Yamanaka *et al.*, *Inorg. Chem.* **39**, 56 (Ba_8Si_{46}), H. Fukuoka *et al.*, *J. Organomet. Chem.* **611**, 543 ($Ba_{24}Si_{100}$), S.D. Jacobsen *et al.* (1998), *Can. Mineral.* **36**, 1053 ($BaSO_4$), N.W. Ashcroft and N.D. Mermin (1976), *Solid State Physics*, Thomson Learning, London (Si), J. Dong *et al.* (1999), *Phys. Rev. B* **60**, 950 (Si_{136}).

Table 7.1: Crystallographic parameters for the barium–containing and reference compounds. a, b and c are the lattice constants, N_{sym} is the number of different symmetry positions in the unit cell, and $N_{\text{sym}}^{\text{Ba}}$ is the number of different symmetry positions occupied by barium atoms.

to the structure formula Ba_8Si_{46}. NRIXS spectra of the barium $N_{IV,V}$–edges have been separately calculated for barium in a small and in a large cage respectively, and spectra of the silicon L_{I-III}–edges have been calculated for the three different silicon symmetry sites in the clathrate network. For each spectrum, the near edge has been computed with full multiple scattering and extended energy loss range by path expansion.[22] The two partial spectra were then composed by scaling the latter to the near–edge spectrum in the energy range in which the spectra show overlap. Finally, the spectra were added up for the different sites with the multiplicities 2 and 6 for barium, and 6, 16 and 24 for silicon. This sum is then convoluted with the experimental resolution and can be compared with the experimental spectra.

The momentum–transfer dependence of the NRIXS spectra of Ba_8Si_{46} was calculated with the adaptation of the RSMS approach for NRIXS in the same manner as described above. The measurements were performed at a finite momentum transfer so that also non–dipole transitions appear. Therefore, the contribution of barium 4d $\rightarrow$ d monopole transitions to the total Ba_8Si_{46} spectrum, which appears for energy losses at about 98 eV, was extracted from the calculations. Contributions from other non–dipole transitions were found to be negligible. Dynamical screening and therefore collective excitations were not accounted for in these calculations.

---

[22] See chapter 2.2.2 for computational details.

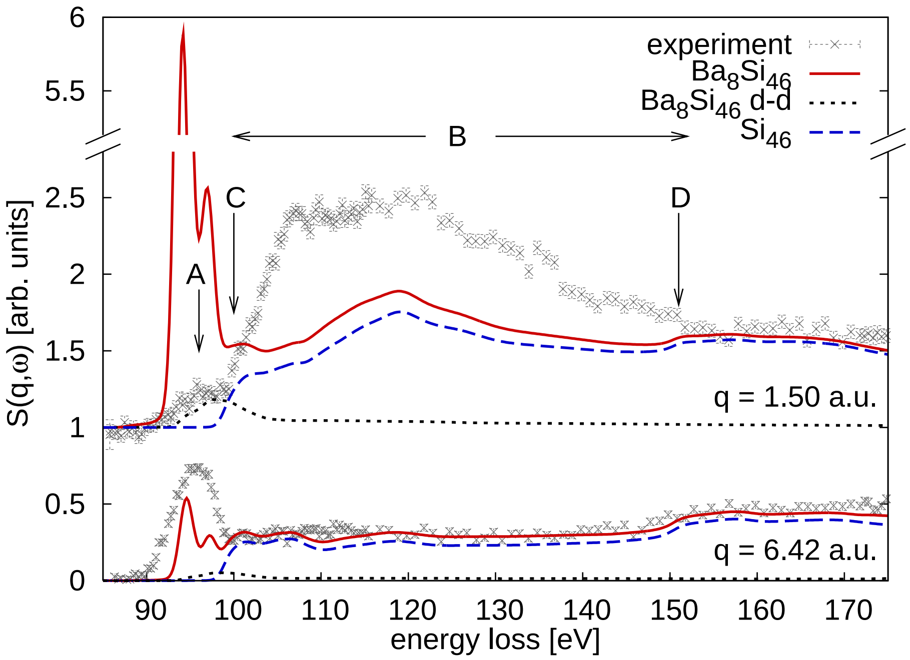

Figure 7.3: Experimental NRIXS spectra of Ba_8Si_{46} for $q = 1.50$ a.u. (top) and $q = 6.42$ a.u. (bottom) with associated RSMS calculations for the silicon contribution and the full Ba_8Si_{46} spectrum. The contribution arising from barium 4d → d excitations is indicated separately. A is the barium $N_{IV,V}$–edge, C and D are the onsets of the underlying silicon $L_{II,III}$–edges and the L_I–edge. The broad feature B, only visible in the dipole limit, can be attributed to the barium 4d − f giant dipole resonance. Collective excitations are not accounted for in the calculations.

7.3 Momentum–transfer dependence of the giant resonance

The dipole character of the barium giant resonance can be studied by NRIXS due to its momentum–transfer dependence allowing the selection of excitation channels. The experiment was performed at ESRF beamline ID16. All important parameters of the experiment are given in table A.2 (keys C_1, C_2). The NRIXS spectra of Ba_8Si_{46} for the low and the high momentum transfer are shown in Fig. 7.3. The barium $N_{IV,V}$–edges (92.6/89.9 eV) are indicated by A, the onset of the underlying silicon $L_{II,III}$–edges (99.8/99.4 eV) and the silicon L_I–edge (150 eV) of the host lattice by C and D respectively. The intense broad feature denoted by B only appears for the measurement in the dipole limit with low momentum transfer and is absent for large q. At such high momentum transfers, single particle–hole rather than collective excitations are probed and the weight of contributions from multipole transitions is increased. Therefore, feature B can be attributed to the 4d − f giant dipole resonance of barium. It shows good agreement with the experimental

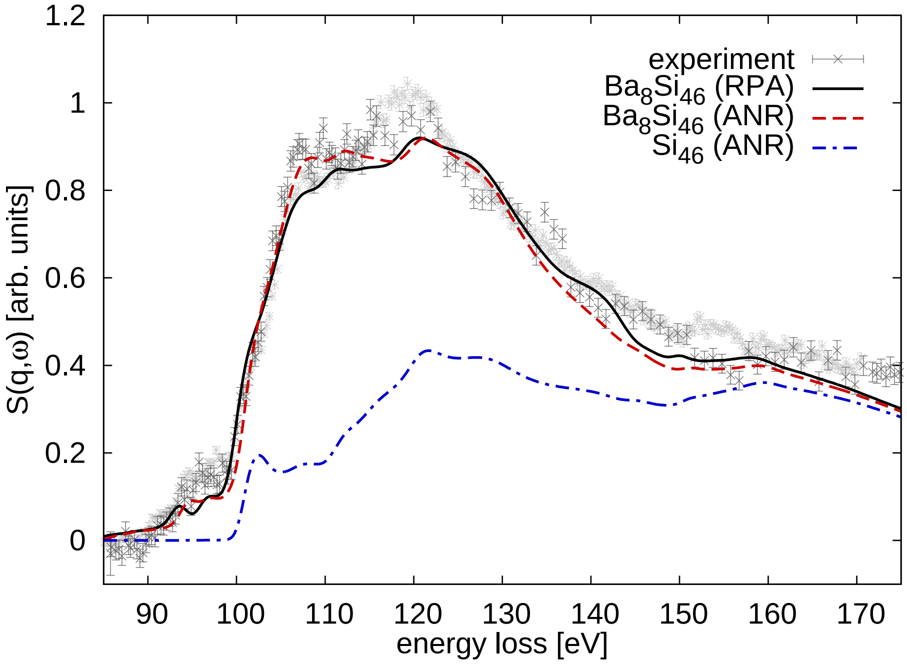

Figure 7.4: NRIXS spectrum of Ba_8Si_{46} for $q = 1.50$ a.u. and calculated XAS spectra employing TDLDA. The spectra were calculated for Ba_8Si_{46} in RPA and with dynamical core hole–electron screening (ANR). The exclusive contribution from the Si_{46} is presented separately. The result for $q = 1.37$ a.u. of the Ba_8Si_{46} experiment with the Medipix setup of ESRF ID 16 is shown as well (light gray) for comparison.

photoabsorption cross section of atomic barium in energy position and width as discussed by Richter *et al.*[23] These results are compared with calculations of the q–dependent NRIXS spectra in Fig. 7.3. The q–dependence of the underlying silicon edges is reproduced very well by the calculations as has been reported earlier.[24] Since this approach does not account for dynamical screening, the observed resonance (B) originating from collective 4d electron excitations[25] cannot be reproduced for low q. The spectral weight of the dipole transitions predicted by the calculations (at A) is transferred to the broad resonance peak (B) at higher energy losses in the experiment. For high q, the qualitative agreement is significantly better because the resonance is suppressed, but still the weight at the barium $N_{IV,V}$–edge onset (A) is not fully reproduced. These results emphasize that collective effects have to be accounted for.

In the dipole limit the TDLDA calculations for x–ray absorption can be compared with the experimental NRIXS spectra of the giant resonance for low momentum transfer. Calculations were performed within RPA and with the exchange correlation kernel f_{xc}

---

[23] M. Richter *et al.* (1989), *Phys. Rev. A* **39**, 5666.

[24] See chapter 5.3.1.

[25] M.A. Amusia and J.P. Connerade (2000), *Rep. Prog. Phys.* **63**, 41.

by Ankudinov, Nesvizhskii and Rehr[26] (ANR) and are compared with the experiment in Fig. 7.4. In RPA, only the external electromagnetic field of the x–rays is screened by core polarization whereas ANR also includes the frequency–dependent screening of the interaction between the excited electron and the core hole. The overall agreement between experiment and calculations is very good. The width and the relative strength of the giant resonance with respect to the calculated silicon edges agree very well with the experiment. The comparison of both calculations shows that the general feature of the giant resonance can already be explained within RPA. Nevertheless, the inclusion of core hole–electron screening improves the agreement in the steepness of the resonance onset. Remaining differences between the experiment and the theory above 115 eV might be related to the onset of double electron excitations as discussed by Richter *et al.*[27] Similar differences between experiment and calculation have also been observed for other Ba/Si compounds as presented in chapter 7.4. Moreover, for finite q, as it is the case for the experimental data in this work, still a certain non–dipole contribution[28] is expected, which is not accounted for in the calculated XAS spectra.

The quality of the experimental data shown in Fig. 7.4 does not allow the extraction of the barium giant resonance from the underlying silicon edge. Therefore, the experiment was performed again for Ba_8Si_{46} with higher statistics and focus on the resonance modulation. The result for $q = 1.37\,\text{a.u.}$ (key F_3) is also presented in Fig. 7.4. The previous spectrum shows deviations to the newer study, which in part can be attributed to the different momentum transfer but also to statistics and to the quality of background subtraction.

In the following, a study on the modulation of the resonances for different barium–containing compounds will be presented. It will be shown for the first time that it is possible to extract the differences between the modulations for different systems.

7.4 Modulation of the giant resonance

The sensitivity of the giant resonance fine structure to the local structural environment of the excited atom in complex compounds has been theoretically predicted more than ten years ago.[29] However, so far there has been no experimental proof for significant changes in the fine structure for different complex compounds. In the NRIXS study presented here, the giant resonance could be extracted for various compounds and their comparison reveals significant differences in the fine structure.

---

[26] A.L. Ankudinov *et al.* (2003), *Phys. Rev. B* **67**, 115120.

[27] M. Richter *et al.* (1989), *Phys. Rev. A* **39**, 5666.

[28] This can be, e.g., a monopole d → d contribution as shown in Fig. 7.3.

[29] J. Luberek and G. Wendin (1996), *Chem. Phys. Lett.* **248**, 147.

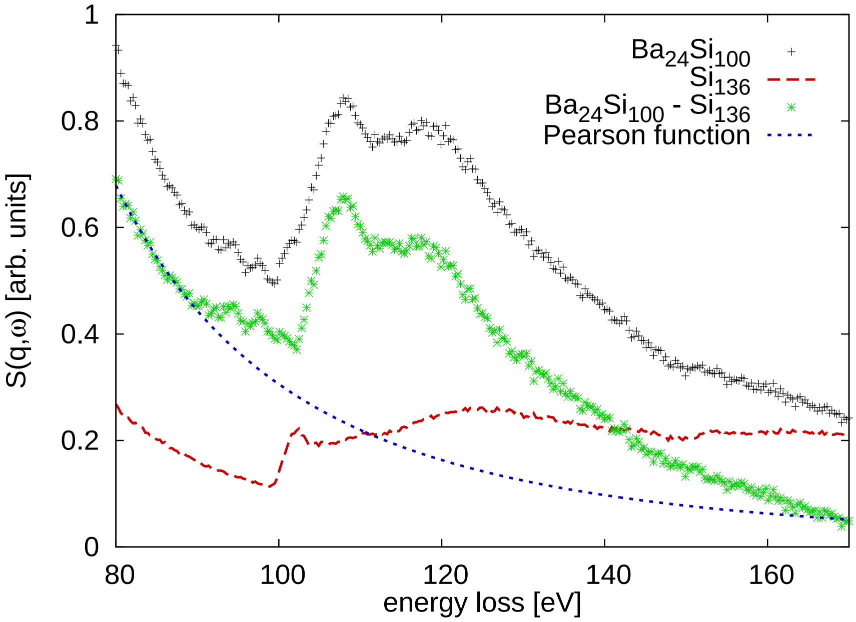

Figure 7.5: Extraction of the barium giant resonance for $Ba_{24}Si_{100}$ at $q = 1.08\,$a.u. The silicon contribution is removed from the raw $S(\mathbf{q}, \omega)$ by a Si_{136} spectrum measured at the same momentum transfer so that the complete barium spectrum from core and valence electrons remains. The barium valence–electron contribution can then be approximated by a Pearson function.

7.4.1 Experimental extraction of the giant–resonance modulations

The experiment has been performed with the Medipix setup at ESRF beamline ID16. All important experimental parameters are given in Tab. A.2 (key F_n). Spectra for Ba_8Si_{46}, $Ba_{24}Si_{100}$, $BaSi_6$, $BaSi_2$, and $BaSO_4$ were recorded as for the reference samples Si and Si_{136}. The setup allows the acquisition of spectra for five different momentum transfers simultaneously. However, the barium giant resonance could only be extracted for three of them. For the lowest q, the counting rate was too low and for the largest q, the particle–hole contribution obscuring the giant resonance spectrum cannot be approximated by a simple parameterized function. For the remaining three momentum transfers, the silicon contribution was removed by subtraction of an appropriate reference spectrum.[30] The remaining barium valence–electron contribution was fitted by means of parameterized Pearson functions and subtracted.[31] An example of a typical extraction is given in Fig. 7.5. For $BaSO_4$, only Pearson functions have been subtracted from the spectra.

The extracted barium contributions in the vicinity of the barium $N_{IV,V}$–edges are normalized to their integral between 101 eV and 150 eV energy loss and are shown in Fig. 7.6.

---

[30] Si has been used as reference for $BaSi_2$, Si_{136} has been used for Ba_8Si_{46}, $Ba_{24}Si_{100}$, and $BaSi_6$.

[31] For details of the NRIXS extraction process, see chapter 4.2.3.

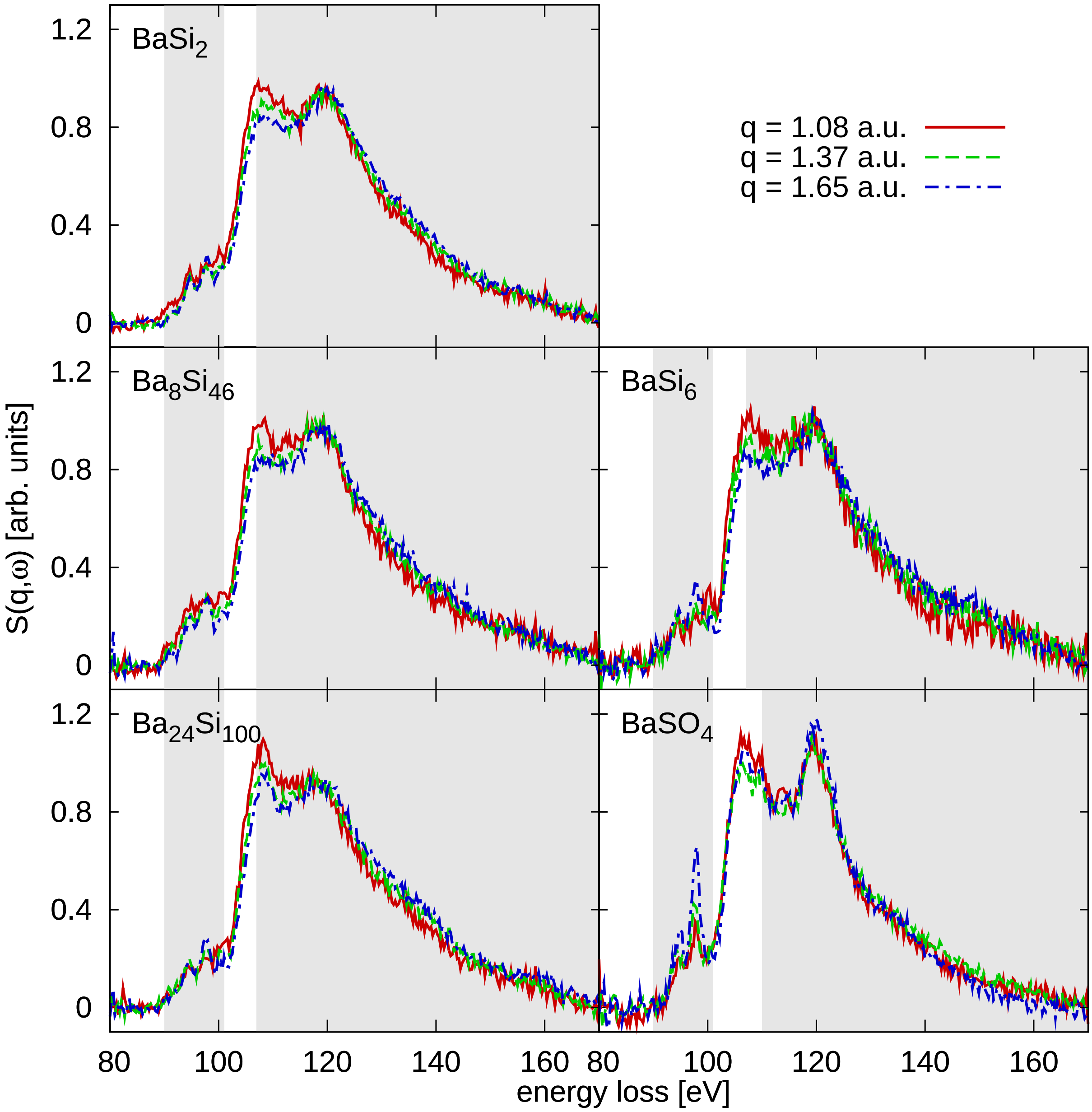

Figure 7.6: Momentum–transfer dependence of the barium giant resonance for different barium/silicon compounds. The shadowed region on the left marks the energy range before the onset of the giant resonance, the shadowed region on the right indicates the range in which double electron excitations are expected. For $BaSO_4$, this region is shifted to higher energies due to the ionic character of the compound.

The results can be partitioned into three energy regimes. Below the onset of the giant resonance at about 101 eV (left shadowed region), all spectra show a modulated shoulder corresponding to the barium $N_{IV,V}$–edge as visible in particular for high q in Fig. 7.3. This is also the region in which monopole transitions are expected by theory. The momentum–transfer dependence, especially for $BaSO_4$, supports this prediction. Since Fig. 7.6 is intended to show the momentum transfers of the resonance, this regime has been omitted for normalization. Double electron excitations superimposing the giant resonance spectrum, as discussed by Richter *et al.*,[32] are expected to occur for energy losses above 110 eV for $BaSO_4$ and above 107 eV for the other compounds (right shadowed region). Basically contributions from the resonance are assumed in between. The general shapes and widths of the resonances are very similar showing the high quality of the background subtraction by the Si/Si_{136} references. Only the resonance width of $BaSO_4$ is smaller, as it is an example of an ionic crystal.[33] The momentum–transfer dependence shows a consistent behavior for all compounds.

However, in detail, the fine structure shows strong variation between the compounds and can be extracted by subtraction of a reference spectrum for each q separately. $BaSi_2$ was chosen as reference since it is the less complex structure from a crystallographic point of view. Apart from $BaSO_4$, the modulations of the resonances prove to be basically independent of q as can be seen in Fig. 7.7. Thus, the differences for the three q–values can be added up to increase the statistics. The resulting modulations are compared with each other in Fig. 7.8. For $BaSO_4$, which shows a strong momentum–transfer dependence in the sharp features between 90 eV and 101 eV energy loss, only the difference for the lowest q is shown.

For all compounds, significant modulations from the reference sample $BaSi_2$ can be observed. The spectra for the clathrates and $BaSi_6$ show similarities in their general behavior concerning the position of minimal and maximal deviations, but also differ from each other in their fine structure. The deviations of $BaSO_4$ to the reference are larger in amplitude, which is due to the different width of the resonance as discussed above. These results for the first time show that modulations of the giant–resonance spectrum for different compounds can be experimentally extracted and distinguished.

7.4.2 Comparison with RSMS calculations

RSMS calculations in dipole limit of the giant resonance were performed for the presented compounds as discussed in chapter 7.2 and are now compared to the experimental results for the lowest momentum transfer $q = 1.08\,\text{a.u.}$ in Fig. 7.9. The widths and the general

---

[32] M. Richter *et al.* (1989), *Phys. Rev. A* **39**, 5666.

[33] A thorough discussion of the $BaSO_4$ spectrum is given in C. Sternemann *et al.* (2008*a*), *J. Anal. Atom. Spectrom.* DOI: `10.1039/B717441A`.

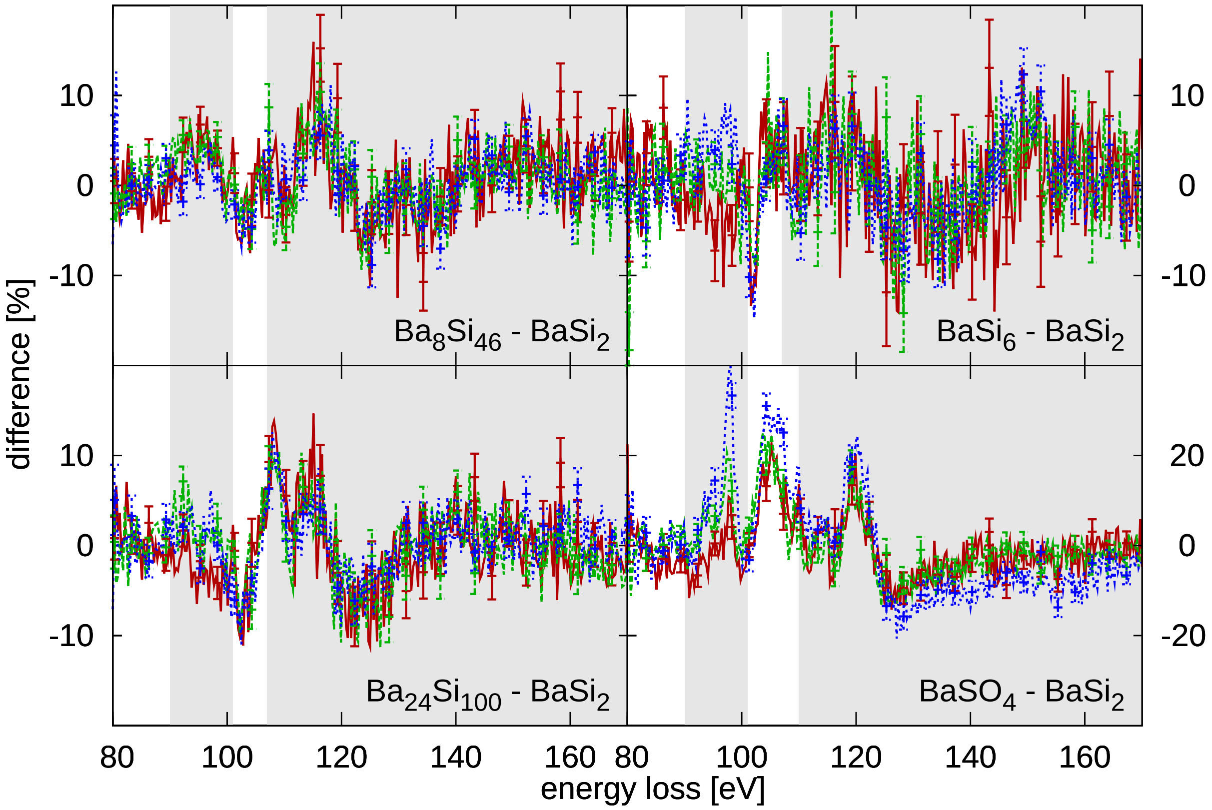

Figure 7.7: Modulations of the giant resonance fine structure with $BaSi_2$ as reference spectrum. The differences prove to be mainly independent of the momentum transfer. Thus, an average over q can increase the statistics without a quality reduction of the differences.

shape of the resonances are very well reproduced. Also the spectral contribution for an energy loss between 90 and 100 eV are present. However, the calculations reveal strong differences above 115 eV. As already found for Ba_8Si_{46} in chapter 7.3 and discussed by Richter *et al.*,[34] the second maximum in the experiment can be attributed to a 4d5p or 4d5s double electron excitation for barium. Since such processes are not included in the RSMS calculation, experiment and FEFF calculations in Fig. 7.9 are normalized to their integral between 101 eV and 111 eV energy loss where these excitations do not significantly contribute. The calculations are smoother than the experiment, which is especially visible in the degree of steepness of the giant resonance onset between 100 and 105 eV. As discussed in chapter 5.3.1, this smoothing of the theoretical curve is probably an artefact due to the finite cluster size within the calculation. The differences between experiment and theory in Fig. 7.10 show that the deficiencies of the calculations are very similar for all compounds. It may be assumed that similar deviations between experiment and theory for different

---

[34] M. Richter *et al.* (1989), *Phys. Rev. A* **39**, 5666.

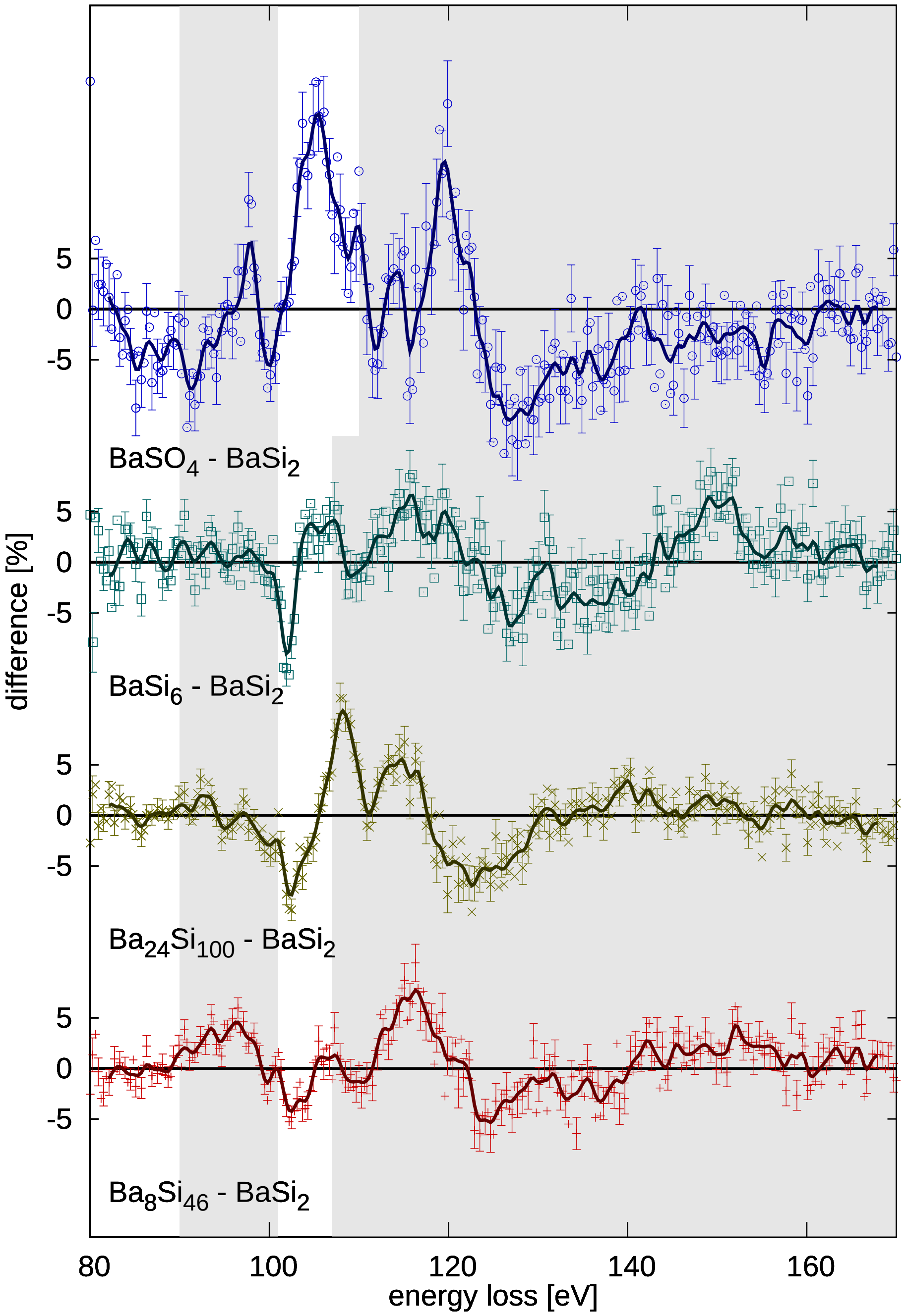

Figure 7.8: Modulation of the giant resonance as presented in Fig. 7.7 after average over q. For the BaSO$_4$ difference, only the result for the lowest q is shown due to the strong momentum–transfer dependence in the energy–loss regime between 90 eV and 100 eV. Smoothened spectra are shown as guides to the eye (solid lines).

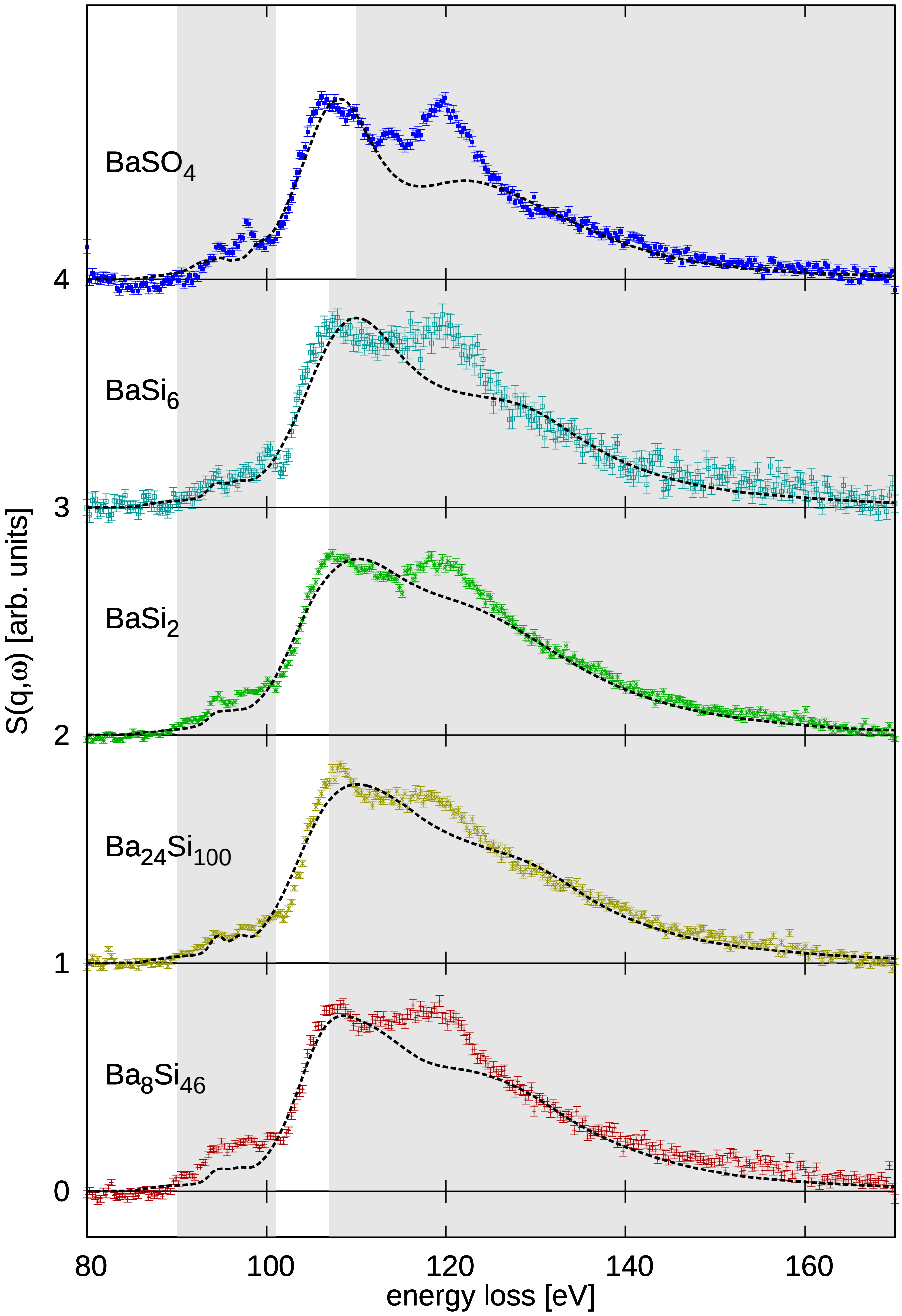

Figure 7.9: Comparison of the experimental giant–resonance spectra (symbols) with RSMS calculations (dashed). Every spectrum is normalized to its area in the interval 101–111 eV. The spectra are vertically shifted for clarity.

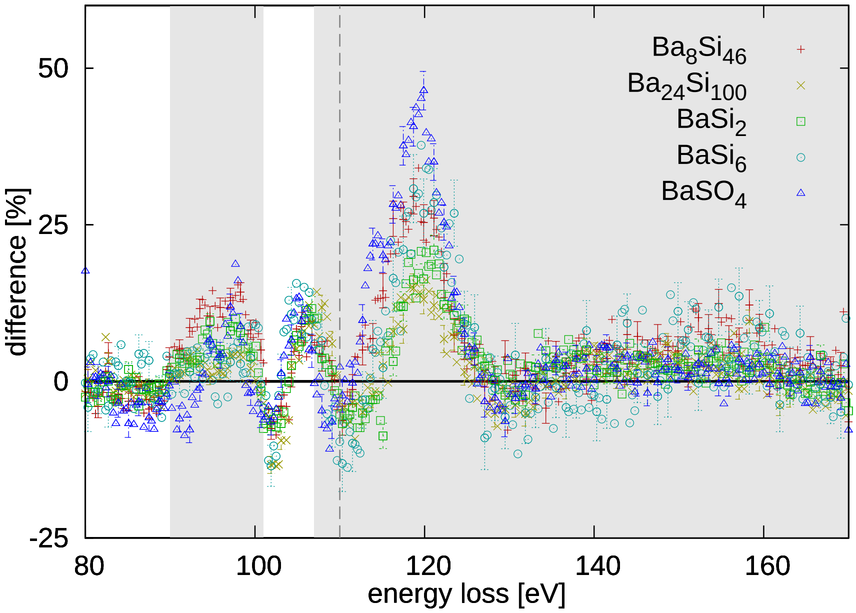

Figure 7.10: Differences between the experiment and the calculation of the giant–resonance spectra as presented in Fig. 7.9. The vertical line indicates the expected onset of the double electron excitations for $BaSO_4$.

compounds indicate that the approximations in the RSMS approach lead to the same deficiencies in the calculations. Thus, the relative changes of the theoretical spectra for those compounds might yield the proper changes of the experimental fine structure. The comparison of calculated and experimental spectral differences between the compounds and the $BaSi_2$ reference presented in Fig. 7.11 indeed shows a reasonable accordance for energy losses below 107 eV (110 eV for $BaSO_4$) and above about 120 eV where the contribution from double electron excitations is suppressed. However, the systematic deviations between experiment and theory (Fig. 7.10) are much stronger than the modulation of the giant resonance expected purely from the experiment (Fig. 7.8). With current state–of–the–art approaches for the calculation of NRIXS spectra, it is difficult to draw definitive conclusions on the electronic differences between the compounds by means of the calculations. A TDLDA implementation for q–dependent calculations of NRIXS spectra and a theoretical consideration of double electron excitations is therefore strongly desirable.

7.4.3 Summary

The barium giant dipole resonance has been measured for various barium–containing compounds. For the first time, theoretically predicted modulations of the giant–resonance spectra for barium in different structural environments could be experimentally verified.

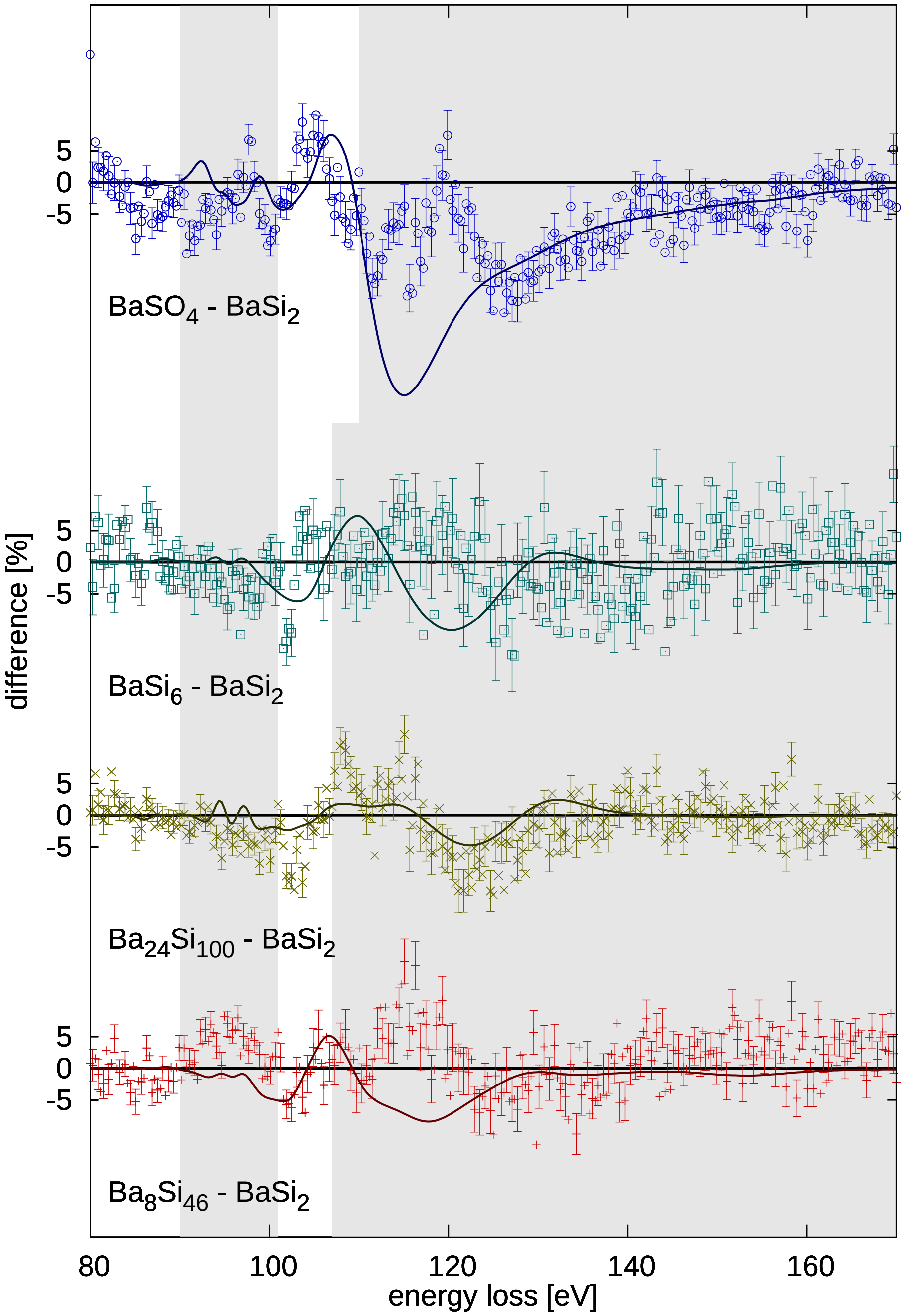

Figure 7.11: Comparison of experimental and calculated differences of the giant resonance with $BaSi_2$ as reference.

Figure 7.12: Mao–Bell diamond–anvil cell used during the high–pressure experiments. The picture shows a one–cent coin for size comparison.

Below the threshold of the resonance, the spectra also show spectral weight with a strong momentum–transfer dependence especially for $BaSO_4$. 6 to 9 eV above the threshold, the resonance is superimposed by a structure originating from double electron excitations. This contribution cannot yet be reproduced with today's computational approaches. However, for the study of one compound under different conditions, e.g. concerning temperature or pressure, it might be expected that systematic errors cancel out when comparing relative changes of the spectra. Therefore, the study of the giant resonance can yield a promising access to local electronic and structural changes in complex compounds.

7.5 High–pressure sample environment

With the focus on the future potential of high–pressure experiments, NRIXS is the only method to study giant resonances under extreme pressure. It is complementary to soft x–ray absorption and electron energy loss spectroscopy since low energy transitions can be measured under experimental conditions in which electrons and soft x–rays are unfeasible as probes. The incident energy can be freely chosen and thus allows the study of shallow absorption edges[35] using hard x–rays of about 10 keV. This yields a high bulk sensitivity and makes high–pressure experiments using, e.g., diamond–anvil cells feasible.[36] Varying the scattering angle, i.e. the momentum transfer q, the spectra can be measured in the dipole limit (low q) or with dominating contributions from non–dipole allowed transitions[37] (high q) as discussed in chapter 2. As long as the dipole approximation is valid, NRIXS

---

[35] Usually between a few eV and 1 keV.

[36] W.L. Mao *et al.* (2003), *Science* **302**, 425; Y. Meng *et al.* (2004), *Nat. Mater.* **3**, 111.

[37] See, e.g., C. Sternemann *et al.* (2003), *Phys. Rev. B* **68**, 035111; H. Sternemann *et al.* (2007*a*), *Phys. Rev. B* **75**, 075118.

spectra measured for energy losses close to a core electron binding energy can be compared with x–ray absorption spectra measured with incident energies in the regime of the binding energy.[38] High–pressure NRIXS studies have been restricted to K–edges of low–Z elements up to now. In the study of heavier elements, the core level cross section is very low. Therefore, the exploration of alternative edges is necessary. It has recently been shown that the barium $N_{IV,V}$–edges in Ba_8Si_{46} are accessible using NRIXS.[39]

Interesting pressure–induced phase transitions in solid state matter usually occur in the range between 1 and 100 GPa. These pressures can be achieved within a *diamond–anvil cell* (DAC).[40] In such a cell, the sample is placed between the coplanar faces of two cut diamond anvils. The diamonds are glued on stainless steel plates, which are connected by screws.[41] When the screws are turned, the metal plates smoothly approach each other and the sample is compressed. To prevent the sample from being squeezed out, it is held between the diamonds by a gasket material such as steel or beryllium. During the experiments presented in this work, the x–ray beam path was chosen through the gasket. Therefore, only beryllium gaskets have been used to reduce absorption.

A gasket has to match the lateral cut of the diamond anvils. Thus, gaskets have to be separately prepared for each cell: A beryllium disc is placed between the diamonds and pre–intended by the diamonds. With a micro drill, the indentation is countersunk so that its hole fits the shape of the diamond facets. The powder sample is loaded into the hole together with a small ruby chip as a pressure calibrant for the standard luminescence method.[42] Fig. 7.12 shows one of the DACs used during the experiment. Due to the small gap between the steel plates, the scattering is strongly shadowed. Hence, this cell only allows the use of one analyzer crystal in the BL12XU multi–analyzer setup as already mentioned in chapter 3.2.2. The count rate can significantly be increased by means of a *panoramic DAC*. Here, the diamonds are rather glued onto steel cones so that the unshadowed opening angle for the scattered beam is much wider.

7.6 Measurement of the barium $N_{IV,V}$–edges in high–pressure environment

Barium/silicon compounds reveal interesting high–pressure properties. Amongst these compounds, the Ba_8Si_{46} clathrate is of special interest for high–pressure studies showing

---

[38] H. Nagasawa *et al.* (1989), *J. Phys. Soc. Jpn.* **58**, 710.

[39] C. Sternemann *et al.* (2005*a*), *Phys. Rev. B* **72**, 035104.

[40] A. Jayaraman (1983), *Rev. Mod. Phys.* **55**, 65.

[41] This is the description of the Mao–Bell DAC which was used in the experiments. An alternative is, e.g., the piston cell in which the diamonds are glued on the two facing sides of a piston and a cylinder.

[42] J.D. Barnett *et al.* (1973), *Rev. Sci. Inst.* **44**, 1.

three phase transitions under hydrostatic pressure. Around 5–7 GPa, Kume *et al.*[43] found a reversible collapse of vibrational Raman modes giving a hint to a second order electronic phase transition. This result is supported by x–ray absorption near edge structure (XANES) measurements of the barium L_{III}–edge by San Miguel *et al.*[44] indicating an energy shift of the edge–onset position. The transition is attributed to a displacement of the barium dopants[45] from the center of the cages, which should also lead to electronic reconfiguration between the barium and the silicon atoms of the host lattice.[46] However, by EXAFS analysis, a maximum displacement of the dopants of 0.3 Å has been estimated.[47] Between 11.5 and 14 GPa San Miguel *et al.*[48] observed a drastic reduction of the lattice constant by x–ray diffraction (XRD) whereas the diffraction pattern shows no change in the crystal symmetries. The mechanism of this isostructural volume collapse is not fully understood. Whereas Yang *et al.*[49] predict a dramatic Fermi surface change in the region of the volume collapse by employing band–structure calculations, Iitaka,[50] instead, proposed that some of the silicon atoms are released from the silicon network by pressure leading to vacancies and thus to an increased compressibility without a change of the space group visible for XRD. Finally, above 40 GPa, Ba_8Si_{46} becomes irreversely amorphous.[51] In order to determine the mechanism of the phase transitions, a study of the changes in the local environment and the electronic structure of the guest atom is required. The sensitivity of the barium giant resonance to the surrounding of the barium atom was demonstrated in chapter 7.4. Thus, it seems to be a promising approach to study pressure–induced phase transitions by means of the fine structure of the giant resonance. It has also been shown that current numerical approaches feature deficiencies in the calculation of giant–resonance spectra for different compounds. However, it can be assumed that the deviations of calculations at different pressures for the same compound are very similar so that the relative changes of the spectra are reproduced correctly. Therefore, TDLDA calculations of Ba_8Si_{46} have been performed in the same way as for ambient pressure. The structure was assumed to be unchanged apart from the lattice constant which was chosen according to San Miguel *et al.*[52] The results of the calculations are displayed in the right part of Fig. 7.13.

The high–pressure experiment was accomplished at SPring–8 beamline BL12XU. For the details of the experimental setup, it is referred to chapter 3.2.2. The Ba_8Si_{46} powder

---

[43] T. Kume *et al.* (2003), *Phys. Rev. Lett.* **90**, 155503.

[44] A. San Miguel *et al.* (2005), *Europhys. Lett.* **69**, 556.

[45] T. Kume *et al.* (2003), *Phys. Rev. Lett.* **90**, 155503; L. Yang *et al.* (2006), *Phys. Rev. B* **74**, 245209.

[46] A. San Miguel *et al.* (2005), *Europhys. Lett.* **69**, 556.

[47] ibid.

[48] ibid.

[49] L. Yang *et al.* (2006), *Phys. Rev. B* **74**, 245209.

[50] T. Iitaka (2007), *Phys. Rev. B* **75**, 012106.

[51] A. San Miguel and P. Toulemonde (2005), *High Pressure Res.* **25**, 159.

[52] Lattice constant from A. San Miguel *et al.* (2005), *Europhys. Lett.* **69**, 556, Fig. 2: ambient pressure: 10.36 Å, 8 GPa: 10.1 Å, 20 GPa: 9.6 Å.

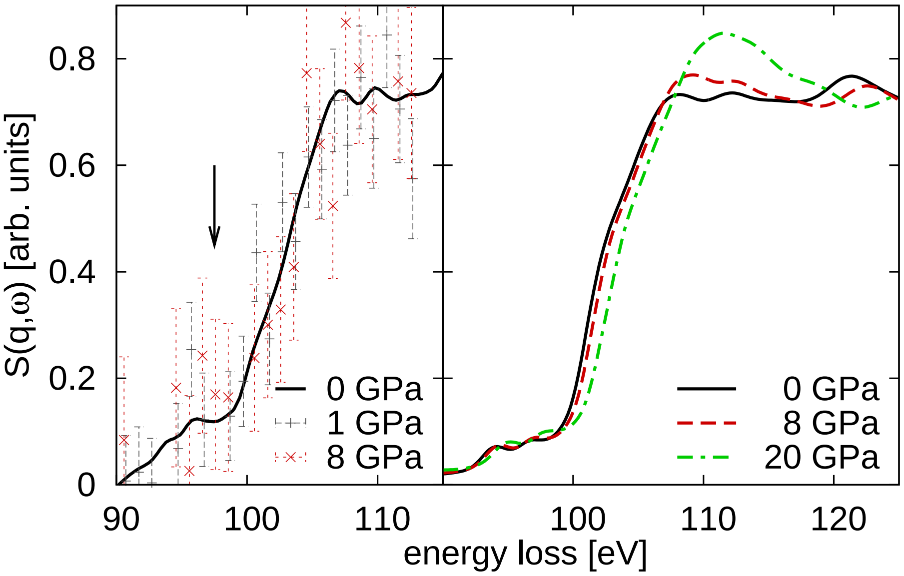

Figure 7.13: Experiment and calculations for the high–pressure experiment of Ba_8Si_{46}. Left: Comparison of the measured barium giant resonance onset in Ba_8Si_{46} at $q = 1.29$ a.u. for ambient pressure (solid line), 1 GPa and 8 GPa. Right: Calculated XAS spectra using TDLDA (ANR) at ambient pressure, 8 and 20 GPa. All spectra are normalized to the area between 90 and 115 eV. The arrow indicates the energy loss regime of 4d → d monopole excitations as predicted within LDA calculations employing FEFF8.2. Both, experiment and calculations, include the contributions from the silicon $L_{II,III}$–edges.

was loaded into a drilled hole of 125 μm diameter in a pre–intended 100 μm thick beryllium gasket together with a ruby chip as a pressure calibrant for the standard luminescence method. This gasket was placed between the cut–end face of the diamonds within the DAC. The beam path was chosen through the beryllium gasket, and a tungsten slit of $50 \times 500\,\mu\mathrm{m}^2$ mounted in front of the analyzer arm was brought close to the gasket to reduce scattering from beryllium.[53] Pressures of 1 and 8 GPa were applied and the barium giant resonance was measured in transmission geometry at a scattering angle of 20° ($q =$ 1.29 a.u.). All measured spectra were normalized with a monitor signal and corrected for the background, absorption and scattering cross section according to chapter 4.2.1. The experimental parameters are summarized in Tab. A.2 (key C_3). The results presented in Fig. 7.13 show the first NRIXS measurements of non–K edges under high–pressure conditions. The comparison between these spectra at 1 and 8 GPa with the results for ambient pressure emphasizes that the signal from the Ba_8Si_{46} can be properly extracted when measured in a DAC. These spectra are confronted with the calculations of the giant resonance at pressures of 1, 8, and 20 GPa. Within the actual accuracy of the experiment, it was not possible to subtract the silicon contribution from the spectrum by a reference so

---

[53] The onset of the beryllium K–edge is at 111.5 eV energy loss.

that both, experiment and calculations, include the silicon $L_{II,III}$–edges. It is also difficult to judge whether an increase of spectral weight for 4d → d excitations around energy losses of 98 eV at high pressure can be observed. This change is due to an increase of filled and empty d–bands near the Fermi level across the phase transition at 7 GPa, which was discussed by San Miguel *et al.* and Yang *et al.*[54] A conclusion on the pressure–induced changes of the giant resonance's shape as predicted by theory for energy losses above 107 eV cannot be drawn within the limits of the experiment. Nevertheless, the statistics and the signal–to–noise ratio of the high–pressure signal can be significantly improved by using special DACs optimized for the use with a multianalyzer setup together with different gasket material so that detailed differences between the spectra become observable. The new Medipix setup at ESRF beamline ID16 is a predestinated setup for such high–pressure experiments. Besides nine available analyzers, the signal from the sample can be separated from the gasket scattering by software slitting due to the spatial resolution of the setup.[55] Such experiments allow the study of giant resonances under high–pressure conditions, which opens a large field of applications concerning the structural and electronic pressure–dependence for a wide range of materials. The feasibility of this NRIXS application was demonstrated by the results presented in this chapter.

7.7 The iodine giant resonance in $I_8Si_{44}I_2$

Besides the elements with $Z \geq 55$, such as barium or lanthanum, for which a collapse of the 4f–orbitals causes an enhancement of the spectral contribution above the $N_{IV,V}$–threshold, also elements with $Z \leq 54$ show giant resonances[56] in a two–well potential of the atomic centrifugal barrier.[57] Iodine is of special interest due to its different electronegativity compared to barium. Connerade and Mansfield[58] show that the charge of the resonating atom strongly influences orbital hybridization. A DFT ab–initio study of silicon clathrates exhibits that dopants with elements of higher electronegativity than silicon can tune mechanical and physical properties over a broad range.[59] Like barium, also iodine can be inserted into complex silicon networks. $I_8Si_{44}I_2$ is a structure similar to the Ba_8Si_{46} clathrate. An iodine atom is trapped in each of the eight silicon cages in the unit cell and, in addition to that, two silicon atoms of the host–cage structure are replaced by iodine atoms. This leads to a certain distortion of the regular type I clathrate structure. An

---

[54] A. San Miguel *et al.* (2005), *Europhys. Lett.* **69**, 556; L. Yang *et al.* (2006), *Phys. Rev. B* **74**, 245209.

[55] See chapter 3.2.1 for details of the setup.

[56] As is the case for xenon (R. Haensel *et al.* (1969), *Phys. Rev.* **188**, 1375) or iodine (A.T. Domondon and X.M. Tong (2002), *Phys. Rev. A* **65**, 032718).

[57] U. Becker (1987), "The 4d + 4f giant resonance from barium through the rare–earths", *Giant Resonances in Atoms, Molecules, and Solids*, Plenum, New York.

[58] J.P. Connerade and M.W.D. Mansfield (1982), *Phys. Rev. Lett.* **48**, 131.

[59] D. Connétable (2007), *Phys. Rev. B* **75**, 125202.

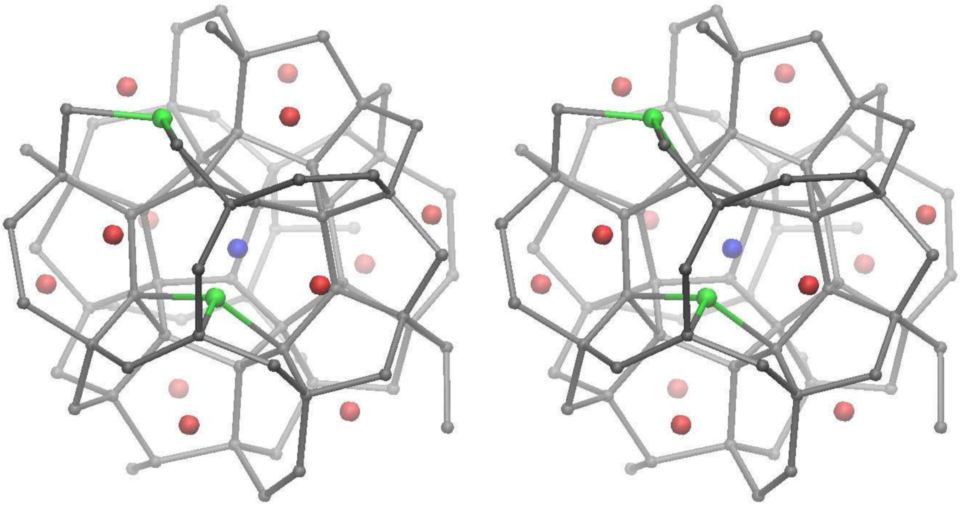

Figure 7.14: Stereoscopic images (parallel) of the $I_8Si_{44}I_2$ structure. Iodine atoms occupying the two different cages are colored blue and red, iodine atoms replacing silicon in the network are colored green.

illustration of the atomic structure is given in Fig. 7.14.

NRIXS spectra for $I_8Si_{44}I_2$ have been recorded at SPring–8 beamline BL12XU and ESRF beamline ID16 for low and high momentum transfers.[60] As typical for a giant dipole resonance, the spectrum for low q is dominated by a broad structure above the $N_{IV,V}$–threshold. As shown in Fig. 7.15, the RSMS calculation within TDLDA shows a generally good agreement with the experiment. For high momentum transfer, q–dependent RSMS calculations were performed within LDA and are compared with the experiment in Fig. 7.16. The modulations of the spectrum between 50 and 70 eV and the silicon $L_{II,III}$–edges are remarkably well described by the calculations. However, the spectral weight between 70 and 100 eV is significantly underestimated by the LDA calculations. For small q, dynamical effects can be the cause for this enhancement since this region coincides with the maximum of the giant resonance. They, however, are not included in the q–dependent RSMS calculations. The strong momentum–transfer dependence of the $I_8Si_{44}I_2$ NRIXS spectrum becomes even clearer in Fig. 7.17 showing results obtained with the Medipix setup at ESRF ID16. Here, the silicon contribution was removed so that the spectra only show the signal from the iodine. For low q, the spectra are compared with the iodine contribution of the TDLDA calculation presented in Fig. 7.15. The good agreement emphasizes the high quality of the background subtraction. In analogy to Fig. 7.16, q–dependent RSMS calculations were also performed for $q = 4.60\,\text{a.u.}$ and are compared with the experiment. The agreement is in line with the results obtained for $q = 6.98\,\text{a.u.}$ The increase of the first

---

[60] For experimental details see Tab. A.2 (keys D_n and E_n).

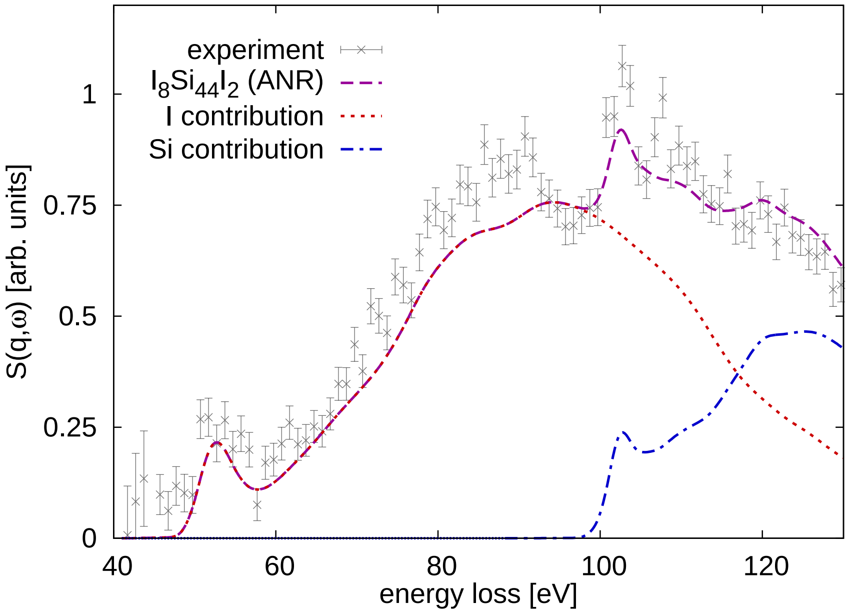

Figure 7.15: NRIXS spectrum for $I_8Si_{44}I_2$ at $q = 0.69$ a.u. The dipole RSMS calculations employing TDLDA are included for comparison.

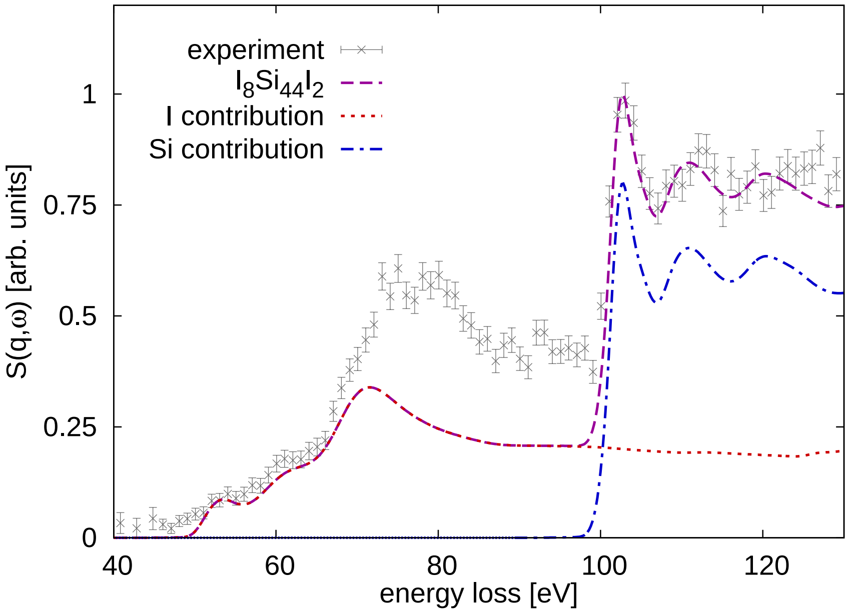

Figure 7.16: NRIXS spectrum for $I_8Si_{44}I_2$ at $q = 6.98$ a.u. The spectra are compared with the q–dependent RSMS calculations within LDA.

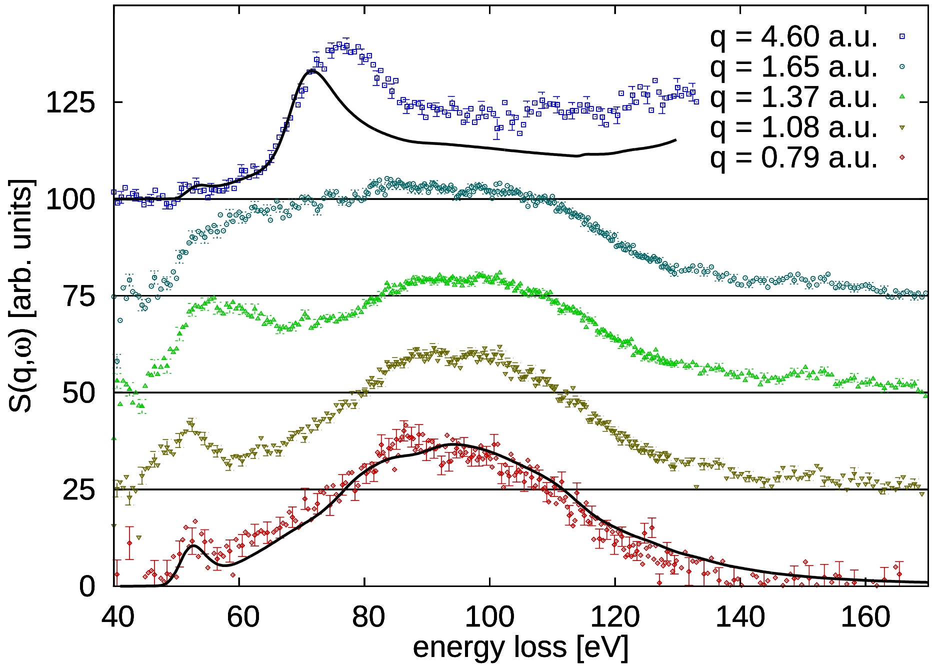

Figure 7.17: Momentum–transfer dependence of the iodine $N_{IV,V}$–spectrum. The RSMS calculation within TDLDA in the dipole limit is compared with the results for $q = 0.79$ a.u. The q–dependent RSMS calculation in LDA is compared with the experiment for $q = 4.60$ a.u. The spectra are vertically shifted for clarity.

maximum around 40–60 eV is the most striking change for growing momentum transfer in the experiment. This indicates the rise of multipole contributions to the NRIXS spectrum. A TDLDA enhancement for the q–dependent RSMS implementation is therefore again highly desirable to understand the q–dependence of giant–resonance spectra.

7.8 Conclusions and outlook

The $4\mathsf{d}-\mathsf{f}$ giant dipole resonance of barium was studied for various complex silicon compounds with intercalated barium atoms by means of NRIXS. It has been shown for the first time that theoretically predicted fingerprint–like modulations of the resonance in such compounds exist and can be measured with sufficient precision for a direct comparison. By means of the ab–initio real space multiple scattering approach FEFF, the giant resonances could be modeled successfully within TDLDA. The comparison with the experiment exhibits that double electron excitations superimpose the resonance, which are not included in the RSMS calculations. Nevertheless, the comparison of relative changes of the resonance for different compounds shows good agreement between experiment and calculations for the energy ranges where double electron excitations do not contribute. Moreover, these results indicate that the study of changes in the giant resonance for a compound under variation of experimental parameters, like temperature or pressure, might be successfully describable within the current RSMS approach. However, for a comparison of the full spectra, double electron excitations and non–dipole contributions have to be taken into account.

The onset of the giant resonance in the vicinity of the barium $N_{IV,V}$–edges in Ba_8Si_{46} was also measured under high–pressure conditions. Though the statistics of the first experiment are not sufficient to draw further conclusions on pressure–dependent changes in the system, the shape of the resonance onset for ambient–pressure conditions could be well reproduced. In the view of the gain in counting rate and background discrimination with the new Medipix setup of ESRF ID16, this opens a wide field of novel applications for high pressure NRIXS studies on medium– and high–Z elements. Measurements of the barium giant resonance as a function of pressure by NRIXS yield enormous potential for a combined probe of changes in the electronic and local structure across phase transitions. This method can be applied in general for high–pressure studies for a wide range of nanostructured materials with resonating guest atoms caged in, e.g., clathrates or fullerenes.

Finally, the $N_{IV,V}$–edges of iodine in the $I_8Si_{44}I_2$ clathrate structure were studied as an example of an intercalated resonator with different electronegativity. A complex momentum–transfer dependence was experimentally observed. The spectrum for low q could be explained by RSMS calculations within TDLDA, whereas the q–dependent calculation within LDA for high momentum transfer lacks spectral weight compared to the experiment. This finding also stresses the need for a TDLDA implementation in the RSMS approach for NRIXS.

Chapter 8

Summary and outlook

8.1 Summary

In this thesis, silicon compounds of industrial and fundamental interest have been studied by means of inelastic x–ray scattering. The major achievements of this thesis are: the development of a universal background–subtraction algorithm necessary for advanced q–dependent NRIXS studies, the exploration of L–edge studies by an RSMS approach, the experimental extraction of suboxide spectra combined with a study of the disproportionation in bulk amorphous silicon monoxide, and the experimental proof of theoretically predicted modulations in the barium giant dipole resonance by means of NRIXS.

An experimentally self–consistent background removal algorithm was developed for momentum–transfer dependent NRIXS studies. Apart from tabulated Hartree–Fock core Compton profiles, no theoretical input is necessary to distill the absorption edges of interest for a wide energy– and momentum–transfer range from the scattering of other electrons in the system. The quality of the algorithm was demonstrated on the silicon L–edges in Si and SiO_2. The results show very good agreement with momentum–transfer dependent ab–initio calculations.

The performance and limitations of an RSMS approach for the calculation of q–dependent NRIXS spectra were discussed for the near–edge regime of sodium, magnesium and silicon L–edges. The general shape and most of the fine structure in the calculations show very good agreement with experiment and calculations within an approach based on the Bethe–Salpeter equations. Deviations between experiment and theory were discussed referring to approximations in the RSMS approach, e.g. concerning finite–size effects and the core–hole treatment. In general, the RSMS approach was found to well explain the experimental data, so that it is a good alternative for systems for which calculations employing different approaches, like the BSE, are unfeasible.

The disproportionation of bulk amorphous silicon monoxide was studied by NRIXS. The decrease of the suboxide interface domain due to the phase separation of local Si and SiO_2 regimes could be observed in the spectra for different annealing temperatures and momentum transfers. The results yield a consistent overall picture in line with the ICM model. The temperature range for the disproportionation could be determined and was compared with results of an analogous RIXS experiment on the disproportionation of bulk amorphous germanium monoxide. For the first time, the spectral contributions of the suboxides to the silicon $L_{II,III}$–edges could be extracted directly from the NRIXS signal. A comparison with an ab–initio calculation based on the StoBe–deMon code yields a good general agreement.

The barium giant dipole resonance was studied for barium atoms in complex surroundings, especially in complex silicon network structures, by means of NRIXS. The momentum–transfer dependence of the barium $N_{IV,V}$–edges was analyzed showing the strong suppression of the resonance for large momentum transfer. For the first time, theoretically predicted modulations of the barium giant resonance spectrum for different local surroundings could be experimentally verified. The modulations were compared to ab–initio RSMS calculations in the dipole limit employing TDLDA. Deviations between experiment and theory could be explained by multi–electron excitations and multipole contributions, which are not accounted for in the calculations. The importance of the giant resonance for the study of pressure–induced phase transitions was emphasized and the feasibility of this approach was shown in a first experiment. The iodine giant resonance was studied for iodine atoms in a type I silicon clathrate and a complex momentum–transfer dependence was experimentally found, which in part could be explained by dipole and q–dependent RSMS calculations.

The thesis advances the experimental treatment of q–dependent NRIXS studies as well as the interpretation of experimental results when comparing to ab–initio calculations in general. On the basis of these results, the thesis contributes to the understanding of the physics in two important material classes: amorphous silicon oxides and silicon clathrates.

8.2 Outlook

With the installation of NRIXS spectrometers designated for multi–q experiments, as the LERIX setup at APS beamline 20–ID or the multi–analyzer setups at ESRF beamline ID16 and the Taiwan beamline BL12XU at SPring–8, the number of momentum–transfer dependence studies is increasingly growing. The algorithm for background subtraction developed in this thesis now allows a consistent analysis of the experimental data. The access of core excitations and the possible extraction of the projected density of states from multi–q NRIXS spectra opens a wide field of applications for a combined electronic and structural study of complex bulk systems.

The comparison of the novel RSMS approach for NRIXS spectra with the experiment and with BSE calculations supports the applicability of this approach to systems, which are not accessible with other computational methods. These are especially materials in the focus of current research, such as amorphous materials and systems with large unit cells.

The results from the NRIXS study of the disproportionation of bulk amorphous silicon monoxide encourage further experiments for a finer grid of annealing temperatures to increase the accuracy of the temperature regimes. In order to determine the minimum possible amount of suboxides in the silicon monoxide, i.e. the state of full disproportionation, a study for annealing temperatures higher than 1000 ℃ is required. The agreement of the results for silicon and germanium monoxide gives rise to future studies on ternary $\mathrm{Si}_x\mathrm{Ge}_y\mathrm{O}_z$ compounds. These materials are of special industrial importance concerning faster metal oxide semiconductor field effect transistors on Si/Ge alloys. The study of silicon/silicon oxide interfaces is crucial since they can have a significant influence on the quality of nanoelectronic devices. The successful experimental extraction of the spectral contribution of silicon suboxides exhibits an access to the local electronic structure. The agreement with first ab–initio calculations asks for calculations on larger suboxide clusters for the refinement of structural models for the suboxides.

The experimental evidence found for the modulations in the barium giant dipole resonance yields a promising approach to the study of pressure– or temperature–induced phase transitions. Since in such experiments, spectral changes are observed for the same compound, it might be assumed that already with the present theoretical approaches an interpretation of relative changes in the spectra could be possible. The complex momentum–transfer dependence of the iodine giant resonance requires further theoretical calculations. With an appropriate theoretical framework this q–dependent study is promising to give insight into the coupling of guest atoms to the host lattice and on angular momentum resolved hybridization. These results once more emphasize the need for advanced theoretical approaches, for instance a TDLDA implementation for the RSMS approach of NRIXS.

Appendix A

Supplement to chapter 3

NRIXS experiments have been carried out with four different setups at three beamlines as listed in Fig. A.1.

Setup	Facility	Beamline	Description	Chapter
a	ESRF	ID16	single–detector Rowland setup	3.2.1
b	APS	20–ID	multi–detector LERIX setup	3.2.3
c	SPring–8	BL12XU	high–pressure Rowland setup	3.2.2
d	ESRF	ID16	multi–detector Medipix setup	3.2.1

Table A.1: Setups of the NRIXS experiments presented in this work.

The important experimental parameters for all spectra measured with these setups and presented in this work are summarized in table A.2. The spectra are referenced by the letter given in the first column of the table. For a detailed description of the setups, it is referred to the according chapter.

	Key	ϕ [°]	q [a.u.]	E_0 [keV]	ΔE [eV]	$V\times H$ [μm^2]	Setup
Si	A_1	26.0	1.50	12.398	0.8	50×120	*a*
	A_2	150.0	6.42	12.398	1.5	50×120	*a*
Mg	A_3	13.3	0.61	9.886	1.5	1500×1500	*a*
	A_4	150.0	6.42	12.398	0.8	50×120	*a*
Na	A_5	14.0	0.65	9.886	1.5	70×120	*a*
	A_6	160.0	5.22	9.886	1.5	70×120	*a*
Si, SiO_2, SiO (nat.), SiO (800°), SiO (1000°)	B_1	9.0	0.42	9.893	1.5	400×100	*b*
	B_2	18.0	0.84	9.893	1.5	400×100	*b*
	B_3	27.0	1.25	9.893	1.5	400×100	*b*
	B_4	36.0	1.66	9.893	1.5	400×100	*b*
	B_5	45.0	2.05	9.893	1.5	400×100	*b*
	B_6	54.0	2.43	9.893	1.5	400×100	*b*
	B_7	63.0	2.80	9.893	1.5	400×100	*b*
	B_8	72.0	3.15	9.893	1.5	400×100	*b*
	B_9	81.0	3.48	9.893	1.5	400×100	*b*
	B_{10}	90.0	3.79	9.893	1.5	400×100	*b*
	B_{11}	99.0	4.08	9.893	1.5	400×100	*b*
	B_{12}	108.0	4.34	9.893	1.5	400×100	*b*
	B_{13}	117.0	4.57	9.893	1.5	400×100	*b*
	B_{14}	126.0	4.78	9.893	1.5	400×100	*b*
	B_{15}	135.0	4.95	9.893	1.5	400×100	*b*
	B_{16}	144.0	5.10	9.893	1.5	400×100	*b*
	B_{17}	153.0	5.21	9.893	1.5	400×100	*b*
	B_{18}	162.0	5.29	9.893	1.5	400×100	*b*
	B_{19}	171.0	5.34	9.893	1.5	400×100	*b*
Ba_8Si_{46}	C_1	26.0	1.50	12.398	1.6	50×100	*a*
	C_2	150.0	6.42	12.398	1.6	50×100	*a*
	C_3	20.0	1.29	13.854	2.0	20×25	*c*
$I_8Si_{44}I_2$	D_1	10.0	0.69	13.854	2.0	20×25	*c*
	D_2	140.0	6.98	13.854	2.0	20×25	*c*
$I_8Si_{44}I_2$	E_1	111.5	4.29	9.687	1.1	50×100	*d*
	E_2	118.0	4.45	9.687	1.1	50×100	*d*
	E_3	124.5	4.60	9.687	1.1	50×100	*d*
	E_4	131.0	4.73	9.687	1.1	50×100	*d*
	E_5	137.5	4.84	9.687	1.1	50×100	*d*
Ba_8Si_{46}, $Ba_{24}Si_{100}$, $BaSi_6$, $BaSi_2$, $BaSO_4$, Si, Si_{136}, $I_8Si_{44}I_2$	F_1	17.5	0.79	9.687	1.1	50×100	*d*
	F_2	24.0	1.08	9.687	1.1	50×100	*d*
	F_3	30.5	1.37	9.687	1.1	50×100	*d*
	F_4	37.0	1.65	9.687	1.1	50×100	*d*
	F_5	43.5	1.93	9.687	1.1	50×100	*d*

Table A.2: Experimental parameters of all NRIXS spectra presented in this work. ϕ is the scattering angle, q the absolute value of the momentum transfer. E_0 is the analyzer energy, ΔE the corresponding total energy resolution. V and H are the vertical and horizontal beam sizes. The setups used for the according experiments are indicated in the last column referring to table A.1.

Appendix B

Supplement to chapter 5

The decomposition with respect to the angular momentum of the final state is shown in Fig. B.1 for the RSMS calculation of silicon presented in chapter 5.3.1 (see Fig. 5.1). As expected by the excitation operator $e^{i\mathbf{q}\cdot\mathbf{r}}$, dipole $\mathsf{p} \rightarrow \mathsf{d}$ processes dominate the spectrum for low momentum transfer whereas the contribution of the monopole transition $\mathsf{p} \rightarrow \mathsf{p}$ is significantly increased for $q = 6.42$ a.u.

For sodium, decompositions of the $\mathrm{L}_{\mathrm{II,III}}$–edges were calculated both for local Hedin–Lundqvist exchange and for partially non–local exchange and are presented in Figs. B.2 and B.3. As discussed in chapter 5.3.3, in the latter case, the exchange contributions are calculated within Dirac–Fock for the core electrons and within Hedin–Lundqvist self–energy for the valence electrons. Unlike the FEFF standard configuration $2\mathsf{p}^6 3\mathsf{s}^1$ for the valence electrons within the calculations shown in Fig. B.2, only the $3\mathsf{s}^1$ electron was treated as a valence electron. It can be seen in Fig. 5.5 that such a treatment leads to better agreement with the experiment especially for small momentum transfer. A possible explanation for this effect is given in chapter 5.3.3.

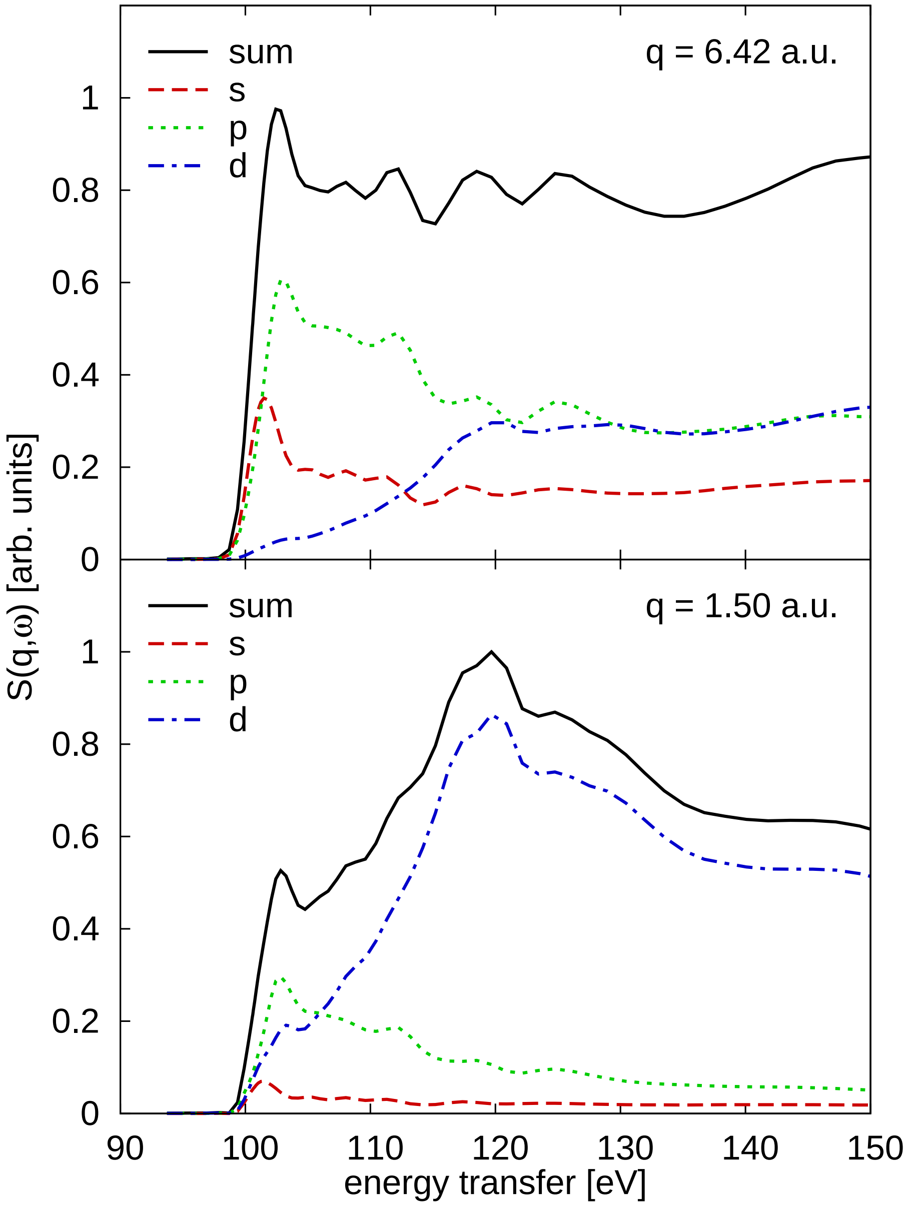

Figure B.1: Decomposition of the RSMS calculations of the Si $L_{II,III}$–edges at $q = 1.50$ a.u. (bottom) and $q = 6.42$ a.u. (top) with respect to the angular momentum of the final state.

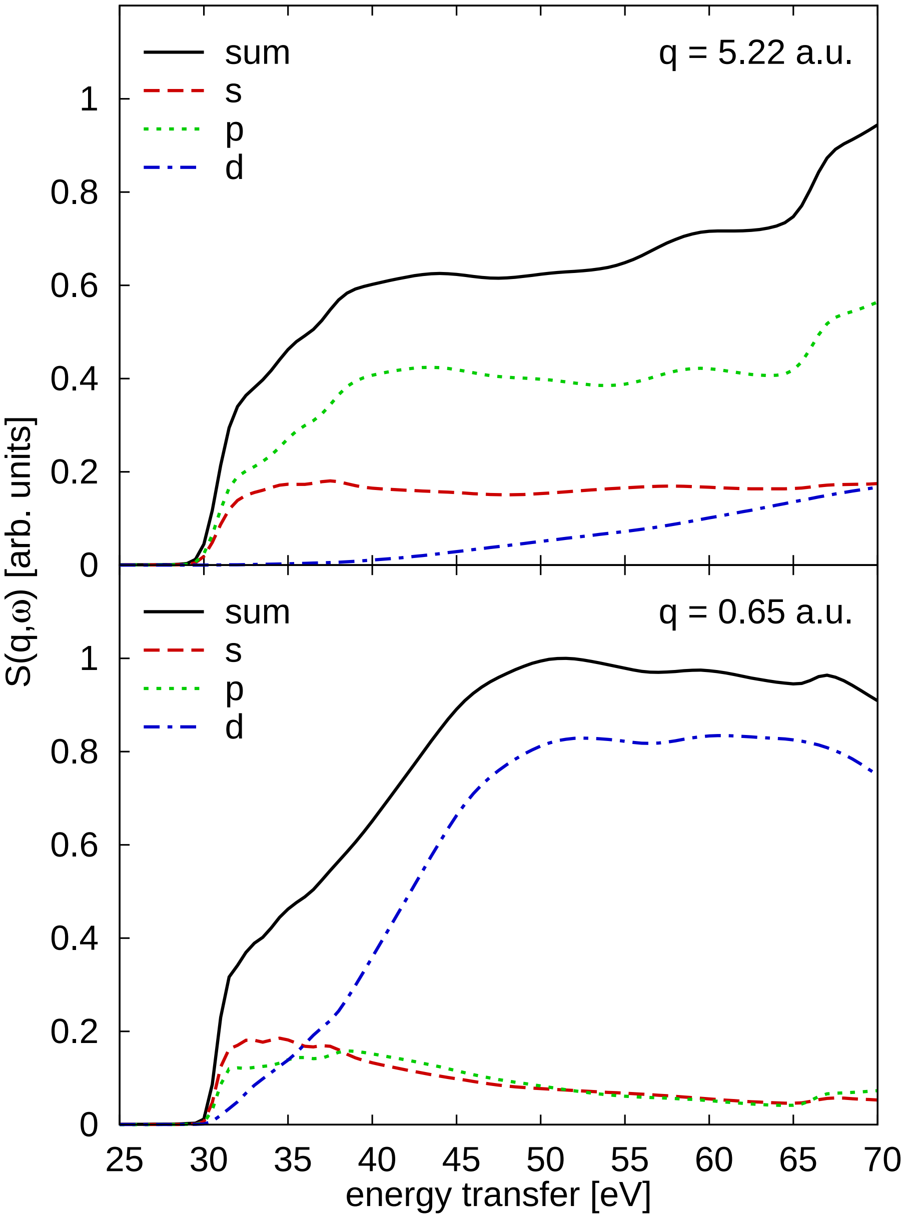

Figure B.2: Decomposition of the RSMS calculations of the Na $L_{II,III}$–edges at $q = 0.65$ a.u. (bottom) and $q = 5.22$ a.u. (top) with respect to the angular momentum of the final state.

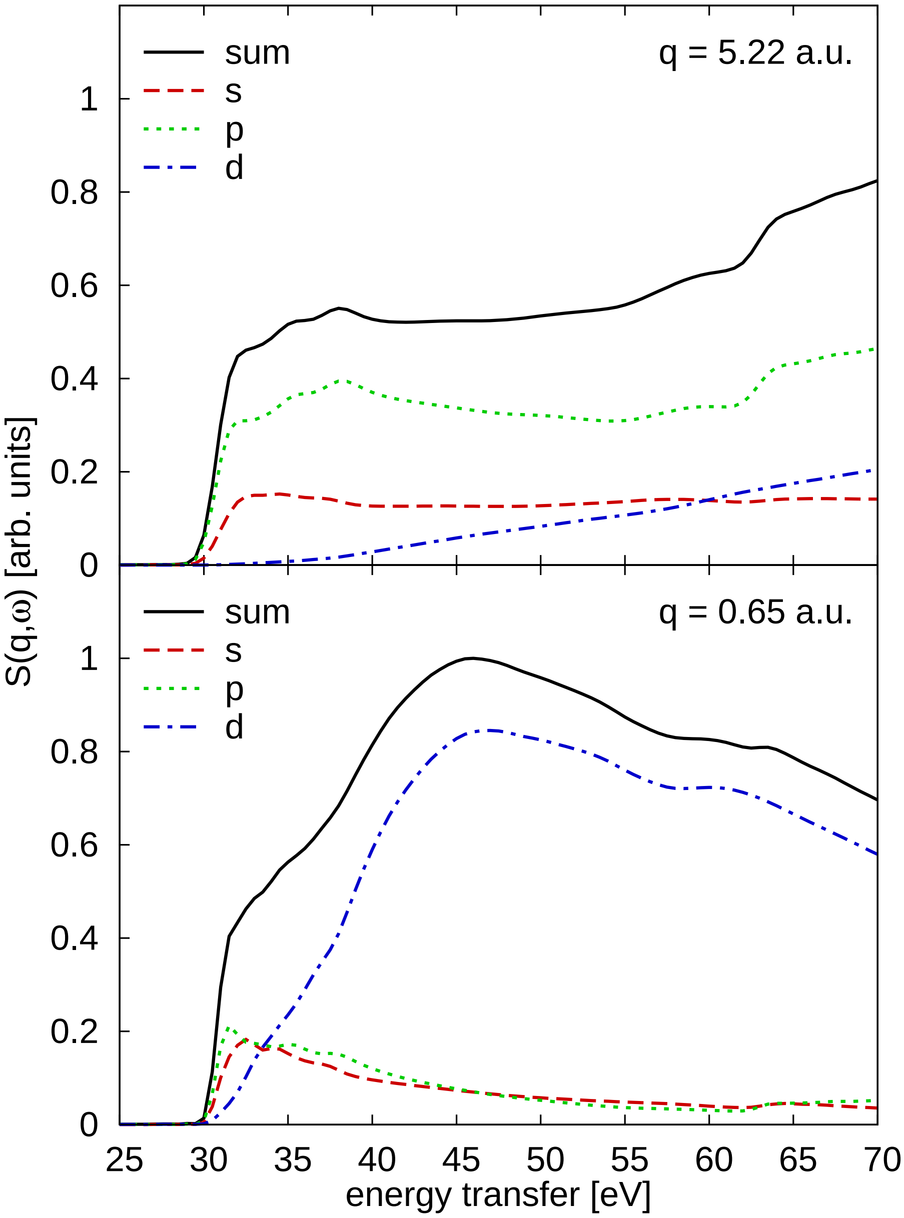

Figure B.3: Decomposition of the RSMS calculations of the Na $L_{II,III}$–edges as in Fig. B.2 but with non–local exchange.

Appendix C

Supplement to chapter 7

C.1 X–ray diffraction of the complex barium/silicon compounds

Diffraction patterns of the complex barium/silicon compounds were recorded at ESRF beamline ID 15 (Ba_8Si_{46} and $Ba_{24}Si_{100}$) at $E_0 = 70$ keV and at DELTA BL9/SAW ($BaSi_6$) at $E_0 = 27$ keV by means of a 2D image plate detector[1] to verify the good powder quality and purity of the samples. All diffraction patterns show uniform Debye rings with little texture. The patterns have been circularly integrated and are presented in Figs. C.1–C.3. The calculations have been performed with the program POUDRIX.[2]

Due to the small amount of sample, the $BaSi_6$ sample was kept inside a sample tube of partially crystallized polymer during the diffraction experiment. The diffraction from the tube dominates the pattern for $q < 0.9$ a.u., thus in Fig. C.3 it is only shown for $q \geq 0.9$ a.u.

C.2 Input files for ATOMS

For RSMS calculations with the FEFF program, the cartesian coordinates of atoms in a finite atomic cluster are required as input parameters. The atomic position for crystals can be calculated with the program ATOMS.[3] The ATOMS input files for the corresponding FEFF calculations presented in chapter 7 are given in tables C.1–C.7.

---

[1] mar345 image plate detector (Marresearch GmbH)

[2] J. Laugier and B. Bochu (2001), *POUDRIX V2*, Laboratoire des matériaux et du génie physique, 2001, URL: `http://www.lmgp.inpg.fr`.

[3] Bruce Ravel (1998), *ATOMS 2.50*, University of Washington / ANL, 1998, URL: `cars9.uchicago.edu/~ravel`.

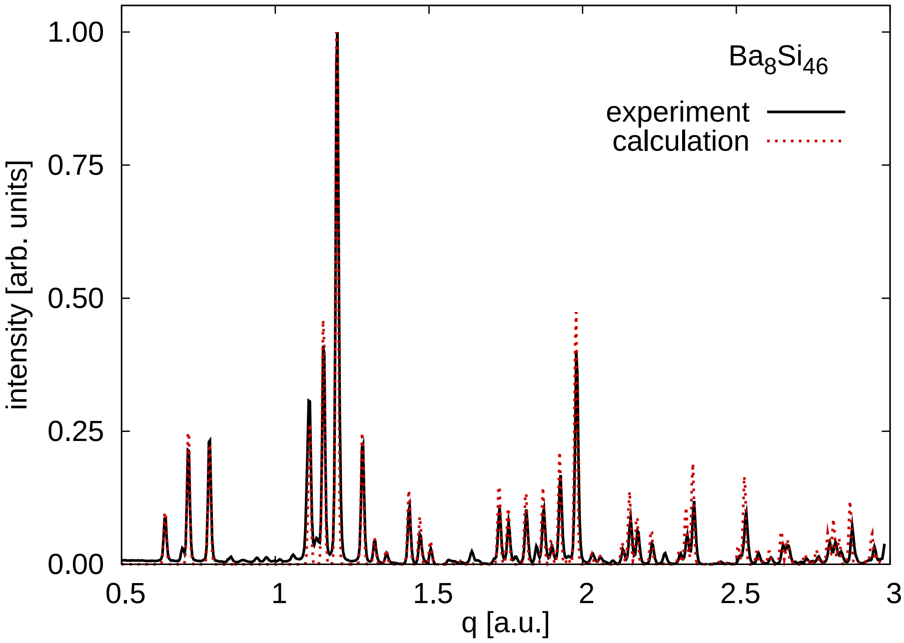

Figure C.1: XRD of Ba$_8$Si$_{46}$. $E_0 = 70$ keV. The theoretical spectrum shows very good agreement with the experiment.

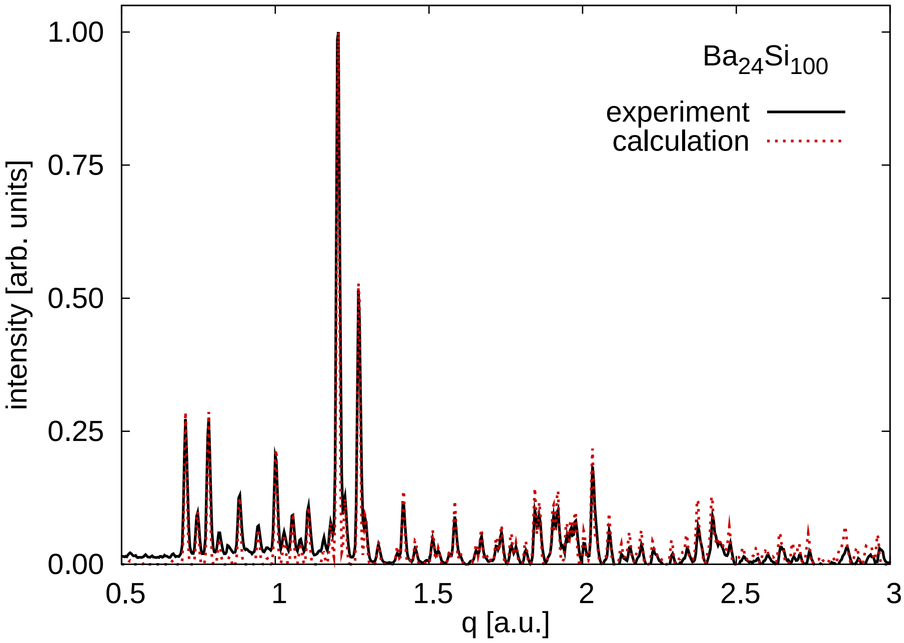

Figure C.2: XRD of Ba$_{24}$Si$_{100}$. $E_0 = 70$ keV. The agreement between theory and experiment is comparable to Fig. C.1.

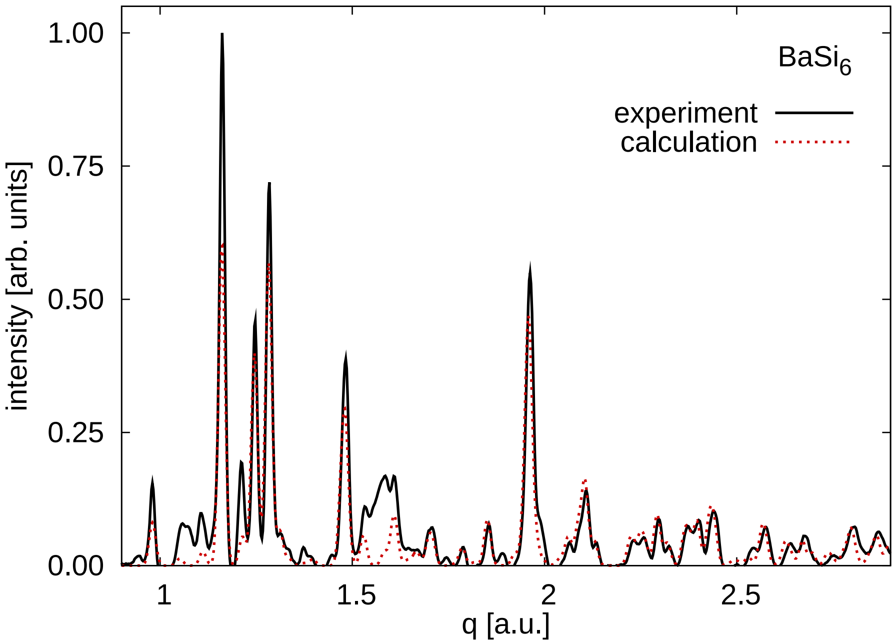

Figure C.3: XRD of BaSi$_6$. $E_0 = 27$ keV. The agreement between theory and experiment is reasonably good. The additional contributions in the diffraction pattern are probably due to the polymer sample tube.

```
title BaSi2 I (orthorhombic)

space P n m a
rmax=20 a 8.920 b 6.750 c 11.570
core=Ba0
edge=N4

output BaSi_I_feff.inp

atoms
   Ba    0.014    0.250    0.694    Ba0
   Ba    0.893    0.250    0.095    Ba1
   Si    0.424    0.250    0.091    Si0
   Si    0.205    0.250    0.969    Si1
   Si    0.190    0.078    0.147    Si2
```

Table C.1: ATOMS 2.50 input file for the orthorhombic BaSi$_2$ structure.

```
title BaSi6

space C m c m
rmax=20 a 4.485 b 10.375 c 11.969
core=Ba0
edge=N4

output BaSi6_feff.inp

atoms
   Ba    0.000    0.273    0.250    Ba0
   Si    0.000    0.250    0.537    Si0
   Si    0.000    0.559    0.351    Si1
   Si    0.000    0.024    0.599    Si2
```

Table C.2: ATOMS 2.50 input file for the $BaSi_6$ structure.

```
title Ba8Si46

space P m -3 n
rmax=18 a 10.35
core=Ba0
edge=N4

output Ba8Si46_feff.inp

atoms
   Si    0.2500   0.5000   0.0000   Si0
   Si    0.1837   0.1837   0.1837   Si1
   Si    0.0000   0.1170   0.3080   Si2
   Ba    0.0000   0.0000   0.0000   Ba0
   Ba    0.2500   0.0000   0.5000   Ba1
```

Table C.3: ATOMS 2.50 input file for the Ba_8Si_{46} structure.

```
title Ba24Si100

space P 41 3 2
rmax=20 a 14.0685
core=Ba0
edge=N4

output Ba24Si100_feff.inp

atoms
    Ba    0.1887  0.1887  0.1887  Ba0
    Ba    0.8750  0.8750  0.8750  Ba1
    Ba    0.1250  0.8072  0.0572  Ba2
    Si    0.0362  0.0362  0.0362  Si0
    Si    0.2038  0.0427  0.0000  Si1
    Si    0.1250  0.1696  0.4196  Si2
    Si    0.2387  0.9394  0.8752  Si3
    Si    0.4156  0.8605  0.0769  Si4
    Si    0.3256  0.3256  0.3256  Si5
```

Table C.4: ATOMS 2.50 input file for the $Ba_{24}Si_{100}$ structure.

```
title BaSO4 (Barite)

space P b n m
rmax=15 a=7.1540  b=8.8790 c=5.4540
core=Ba0
edge=N4

output BaSO4_feff.inp

atoms
    Ba    0.1584   0.1845   0.2500   Ba0
    S     0.1908   0.4375   0.7500   S0
    O     0.1072   0.5870   0.7500   O0
    O     0.0498   0.3176   0.7500   O1
    O     0.3118   0.4194   0.9704   O2
```

Table C.5: ATOMS 2.50 input file for the $BaSO_4$ structure.

```
title XANES Si136

space F d -3 m
shift 0.125 0.125 0.125
rmax=20 a 14.62
core=Si0
edge=L2

output Si136_feff.inp

atoms
    Si    0.000    0.000    0.000    Si0
    Si    0.094    0.094    0.094    Si1
    Si    0.058    0.058    0.246    Si2
```

Table C.6: ATOMS 2.50 input file for the Si_{136} structure.

```
title XANES Si

space F d -3 m
shift -0.125 -0.125 -0.125
rmax=20 a 5.431
core=Si0
edge=L2

output Si_feff.inp

atoms
    Si    0.00     0.00     0.00      Si0
    Si    0.25     0.25     0.25      Si1
```

Table C.7: ATOMS 2.50 input file for the Si structure.

Bibliography

Adams, G.B., M. O'Keeffe, A.A. Demkov, O.F. Sankey, and Y.-M. Huang (1994), *Phys. Rev. B* **49**, 8048.

Alouani, M., J.M. Koch, and M.A. Khan (1986), *Solid State Comm.* **60**, 657.

Amusia, M.A., and J.P. Connerade (2000), *Rep. Prog. Phys.* **63**, 41.

Amusia, M.Y., A.S. Baltenkov, L.V. Chernysheva, Z. Felfi, and A.Z. Msezane (2006), *J. Exp. Theor. Phys.* **102**, 53.

Ankudinov, A.L., and J.J. Rehr (1997), *J. Phys. IV France* **7**, C2.

Ankudinov, A.L., S.I. Zabinsky, and J.J. Rehr (1996), *Comp. Phys. Comm.* **98**, 359.

Ankudinov, A.L., S.D. Conradson, J. Mustre de Leon, and J.J. Rehr (1998*b*), *Phys. Rev. B* **57**, 7518.

Ankudinov, A.L., B. Ravel, J.J. Rehr, and S.D. Conradson (1998*a*), *Phys. Rev. B* **58**, 7565.

Ankudinov, A.L., C.E. Bouldin, J.J. Rehr, J. Sims, and H. Hung (2002), *Phys. Rev. B* **65**, 104107.

Ankudinov, A.L., A.I. Nesvizhskii, and J.J. Rehr (2003), *Phys. Rev. B* **67**, 115120.

Arms, D.A., T.J. Graber, A.T. Macrander, R.O. Simmons, M. Schwoerer-Bohning, and Y. Zhong (2005), *Phys. Rev. B* **71**, 233107.

Ashcroft, N.W., and N.D. Mermin (1976), *Solid State Physics*, Thomson Learning, London.

Aulbur, W.G., L. Jönsson, and J.W. Wilkins (2000), "Solid State Physics", ed. by H. Ehrenreich and F. Spaepen, vol. 54, Academic, New York, 1.

Balakumar, S., S. Peng, K.M. Hoe, A. Agarwal, G.Q. Lo, R. Kumar, N. Balasubramanian, D.L. Kwong, and S. Tripathy (2007), *Appl. Phys. Lett.* **90**, 032111.

Balasubramanian, M., C.S. Johnson, J.O. Cross, G.T. Seidler, T.T. Fister, E.A. Stern, C. Hammer, and S.O. Mariager (2007), *Appl. Phys. Lett.* **91**, 031904.

Baldwin, G.C., and G.S. Klaiber (1947), *Phys. Rev.* **71**, 3.

— (1948), *Phys. Rev.* **73**, 1156.

Barnett, J.D., S. Block, and G.J. Piermarini (1973), *Rev. Sci. Inst.* **44**, 1.

Batson, P.E. (1993), *Phys. Rev. B* **47**, 6898.

Becker, U. (1987), "The 4d + 4f giant resonance from barium through the rare–earths", *Giant Resonances in Atoms, Molecules, and Solids*, Plenum, New York.

Belot, V., R.J.P. Corriu, D. Leclercq, P. Lefèvre, P.H. Mutin, A. Vioux, and A.M. Flank (1991), *J. Non–Cryst. Solids* **127**, 207.

Bergmann, U., and S.P. Cramer (1998), *SPIE Proc.* **3448**, 198.

Bergmann, U., P. Glatzel, and S.P. Cramer (2002), *Microchem. J.* **71**, 221.

Bergmann, U., D. Nordlund, Ph. Wernet, M. Odelius, L.G.M. Pettersson, and A. Nilsson (2007*a*), *Phys. Rev. B* **76**, 024202.

Bergmann, U., A. Di Cicco, Ph. Wernet, E. Principi, P. Glatzel, and A. Nilsson (2007*b*), *J. Chem. Phys.* **127**, 174504.

Biggs, F., L.B. Mendelsohn, and J.B. Mann (1975), *Atomic Data Nuclear Tables* **16**, 201.

Bréchignac, C., and J.P. Connerade (1994), *J. Phys. B: At. Mol. Opt. Phys.* **27**, 3795.

Bruhwiler, P.A., and S.E. Schnatterly (1990), *Phys. Rev. B* **41**, 8013.

Buczko, R., G. Duscher, S.J. Pennycook, and S.T. Pantelides (2000), *Phys. Rev. Lett.* **85**, 2168.

Busani, T., R.A.B. Devine, M. Martini, G. Spinolo, and A. Vedda (2001), *J. Non–Cryst. Solids* **280**, 177.

Cai, Y.Q., P. Chow, C.C. Chen, H. Ishii, K.L. Tsang, C.C. Kao, K.S. Liang, and C.T. Chen (2004), *AIP Conf. Proc.* **705**, 340.

Cai, Y.Q., H.K. Mao, P.C. Chow, J.S. Tse, Y. Ma, S. Patchkovskii, J.F. Shu, V. Struzhkin, R.J. Hemley, H. Ishii, C.C. Chen, I. Jarrige, C.T. Chen, S.R. Shieh, E.P. Huang, and C.C. Kao (2005), *Phys. Rev. Lett.* **94**, 025502.

Caliebe, W.A. (1997), "Inelastic X–Ray Scattering with High Energy Resolution", PhD thesis, Christian–Albrechts Universität zu Kiel.

Callcott, T.A., E.T. Arakawa, and D.L. Ederer (1978), *Phys. Rev. B* **18**, 6622.

Citrin, P.H., G.K. Wertheim, and M. Schlüter (1979), *Phys. Rev. B* **20**, 3067.

Condron, C.L., R. Porter, T. Guo, and S.M. Kauzlarich (2005), *Inorg. Chem.* **44**, 9185.

Connerade, J.P. (1987), "Controlled collapse and the profiles of 'giant resonances'", *Giant Resonances in Atoms, Molecules, and Solids*, Plenum, New York.

Connerade, J.P., and M.W.D. Mansfield (1982), *Phys. Rev. Lett.* **48**, 131.

(1987), *Giant Resonances in Atoms, Molecules, and Solids*, ed. by J.P. Connerade, J.M. Esteva, and R.C. Karnatak, Plenum, New York.

Connétable, D. (2007), *Phys. Rev. B* **75**, 125202.

(2004), *X–ray Compton Scattering*, ed. by M.J. Cooper, P.E. Mijnarends, N. Shiotani, N. Sakai, and A. Bansil, Oxford University Press.

Dahn, J.R., B.M. Way, E.F. Fuller, W.J. Weydanz, J.S. Tse, D.D. Klug, T. Van Buuren, and T. Tiedje (1994), *J. Appl. Phys.* **75**, 1946.

Dirac, P.A.M. (1930), *Proc. Camb. Phil. Soc.* **26**, 376.

Domondon, A.T., and X.M. Tong (2002), *Phys. Rev. A* **65**, 032718.

Dong, J., O.F. Sankey, and G. Kern (1999), *Phys. Rev. B* **60**, 950.

Doniach, S., and E.H. Sondheimer (1998), *Green's functions for solid state physicists*, Imperial College Press, London.

Eisenberger, P., and P.M. Platzman (1970), *Phys. Rev. A* **2**, 415.

Evers, J. (1980), *J. Solid State Chem.* **32**, 77.

Feng, Y., G.T. Seidler, J.O. Cross, A.T. Macrander, and J.J. Rehr (2004), *Phys. Rev. B* **69**, 125402.

Fister, T.T., G.T. Seidler, C. Hamner, J.O. Cross, J.A. Soininen, and J.J. Rehr (2006*a*), *Phys. Rev. B* **74**, 214117.

Fister, T.T., G.T. Seidler, L. Wharton, A.R. Battle, T.B. Ellis, J.O. Cross, A.T. Macrander, W.T. Elam, T.A. Tyson, and Q. Quian (2006*b*), *Rev. Sci. Instr.* **77**, 063901.

Friede, B., and M. Jansen (1996), *J. Non–Cryst. Solids* **204**, 202.

Fukuoka, H., K. Ueno, and S. Yamanaka, *J. Organomet. Chem.* **611**, 543.

Godby, R.W., M. Schlüter, and L.J. Sham (1988), *Phys. Rev. B* **37**, 10159.

Gonis, A., and W.H. Butler (2000), *Multiple Scattering in Solids*, Springer, New York.

Gupta, R.P., and A.J. Freeman (1976), *Phys. Lett.* **59A**, 223.

Haensel, R., G. Keitel, P. Schreiber, and C. Kunz (1969), *Phys. Rev.* **188**, 1375.

Hämäläinen, K., and S. Manninen (2001), *J. Phys.: Condens. Matter* **13**, 7539.

Hämäläinen, K., S. Galambosi, J.A. Soininen, E.L. Shirley, J.P. Rueff, and A. Shukla (2002), *Phys. Rev. B* **65**, 155111.

Hamann, D.R. (2000), *Phys. Rev. B* **61**, 9899.

Hänsch, W., and W. Ekardt (1982), *Phys. Rev. B* **25**, 7815.

Hatada, K., K. Hayakawa, M. Benfatto, and C.R. Natoli (2007), *Phys. Rev. B* **76**, 060102(R).

Hedin, L. (1965), *Phys. Rev.* **139**, A796.

Hermann, K., L.G.M. Pettersson, M.E. Casida, C. Daul, A. Goursot, A. Koester, E. Proynov, A. St-Amant, D.R. Salahub, V. Carvetta, H. Duarte, C. Friedrich, N. Godbout, J. Guan, C. Jamorski, M. Leboeuf, M. Leetmaa, M. Nyberg, L. Pedocchi, F. Sim, L. Triguero, and A. Vela (2005), *StoBe Software*, 2005.

Hill, J.P., D.S. Coburn, Y.J. Kim, T. Gog, D.M. Casa, C.N. Kodituwakku, and H. Sinn (2007), *J. Synch. Rad.* **14**, 361.

Hohl, A., T. Wieder, P.A. van Aken, T.E. Weirich, G. Denninger, M. Vidal, S. Oswald, C. Deneke, J. Mayer, and H. Fuess (2003), *J. Non–Cryst. Solids* **320**, 255.

Holm, P. (1988), *Phys. Rev. A* **37**, 3706.

Holm, P., and R. Ribberfors (1989), *Phys. Rev. A* **40**, 6251.

Hubbard, J. (1957), *Proc.R. Soc. London Ser. A* **240**, 539.

Huotari, S., K. Hämäläinen, S. Manninen, A.A. Issolah, and M. Marangolo (2001), *J. Phys. Chem. Solids* **62**, 2205.

Huotari, S., G. Vankó, F. Albergamo, C. Ponchut, H. Graafsma, C. Henriquet, R. Verbeni, and G. Monaco (2005), *J. Synch. Rad.* **12**, 467.

Iitaka, T. (2007), *Phys. Rev. B* **75**, 012106.

Jacobsen, S.D., J.R. Smyth, R.J. Swope, and R.T. Downs (1998), *Can. Mineral.* **36**, 1053.

Jayaraman, A. (1983), *Rev. Mod. Phys.* **55**, 65.

Joly, Y. (2001), *Phys. Rev. B* **63**, 125120.

Kahn, D., and J.P. Lu (1997), *Phys. Rev. B* **56**, 13898.

Kapaklis, V., C. Politis, P. Poulopoulos, and P. Schweiss (2005), *Appl. Phys. Lett.* **87**, 123114.

Kas, J.J., A.P. Sorini, M.P. Prange, L.W. Cambell, J.A. Soininen, and J.J. Rehr (2007), *Phys. Rev. B* **76**, 195116.

Kawaji, H., H. Horie, S. Yamanaka, and M. Ishikawa (1995), *Phys. Rev. Lett.* **74**, 1427.

Kirkpatrick, P., and A.V. Baez (1948), *J. Opt. Soc. Am.* **38**, 766.

Kohn, W., and L.J. Sham (1965), *Phys. Rev.* **140**, A1133.

Kramers, H.A., and W. Heisenberg (1925), *Z. Phys.* **31**, 681.

Krisch, M., and F. Sette (2002), *Surf. Rev. Lett.* **9**, 969.

Krisch, M.H., F. Sette, C. Masciovecchio, and R. Verbeni (1997), *Phys. Rev. Lett.* **78**, 2843.

Krywka, C., M. Paulus, C. Sternemann, M. Volmer, A. Remhof, G. Nowak, A. Nefedov, B. Pöter, M. Spiegel, and M. Tolan (2006), *J. Synch. Rad.* **13**, 8.

Kumar, R.S., A.L. Cornelius, M.G. Pravica, M.F. Nicol, M.Y. Hu, and P.C. Chow (2007), *Diamond Rel. Mat.* **16**, 1136.

Kume, T., H. Fukuoka, T. Koda, S. Sasaki, H. Shimizu, and S. Yamanaka (2003), *Phys. Rev. Lett.* **90**, 155503.

Laugier, J., and B. Bochu (2001), *POUDRIX V2*, Laboratoire des matériaux et du génie physique, 2001, URL: `http://www.lmgp.inpg.fr`.

Lee, S.K., P.J. Eng, H.K. Mao, Y. Meng, M. Newville, M.Y. Hu, and J.F. Shu (2005), *Nature Materials* **4**, 851.

Lee, S.K., P.J. Eng, H.K. Mao, Y. Meng, and J. Shu (2007), *Phys. Rev. Lett.* **98**, 105502.

Llopart, X., M. Campbell, R. Dinapoli, D.S. Sequndo, and E. Pemigotti (2002), *IEEE Trans. Nucl. Sci.* **49**, 2279.

Lu, T.Z., M. Alexe, R. Scholz, V. Talalaev, R.J. Zhang, and M. Zacharias (2006), *J. Appl. Phys.* **100**, 014310.

Luberek, J., and G. Wendin (1996), *Chem. Phys. Lett.* **248**, 147.

Ma, H., S.H. Lin, R.W. Carpenter, and O.F. Sankey (1990), *J. Appl. Phys.* **68**, 288.

Mahan, G.D. (1967), *Phys. Rev.* **163**, 612.

Mamiya, M., H. Takei, M. Kikuchi, and C. Uyeda (2001), *J. Cryst. Growth* **229**, 457.

Mao, W.L., H.K. Mao, P.J. Eng, T.P. Trainor, M. Newville, C.C. Kao, D.L. Heinz, J.F. Shu, Y. Meng, and R.J. Hemley (2003), *Science* **302**, 425.

Mao, W.L., H.K. Mao, Y. Meng, P.J. Eng, M.Y. Hu, P. Chow, Y.Q. Cai, J.F. Shu, and R.J. Hemley (2006), *Science* **314**, 636.

Mattila, A. (2007), "Studies of electronic structure by x–ray Raman and emission spectroscopy: applications to MgB_2 superconductors and high pressure physics", PhD thesis, University of Helsinki.

Mattila, A., J.A. Soininen, S. Galambosi, T. Pylkkänen, S. Huotari, N.D. Zhigadlo, J. Karpinski, and K. Hämäläinen, "Electron hole counts in Al substituted MgB_2 from x-ray Raman scattering", submitted to Phys. Rev. B.

Mattila, A., J.A. Soininen, S. Galambosi, S. Huotari, G. Vankó, N.D. Zhigadlo, K. Karpinski, and K. Hämäläinen (2005), *Phys. Rev. Lett.* **94**, 247003.

Meng, Y., H.K. Mao, P.J. Eng, T.P. Trainor, M. Newville, M.Y. Hu, C.C. Kao, J.F. Shu, D. Hausermann, and R.J. Hemley (2004), *Nat. Mater.* **3**, 111.

Miguel, A. San, and P. Toulemonde (2005), *High Pressure Res.* **25**, 159.

Miguel, A. San, A. Merlen, P. Toulemonde, T. Kume, S. Le Floch, A. Aouizerat, S. Pascarelli, G. Aquilanti, O. Mathon, T. Le Bihan, J.P. Itie, and S. Yamanaka (2005), *Europhys. Lett.* **69**, 556.

Mitsuke, K., T. Mori, and J. Kou (2005), *J. Chem. Phys.* **122**, 064304.

Mizuno, Y., and Y. Ohmura (1967), *J. Phys. Soc. Jpn.* **22**, 445.

Mudryk, Y., P. Rogl, C. Paul, S. Berger, E. Bauer, G. Hilscher, C. Godart, and H. Noël (2002), *J. Phys.: Condens. Matter* **14**, 7991.

Nagasawa, H., S. Mourikis, and W. Schülke (1989), *J. Phys. Soc. Jpn.* **58**, 710.

— (1997), *J. Phys. Soc. Jpn.* **66**, 3139.

Nolas, G.S., G.A. Slack, and S.B. Schujman (2001), *Semicond. Semimet.* **69**, 255.

Nozières, P., and C.D. De Dominicis (1969), *Phys. Rev.* **178**, 1097.

Onellion, M., Y. Chang, D.W. Niles, R. Joynt, G. Margaritondo, N.G. Stoffel, and J.M. Tarascon (1987), *Phys. Rev. B* **36**, 819.

Papaconstantopoulos, D. (1986), *Handbook of the Band Structures of Elemental Solids*, Plenum, New York.

Perdew, J.P., and M. Levy (1983), *Phys. Rev. Lett.* **51**, 1884.

Philipp, H.R. (1971), *J. Phys. Chem. Solids* **32**, 1935.

— (1972), *J. Non–Cryst. Solids* **8–10**, 627.

Ravel, Bruce (1998), *ATOMS 2.50*, University of Washington / ANL, 1998, URL: `cars9.uchicago.edu/~ravel`.

Rehr, J.J., J.A. Soininen, and E.L. Shirley (2005), *Physica Scripta* **T115**, 207.

Rehr, J.J., J.J. Kas, M.P. Prange, F.D. Vila, A.L. Ankudinov, L.W. Campbell, and A.P. Sorini (2006), arXiv:cond-mat/0601241, 2006.

Ribberfors, R. (1975), *Phys. Rev. B* **12**, 2067.

Richter, M., M. Meyer, M. Pahler, T. Prescher, E.V. Raven, B. Sonntag, and H.E. Wetzel (1989), *Phys. Rev. A* **39**, 5666.

Russ, J.C. (1984), *Fundamentals of energy dispersive x–ray analysis*, Butterworths, London.

Saito, K., and T. Sagawa (1981), *J. Phys. Soc. Jpn.* **50**, 1660.

Sakko, A., M. Hakala, J.A. Soininen, and K. Hämäläinen (2007), *Phys. Rev. B* **76**, 205115.

Schacht, A. (2007), "Untersuchung der Disproportionierung von massivem amorphen Germaniummonoxid", diploma thesis, Universität Dortmund.

Schülke, W. (1991), "Inelastic scattering by electronic excitations", *Handbook on synchrotron radiation, Vol. 3*, ed. by G.S. Brown and D.E. Moncton, North–Holland, Amsterdam.

— (2007), *Electron dynamics by inelastic x–ray scattering*, Oxford University Press.

Sham, L.J., and M. Schlüter (1983), *Phys. Rev. Lett.* **51**, 1888.

Slater, J.C., and G.F. Koster (1954), *Phys. Rev.* **94**, 1498.

Soininen, J.A. (2001), "Final–state interactions in inelastic x–ray scattering", PhD thesis, University of Helsinki.

Soininen, J.A., and E.L. Shirley (2001), *Phys. Rev. B* **64**, 165112.

Soininen, J.A., K. Hämäläinen, W.A. Caliebe, C.-C. Kao, and E.L. Shirley (2001), *J. Phys.: Condens. Matter* **13**, 8039.

Soininen, J.A., A.L. Ankudinov, and J.J. Rehr (2005), *Phys. Rev. B* **72**, 045136.

Soininen, J.A., A. Mattila, J.J. Rehr, S. Galambosi, and K. Hämäläinen (2006), *J. Phys.: Cond. Mat.* **18**, 7327.

Sternemann, C., K. Hämäläinen, A. Kaprolat, A. Soininen, G. Döring, C.C. Kao, S. Manninen, and W. Schülke (2000), *Phys. Rev. B* **62**, R7687.

Sternemann, C., M. Volmer, J.A. Soininen, H. Nagasawa, M. Paulus, H. Enkisch, G. Schmidt, M. Tolan, and W. Schülke (2003), *Phys. Rev. B* **68**, 035111.

Sternemann, C., J.A. Soininen, M. Volmer, A. Hohl, G. Vankó, S. Streit, and M. Tolan (2005*c*), *J. Phys. Chem. Solids* **66**, 2277.

Sternemann, C., J.A. Soininen, S. Huotari, G. Vankó, M. Volmer, R.A. Secco, J.S. Tse, and M. Tolan (2005*a*), *Phys. Rev. B* **72**, 035104.

Sternemann, C., S. Huotari, G. Vankó, M. Volmer, G. Monaco, A. Gusarov, H. Lustfeld, K. Sturm, and W. Schülke (2005*b*), *Phys. Rev. Lett.* **95**, 157401.

Sternemann, C., H. Sternemann, S. Huotari, F. Lehmkühler, M. Tolan, and J.S. Tse (2008*a*), *J. Anal. Atom. Spectrom.* DOI: `10.1039/B717441A`.

Sternemann, H., J.A. Soininen, C. Sternemann, K. Hämäläinen, and M. Tolan (2007*a*), *Phys. Rev. B* **75**, 075118.

Sternemann, H., C. Sternemann, J.S. Tse, S. Desgreniers, Y.Q. Cai, G. Vankó, N. Hiraoka, A. Schacht, J.A. Soininen, and M. Tolan (2007*b*), *Phys. Rev. B* **75**, 245102.

Sternemann, H., C. Sternemann, G.T. Seidler, T.T. Fister, A. Sakko, and M. Tolan (2008*b*), *J. Synch. Rad.* **15**, 162.

Streit, S., C. Gutt, V. Chamard, A. Robert, M. Sprung, H. Sternemann, and M. Tolan (2007), *Phys. Rev. Lett.* **98**, 244.

Suzuki, S., T. Ishii, and T. Sagawa (1975), *J. Phys. Soc. Japan* **38**, 156.

Suzuki, T. (1967), *J. Phys. Soc. Jpn.* **22**, 1139.

Taillefumier, M., D. Cabaret, A.-M. Flank, and F. Mauri (2002), *Phys. Rev. B* **66**, 195107.

Temkin, R.J. (1975), *J. Non–Cryst. Solids* **17**, 215.

von Barth, U., and G. Grossmann (1979), *Solid State Comm.* **32**, 645.

— (1982), *Phys. Rev. B* **25**, 5150.

von Barth, U., and L. Hedin (1972), *J. Phys. C: Solid State Phys.* **5**, 1629.

Wang, H., and J. Zhou (2005), *J. Appl. Cryst.* **38**, 830.

Wendin, G. (1973), *Phys. Lett. A* **A–46**, 119.

Wendin, G., and B. Wästberg (1993), *Phys. Rev. B* **48**, 14764.

Weng, X., P. Rez, and O.F. Sankey (1989), *Phys. Rev. B* **40**, 5694.

Weng, X., P. Rez, and P.E. Batson (1990), *Solid State Comm.* **74**, 1013.

Wernet, Ph., D. Nordlund, U. Bergmann, M. Cavalleri, M. Odelius, H. Ogasawara, L.A. Naslund, T.K. Hirsch, L. Ojamae, P. Glatzel, L.G.M. Pettersson, and A. Nilsson (2004), *Science* **304**, 995.

Wernet, Ph., D. Testemale, J.-L. Hazemann, R. Argoud, P. Glatzel, L.G.M. Pettersson, A. Nilsson, and U. Bergmann (2005), *J. Chem. Phys.* **123**, 154503.

Williams, A.R., and J. van W. Morgan (1972), *J. Phys. C: Solid State Phys.* **5**, L293.

Yamanaka, S., and S. Maekawa (2006), *Z. Naturforsch.* **61b**, 1493.

Yamanaka, S., E. Enishi, H. Fukuoka, and M. Yasukawa, *Inorg. Chem.* **39**, 56.

Yang, L., Y.M. Ma, T. Iitaka, J.S. Tse, K. Stahl, Y. Ohishi, Y. Wang, R.W. Zhang, J.F. Liu, H.-K. Mao, and J.Z. Jiang (2006), *Phys. Rev. B* **74**, 245209.

Zacharias, M., R. Weigand, B. Dietrich, F. Stolze, J. Bläsing, P. Veit, T. Drüsedau, and J. Christen (1997), *J. Appl. Phys.* **81**, 2384.

Zacharias, M., J. Heitmann, R. Scholz, U. Kahler, M. Schmidt, and J. Bläsing (2002), *Appl. Phys. Lett.* **80**, 661.

Zangwill, A. (1987), "A condensed matter view of giant resonance phenomena", *Giant Resonances in Atoms, Molecules, and Solids*, Plenum, New York.

Zangwill, A., and P. Soven (1980), *Phys. Rev. A* **21**, 1561.

Zimina, A., S. Eisebitt, W. Eberhardt, J. Heitmann, and M. Zacharias (2006), *Appl. Phys. Lett.* **88**, 163103.

Index

Publications

H. Sternemann *et al.* (2008*b*), *J. Synch. Rad.* **15**, 162: “An extraction algorithm for core–level excitations in non–resonant inelastic x–ray scattering spectra”

H. Sternemann *et al.* (2007*b*), *Phys. Rev. B* **75**, 245102: “Giant dipole resonance of Ba in Ba_8Si_{46}: An approach for studying high–pressure induced phase transitions of nanostructured materials”

H. Sternemann *et al.* (2007*a*), *Phys. Rev. B* **75**, 075118: “Near–edge structure of nonresonant inelastic x–ray scattering from L–shell core levels studied by a real–space multiple–scattering approach”

C. Sternemann *et al.* (2008*a*), *J. Anal. Atom. Spectrom.* DOI: `10.1039/B717441A`: “The barium giant dipole resonance in barite: a study of soft x–ray absorption edges with hard x–rays”

S. Streit *et al.* (2007), *Phys. Rev. Lett.* **98**, 244: “Two dimensional dynamics of metal nanoparticles on the surface of thin polymer films studied with coherent x–rays”

Acknowledgements

I would like to thank all the people without whom this work would not have been possible:

First, I would like to thank my supervisors M. Tolan and C. Sternemann for the possibility to write this thesis and for all invaluable support and encouragement I experienced during the past four years. I am also grateful to J.A. Soininen and A. Sakko for many helpful discussions and for the BSE and StoBe–deMon calculations respectively.

I thank A. Schacht for the GeO data and beneficial cooperation in the data analysis. I also thank J.S. Tse for many fruitful discussions and support during the barium experiments, especially for caring about the DAC. Furthermore, I am grateful to S. Desgreniers and S. Yamanaka for delivery of the barium/silicon samples. I acknowledge A. Hohl for discussion and the preparation of the amorphous SiO and GeO samples. For support during the experiments, I would like to thank S. Huotari, G. Vankó, and G. Monaco (ESRF), Y.Q. Cai and N. Hiraoka (SPring–8) and G.T. Seidler, T.T. Fister, R.A. Gordon (APS). For further help during beamtimes I am grateful to M. Volmer and F. Lehmkühler. I thank the ESRF, the APS, the SPring–8 and the DELTA machine group for provision of synchrotron radiation. For discussion and support, I would like to thank K. Hämäläinen. I acknowledge the mechanical workshop of the Faculty of Physics for construction of sample holders and experimental equipment. T. Witt I thank for computational support.

I am very obliged to C. Sternemann, J.A. Soininen, and M. Paulus for critical reading of my thesis and giving plenty of hints, and also to F. Flottmann and E. Sternemann for proof–reading.

For financial support I thank Deutsche Forschungsgemeinschaft and Deutscher Akademischer Austausch Dienst.

I would also like to thank the people who supported me during the past years in all non–physical concerns: I am grateful to the group Experimentelle Physik Ia of Technische Universität Dortmund for a very familiar and enjoyable working atmosphere. I thank Simo and Liisa for very entertaining evening programs in Helsinki and Grenoble. I further give thanks to all my friends for keeping my out–of–university life alive.

Finally, I would like to thank my family for the love and support in any situation, and of course Kerstin for taking all of my sorrows away.

Dortmund, February 2008, Henning Sternemann

Eidesstattliche Erklärung

Hiermit erkläre ich an Eides Statt, dass die vorliegende Dissertationsschrift — abgesehen von der Beratung durch meine wissenschaftlichen Betreuer — nach Inhalt und Form meine eigene Arbeit ist. Sie wurde weder ganz noch in Teilen an anderer Stelle im Rahmen eines Prüfungsverfahrens vorgelegt.

Dortmund, Februar 2008

(Henning Sternemann)